AERODYNAMIC MODELLING AND OPTIMIZATION OF MORPHING WINGS

A THESIS SUBMITTED TO
THE GRADUATE SCHOOL OF NATURAL AND APPLIED SCIENCES
OF
MIDDLE EAST TECHNICAL UNIVERSITY

BY

DURMUŞ SİNAN KÖRPE

IN PARTIAL FULFILLMENT OF THE REQUIREMENTS
FOR
THE DEGREE OF DOCTOR OF PHILOSOPHY
IN
AEROSPACE ENGINEERING

SEPTEMBER 2014

Approval of the thesis:

AERODYNAMIC MODELLING AND OPTIMIZATION OF MORPHING WINGS

submitted by **DURMUŞ SİNAN KÖRPE** in partial fulfillment of the requirements for the degree of **Doctor of Philosophy in Aerospace Engineering Department, Middle East Technical University** by,

Prof. Dr. Canan Özgen ______________________
Dean, Graduate School of **Natural and Applied Sciences**

Prof. Dr. Ozan Tekinalp ______________________
Head of Department, **Aerospace Engineering**

Prof. Dr. Serkan Özgen ______________________
Supervisor, **Aerospace Engineering Dept., METU**

Examining Committee Members:

Prof. Dr. Yavuz Yaman ______________________
Aerospace Engineering Dept., METU

Prof. Dr. Serkan Özgen ______________________
Aerospace Engineering Dept., METU

Prof. Dr. İsmail Hakkı Tuncer ______________________
Aerospace Engineering Dept., METU

Prof. Dr. Zafer Dursunkaya ______________________
Mechanical Engineering Dept., METU

Prof. Dr. Ünver Kaynak ______________________
Mechanical Engineering Dept., TOBB ETU

Date: 04.09.2014

I hereby declare that all the information in this document has been obtained and presented in accordance with academic rules and ethical conduct. I also declare that, as required by these rules and conduct, I have fully cited and referenced all material and results that are not original to this work.

Name, Last Name : Durmuş Sinan Körpe

Signature :

ABSTRACT

AERODYNAMIC MODELLING AND OPTIMIZATION OF MORPHING WINGS

Körpe, Durmuş Sinan

Ph.D., Department of Aerospace Engineering

Supervisor: Prof. Dr. Serkan Özgen

September 2014, 117 pages

This thesis deals with aerodynamic optimization of morphing wings under performance and geometric constraints. In order to perform the optimization process, flow solvers computing aerodynamic lift and drag were developed as a function evaluator. A gradient based optimization method was used in order to develop the optimization algorithm.

Three dimensional panel method solver was developed in order to obtain lift, pressure drag and induced drag values for a finite wing. Obtained results were compared with different solvers. Compared results were in agreement for low to moderate angles of attack. Two dimensional boundary layer solver was developed in order to obtain the skin friction drag for each strip along span. The boundary layer results were compared with another solver for different angle of attack values and agreement in the results was observed at low to moderate angle of attack values.

Optimization solver was developed by using the generalized reduced gradient method. A benchmark structural optimization problem was solved by using this solver and results were compared with the results in the literature.

Morphing wing optimization process started with a fixed wing optimization problem for a certain cruise velocity at steady level flight for the baseline wing. Fixed wing optimization was performed for three cases that are only airfoil shape change, only planform change and combined airfoil shape and planform change.

After that it was assumed that materials and mechanisms for morphing that were used for another study in the literature were available and the morphing optimization problem was defined according to them. Similar to fixed wing optimization, the process was performed for only airfoil shape change, only planform change and combined airfoil shape and planform change. The optimization problem was solved for velocities less and greater than the cruise velocity and drag polar curve of the morphing wing was obtained. According to the results, remarkable drag reductions were obtained that is expected from a morphing wing. Nevertheless, drag reductions obtained with only planform morphing are significantly higher than those obtained with only airfoil shape morphing.

Keywords: Panel Method, Boundary Layer Flow, Generalized Reduced Gradient Method, Morphing Wings, Aerodynamic Optimization.

ÖZ

ŞEKİL DEĞİŞTİREBİLEN KANATLARIN AERODİNAMİK AÇIDAN MODELLENMESİ VE ENİYİLEMESİ

Körpe, Durmuş Sinan

Doktora, Havacılık ve Uzay Mühendisliği Bölümü

Tez Yöneticisi: Prof. Dr. Serkan Özgen

Eylül 2014, 117 sayfa

Bu tez, performans ve geometrik kısıtlamalar altında şekil değiştirebilen kanatların aerodinamik eniyilemesi ile ilgilidir. Eniyileme işlemini gerçekleştirmek için, aerodinamik kaldırma ve sürükleme değerlerini hesaplayan akış çözücüleri geliştirilmiştir. Eniyileme çözüsünü geliştirmek için, gradyan temelli bir eniyileme metodu kullanılmıştır.

Üç boyutlu panel yöntemi çözücüsü sonlu bir kanat için kaldırma, basınç sürüklemesi ve indüklenmiş sürükleme değerlerini elde etmek amacıyla geliştirilmiştir. Sonuçlar diğer çözücülerin sonuçları ile karşılaştırılmıştır. Elde edilen sonuçlar düşük ve orta mertebedeki hücum açısı değerleri için uyumludur. İki boyutlu sınır tabaka çözücüsü kanat açıklığı boyunca her bir dilim için sürtünme sürüklemesi değerlerini elde etmek amacıyla geliştirilmiştir. Sınır tabaka çözücüsünden elde edilen sonuçlar başka bir çözücüden elde edilen sonuçlar ile karşılaştırılmış, düşük ve orta mertebedeki hücum açılarında sonuçların uyumlu olduğu gözlenmiştir. Eniyileme için genel indirgenmiş gradyan yöntemi algoritması geliştirilmiştir. Literatürde bulunan örnek bir yapısal eniyileme problemi çözülmüş ve sonuçlar literatürdeki diğer sonuçlarla karşılaştırılmıştır.

Şekil değiştirebilen kanat eniyilemesi düz ve sabit hızlı bir uçuş için bir sabit kanadın seyir hızında eniyilemesi ile başlamıştır. Sabit kanat eniyilemesi, sadece profil şekli değişimi, sadece kanat şekli değişimi ile profil şekli ve kanat şekli değişimi birlikte olmak üzere üç şekilde yapılmıştır.

Daha sonra, literatürde bulunan bir çalışmadaki şekil değiştirmeyi sağlayan malzeme ve mekanizmaların mevcut olduğu varsayılarak, şekil değiştirebilen kanat eniyileme problemi tanımlanmıştır. Sabit kanat eniyilemesine benzer şekilde şekil değiştirebilen kanat eniyilemesi de sadece profil şekli değişimi, sadece kanat şekli değişimi ile profil şekli ve kanat şekli değişimi birlikte olmak üzere üç şekilde yapılmıştır. Eniyileme problemi seyir hızının altındaki ve üstendeki hızlar için çözülmüş ve bu sayede şekil değiştirebilen kanadın sürükleme kuvvet değerleri elde edilmiştir. Sonuçlara göre, şekil değiştirebilen kanadın beklentilere uygun olarak, kayda değer ölçüde düşük sürükleme kuvveti ürettiği gözlenmiştir. Bununla beraber, kanat şekli değişimi ile elde edilen sürükleme kuvveti azalması, sadece profil şekli değişimi ile elde edilenden belirgin bir şekilde fazladır.

Anahtar Kelimeler: Panel Metodu, Sınır Tabaka Akışı, Genel İndirgenmiş Gradyan Yöntemi, Şekil Değiştirebilen Kanat, Aerodinamik Eniyileme.

to

My Family

and

Didem and Teoman

for their love, care and support

ACKNOWLEDGEMENTS

This study was supported by TÜBİTAK with the project number 111M731. This support is gratefully acknowledged.

I want to express my deepest gratitude to Prof. Dr. Serkan Özgen for his support, encouragement and belief in me.

I want to thank my thesis committee members Prof. Dr. İsmail Hakkı Tuncer and Prof. Dr. Zafer Dursunkaya for their recommendations and advice that contributed significantly to the thesis

Thanks to my family for their support and understanding for the days that I spent for the thesis.

Thanks to my Didem who gave me encouragement to finish this study everyday with love.

TABLE OF CONTENTS

ABSTRACT v

ÖZ vii

ACKNOWLEDGEMENTS x

TABLE OF CONTENTS xi

LIST OF TABLES xv

LIST OF FIGURES xvii

LIST OF SYMBOLS xxiii

LIST OF ABBREVIATIONS xxvii

CHAPTERS

1 INTRODUCTION 1

  1.1 Background of the Study 1

  1.2 Review of Literature 7

  1.3 Objectives 14

2 THREE DIMENSIONAL PANEL METHOD 19

  2.1 Introduction 19

  2.2 Theory 19

  2.3 Comparison of pan3d.f Results with XFLR5 23

  2.4 Wake Alignment 27

2.4.1 Results 28

2.5 Application of Iterative Kutta Condition 29

2.5.1 Results 31

2.6 Conclusion 34

3 TWO DIMENSIONAL BOUNDARY LAYER SOLVER 35

3.1 Introduction 35

3.2 Theory 39

3.2.1 Laminar Boundary Layer 39

3.2.2 Transition from Laminar to Turbulent Flow 40

3.2.3 Head’s Method for Turbulent Region 41

3.2.4 Separation Correction Functions for Lift and Drag 42

3.3 Comparison of the Results with XFOIL 43

3.4 Conclusion 47

4 GENERALIZED REDUCED GRADIENT METHOD 49

4.1 Introduction 49

4.2 Theory 49

4.2.1 Generalized Reduced Gradient Method 49

4.2.2 Step Length Selection 52

4.2.2.1 Golden Search Method 53

4.2.3 Selection of Basic and Nonbasic Variables 54

4.2.4 Algorithm for Going Back to Feasible Region 55

4.3 Comparison of the Results for A Structural Optimization Problem 56

4.4 Conclusion.. 64

5 MORPHING WING OPTIMIZATION 65

5.1 Introduction 65

5.2 Use of the Optimization Solver 65

5.3 Baseline Wing 68

5.4 Fixed Wing Optimization 71

5.4.1 Fixed Wing Optimization with Only Airfoil Shape Change 72

5.4.2 Fixed Wing Optimization with Only Planform Change 75

5.4.3 Fixed Wing Optimization with Airfoil Shape and Planform Change 78

5.5 Morphing Wing Optimization 82

5.5.1 Morphing Wing Optimization with Only Airfoil Shape Change 82

5.5.2 Morphing Wing Optimization with Only Planform Change 94

5.5.3 Morphing Wing Optimization with Airfoil Shape and Planform Change 97

5.6 Conclusion.. 103

6 CONCLUSION 105

REFERENCES 109

VITA 115

LIST OF TABLES

TABLES

Table 2.1 C_L, C_{DP} and C_{DI} results for pan3d.f and XFLR5 for different α (NACA 4412, $c_r = 0.4$ m., $b/2 = 3$ m., $\lambda = 0$, $\Lambda = 0$, $\Gamma = 0$, $\theta = 0$, $\varphi = 0$). 25

Table 2.2 C_L, C_{DP} and C_{DI} results for pan3d.f and XFLR5 for different α (NACA 4412, $c_r = 0.4$ m., $b/2 = 3$ m., $\lambda = 0.5$, $\Lambda = 5°$, $\Gamma = 5°$, $\theta = 0$, $\varphi = 5°$). 26

Table 2.3 C_L, C_{DP} and C_{DI} values that are obtained with FLUENT (F) and panel method, RW (Rolled-up wake), SW (Straight wake) at different angle of attack values. 29

Table 2.4 Straight wake results at different element number of A. 33

Table 2.5 Rolled-up wake results at different element number of A. 33

Table 3.1 Comparison of XFOIL and 2DBLS. 46

Table 4.1 Iteration history of the methods (cm^3 volume at iterations). 60

Table 4.2 Optimum design variable values. 61

Table 5.1 Steady level flight data for baseline wing. 70

Table 5.2 Steady level flight data for optimum wing that is obtained with only airfoil shape change. 74

Table 5.3 Steady level flight data for optimum wing that is obtained with only planform change. 78

Table 5.4 Steady level flight data for optimum wing that is obtained with airfoil shape and planform change. 82

Table 5.5 Steady level flight data for morphing wing that is obtained with only airfoil shape change at 16 m/s. 86

Table 5.6 Steady level flight data for morphing wing that is obtained with only airfoil shape change at 20 m/s. 88

Table 5.7 Steady level flight data for morphing wing that is obtained with only airfoil shape change at 40 m/s. 90

Table 5.8 Steady level flight data for morphing wing that is obtained with only airfoil shape change at 50 m/s. 93

Table 5.9 Steady level flight data for morphing wing that is obtained with only planform change. 96

Table 5.10 Steady level flight data for morphing wing that is obtained with airfoil shape and planform change. 100

LIST OF FIGURES

FIGURES

Figure 1.1 Clement Ader’s Eole – a shape changer in 1890 [1]. 2

Figure 1.2 Wright brothers’ kite with control sticks (top), Wing twisting (bottom) [2]. 2

Figure 1.3 Pterodactyl IV (left) [1], MAK-10 (right) [5]... 3

Figure 1.4 BAKSAEV LIG-7 [1]... 4

Figure 1.5 F-111 at different sweep phases (left) [8], Tornado F3 (right) [7]. 4

Figure 1.6 Lockheed-Martin’s morphing wing on UAV [10].................................... 5

Figure 1.7 Hypercomp/NextGen’s morphing wing on UAV [10]. 6

Figure 1.8 Raytheon morphing wing on missile [11]. 6

Figure 1.9 Telescopic wing in testing configurations [12]. 7

Figure 1.10 Comparison of telescoping wing with fixed wing and theoretical results [12]. 8

Figure 1.11 Chord change mechanism [13]. 8

Figure 1.12 Achievable airfoil shapes [13]. 8

Figure 1.13 Experimental model in test tunnel [14]. 9

Figure 1.14 The influence of span extension on the drag for the upswept case [14]. 10

Figure 1.15 Two-design-variable morphing wing [15]... 10

Figure 1.16 Morphing wing comparison with cambered wing and flat plate [15]. ... 11

Figure 1.17 Actuated and non-actuated illustration of variable camber airfoil [16]. . 11

Figure 1.18 XFOIL lift and lift to drag ratio results [16]. 12

Figure 1.19 Wing twisting mechanism [17]. 12

Figure 1.20 Wing with twist and warping mechanism [18]. 13

Figure 1.21 Lift to drag ratio results at different twist angle and angle of attack values [18]. 13

Figure 1.22 Chord and airfoil change mechanism retracted (top), extended (bottom) [19]. 14

Figure 1.23 Span extension mechanism retracted (top), extended (bottom) [19]. 15

Figure 1.24 Optimum morphing airfoil shape [19]. 16

Figure 1.25 Optimum morphing wing planforms [19]. 16

Figure 2.1 Wake doublet strength at trailing edge [21].. 22

Figure 2.2 Body and wake panels of pan3d.f. 23

Figure 2.3 Aircraft, Jibe, used in experiments [23]. 23

Figure 2.4 Comparison of XFLR5 and experimental results [23]............................ 24

Figure 2.5 Wing A from XFLR5 (top), pan3d.f (bottom) (NACA 4412, $c_r = 0.4$ m., $b/2 = 3$ m., $\lambda = 0$, $\Lambda = 0$, $\Gamma = 0$, $\theta = 0$, $\varphi = 0$). 25

Figure 2.6 Wing B from XFLR5 (top), pan3d.f (bottom) (NACA 4412, $c_r = 0.4$ m., $b/2 = 3$ m., $\lambda = 0.5$, $\Lambda = 5°$, $\Gamma = 5°$, $\theta = 0$, $\varphi = 5°$).. 26

Figure 2.7 Rolled-up wake (left) and straight wake (right) alignment for a rectangular wing (NACA 4412 AR = 6). 27

Figure 2.8 Mesh generated in GAMBIT (786584 triangular wall faces, 3956733 tetrahedral cells in domain). 28

Figure 2.9 Comparison of pressure contours $\alpha=4^\circ$ (− Fluent − pan3d.f, Straight Wake). 28

Figure 2.10 Absolute ΔCp at the trailing edge of the wing, (− (rolled-up), − (straight), − (convergence criteria)). 31

Figure 2.11 Pressure coefficient distribution at mid section. 32

Figure 3.1 Lift coefficient correction due to separation [31]. 35

Figure 3.2 Orr-Sommerfeld spatial amplification curves [33]. 36

Figure 3.3 Calculated (bold) and experiential (symbols) drag polar for LNV109A airfoil [33]. 37

Figure 3.4 Velocity potential distribution of optimum airship body [34]. 38

Figure 3.5 Calculated and corrected C_L values for baseline wing. 42

Figure 3.6 Skin friction coefficient (left) and momentum thickness (right) comparison for $\alpha=0^\circ$. 44

Figure 3.7 Skin friction coefficient (left) and momentum thickness (right) comparison for $\alpha=4^\circ$. 45

Figure 3.8 Skin friction coefficient (left) and momentum thickness (right) comparison for $\alpha=8^\circ$. 45

Figure 3.9 Skin friction coefficient (left) and momentum thickness (right) comparison for $\alpha=12^\circ$. 46

Figure 4.1 Local or global estimation of Golden search method [43]. 53

Figure 4.2 Cantilevered beam. 56

Figure 4.3 **σ** values according to initial infeasible design variables (left) and initial feasible design variables (right). 58

Figure 4.4 y_5 values according to initial infeasible design variables (left) and initial feasible design variables (right). 59

Figure 4.5 **σ** values according to initial feasible design variables (left) optimum design variables (right) of Method 7. 62

Figure 4.6 **σ** values according to initial feasible design variables (left) optimum design variables (right) of Method 8. 62

Figure 4.7 y_5 values according to initial feasible design variables (left) optimum design variables (right) of Method 7. 63

Figure 4.8 y_5 values according to initial feasible design variables (left) optimum design variables (right) of Method 8. 63

Figure 5.1 Variation of Lagrange multiplier with objective function value. 67

Figure 5.2 Baseline wing airfoil. 69

Figure 5.3 Baseline wing, top view. 69

Figure 5.4 Drag vs. velocity for baseline wing. 70

Figure 5.5 Baseline airfoil and optimum airfoil that is obtained with only airfoil shape change. 73

Figure 5.6 Drag vs. velocity for baseline wing and optimum wing that is obtained with only airfoil shape change. 74

Figure 5.7 Baseline wing and optimum wing that is obtained with only planform change, top view. 76

Figure 5.8 Drag vs. velocity for baseline wing and optimum wings that are obtained with only airfoil shape change and only planform change. 77

Figure 5.9 Baseline wing and optimum wings that are obtained with only airfoil shape change, only planform change and airfoil shape and planform change, top view. 79

Figure 5.10 Baseline airfoil and optimum airfoils that are obtained with only airfoil shape change, only planform change and airfoil shape and planform change... 80

Figure 5.11 Drag vs. velocity for baseline wing and optimum wings that are obtained with only airfoil shape change, only planform change and airfoil shape and planform change. 81

Figure 5.12 Morphing airfoil shapes at % 5 allowance (top left), % 10 allowance (top right), % 15 allowance (bottom left), without physical constraint (bottom right) at 16 m/s. 84

Figure 5.13 Morphing airfoil shapes at different allowances at 16 m/s. 85

Figure 5.14 Morphing airfoil shapes at % 5 allowance (top left), % 10 allowance (top right), % 15 allowance (bottom left), without physical constraint (bottom right) at 20 m/s. 87

Figure 5.15 Morphing airfoil shapes at different allowances at 20 m/s. 88

Figure 5.16 Morphing airfoil shapes at % 5 allowance (top left), % 10 allowance (top right), % 15 allowance (bottom left), without physical constraint (bottom right) at 40 m/s. 89

Figure 5.17 Morphing airfoil shapes at different allowances at 40 m/s. 90

Figure 5.18 Morphing airfoil shapes at % 5 allowance (top left), % 10 allowance (top right), % 15 allowance (bottom left), without physical constraint (bottom right) at 50 m/s. 91

Figure 5.19 Morphing airfoil shapes at different allowances at 50 m/s. 92

Figure 5.20 Drag vs. velocity for baseline wing, optimum wing that is obtained with airfoil shape and planform change and morphing wing that is obtained with only airfoil shape change with 10 % change allowance. 94

Figure 5.21 Baseline wing and optimum wing that is obtained with airfoil shape and planform change and morphing wings that are obtained with only planform change at different velocities, top view. 95

Figure 5.22 Drag vs. velocity for baseline wing, optimum wing that is obtained with airfoil shape and planform change and morphing wings that are obtained with only airfoil shape change and only planform change. 97

Figure 5.23 Baseline wing, optimum wing that is obtained with airfoil shape and planform change and morphing wings that are obtained with airfoil shape and planform change, top view. 99

Figure 5.24 Morphing airfoil that is obtained with airfoil shape and planform change at 16 m/s (top left), at 20 m/s (top right), 40 m/s (bottom left), 50 m/s (bottom right). 101

Figure 5.25 Drag vs. velocity for baseline wing, optimum wing that is obtained with airfoil shape and planform change and morphing wings that are obtained with only airfoil shape change, only planform change and airfoil shape and planform change. 102

LIST OF SYMBOLS

A		Influence coefficient matrix of doublets
b	(m)	Wing span
b	(cm)	Width of bar
B		Influence coefficient matrix of source
c	(m)	Chord
c_r	(m)	Root chord
c_t	(m)	Tip chord
C		Influence coefficient matrix of the body and wake doublets
C		Jacobian matrix of constraints with respect to basic variables
C_D		Drag coefficient
C_{DF}		Skin friction drag coefficient
C_{DI}		Induced drag coefficient
C_{DP}		Pressure drag coefficient
C_L		Lift coefficient
C_p		Pressure coefficient
d		Equality constraints
D	(N)	Drag
D		Jacobian of the constraints with respect to nonbasic variables
D_F	(N)	Skin friction drag
D_I	(N)	Induced drag
D_P	(N)	Pressure drag
E	(N/cm^2)	Young's modulus
f		Objective function

F		Derivative array of the objective function with respect to design variables
g		Total equality constraints
G		Jacobian of the constraints with respect to the design variables
G_r		Generalized reduced gradient vector
h	(cm)	Height of bar
h		Inequality constraints
h		Central difference parameter
H		Boundary-layer profile shape factor
H_1		Head's method shape factor
ip		Number of panels along chord
I	(cm^4)	Moment of inertia
kp		Number of panels along span
l	(cm)	Length of each segment
l		Thwaites' parameter
l		Equality constraints
L	(N)	Lift
L	(cm)	Length of cantilever beam
M	(Ncm)	Moment
n		Logarithm of the maximum amplification ratio
n		Normal of the panel
N		Number of bars
N		Number of body panel
N_w		Number wake panels
P	(N)	Force
Q_∞	(m/s)	Three dimensional freestream velocity
r		Distance vector
Re		Reynolds number
Re_θ		Momentum thickness Reynolds number

$Re_{\theta crit}$		Critical momentum thickness Reynolds number
S		Search direction for basic variables
T		Search direction for nonbasic variables
U_{sep}	(m/s)	Separation location edge velocity
U_{te}	(m/s)	Trailing edge velocity
V	(cm^3)	Volume
V_e	(m/s)	Panel edge velocity
V_∞	(m/s)	Velocity
W	(N)	Weight
x	(m,-)	Cartesian axis direction
x_{sep}	(m)	Separation location
x_{sepup}	(m)	Upper region separation location
x_{te}	(m)	Trailing edge location
x_{trlow}	(m)	Lower region transition location
x_{trup}	(m)	Upper region transition location
x^l		Upper bound of design variables
x^u		Lower bound of design variables
X		Design variables
y_i	(cm)	Deflection of segment i
y_i'		Derivative of deflection of segment i
Y		Basic variables
Y^u		Upper bound of basic variables
Y^l		Lower bound of basic variables
z		Control points
$\left(\frac{z}{c}\right)_{upinitial}$		Physical thickness of starting airfoil
$\left(\frac{z}{c}\right)_{up}$		Physical thickness of optimum airfoil
Z		Nonbasic variables
Z^u		Upper bound of nonbasic variables

Z^l		Lower bound of nonbasic variables
α	(^{o})	Angle of attack
λ		Step length
λ		Taper ratio
λ		Thwaites’ paramater
Λ	(^{o})	Leading edge sweep angle
Γ	(^{o})	Dihedral angle
θ	(^{o})	Incidence angle
θ	(m)	Momentum thickness
φ	(^{o})	Twist angle
ρ	(kg/m^3)	Density of air
μ	(Ns/m^2)	Viscosity
μ		Value of doublet strengths
δ	(m)	Boundary layer thickness
δ^*	(m)	Boundary layer displacement thickness
Σ	(N/cm^2)	Bending stress
Σ		Value of source strength
Φ		Stream function

LIST OF ABBREVIATIONS

UAV	Unmanned Air Vehicle
DARPA	Defense Advanced Research Projects Agency
MAS	Morphing Aircraft Structure
CPU	Central Processing Unit

CHAPTER 1

INTRODUCTION

1.1 Background of the Study

In history, mankind was always inspired by nature. He admired the creatures that can act unlike him and tried to mimic especially the flying creatures, birds. Apart from mythological stories, human controlled flight in the modern sense officially began in 1903. However, before this, many attempts for controlled flight occurred and inspiration from birds in these attempts was an obvious fact.

In 1890, Clement Ader designed a flying machine that can change its shape during flight, which can be seen in Figure 1.1. In his report, Scout aircraft, which is a model that is defined by him, is defined as follows [1]:

"Whatever category airplanes might belong to, they must satisfy the following general conditions: their wings must be articulated in all their parts and must be able to fold up completely... When advances in aircraft design and construction permit, the frames will fold and the membranes will be elastic in order to diminish or increase the bearing surfaces at the wish of the pilot..."

In July 1899, Wilbur Wright used a set of cables in order to warp (twist) a biplane kite whose span was five feet, which is shown in Figure 1.2. In 1902, Wright brothers discovered how to overcome adverse yaw effect of a twisted wing by designing a moveable vertical rudder and connecting its control system to the twisting system so that the aircraft was easy to control. Use of such a system in aircraft is accepted as a more important contribution than powered flight performed by them in 1903 according to some aviation historians [2].

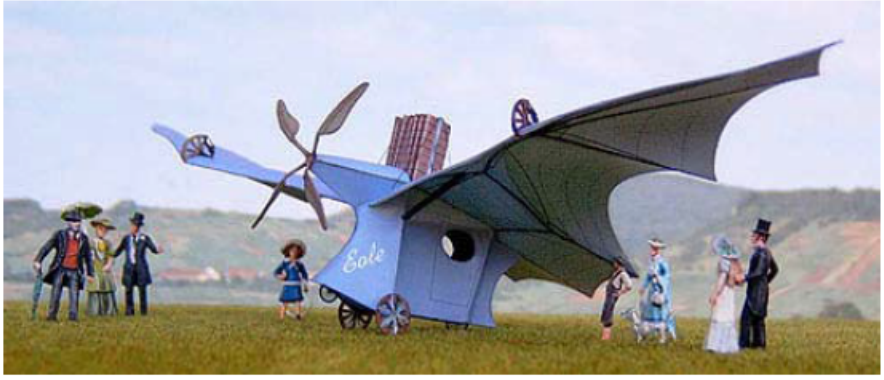

Figure 1.1 Clement Ader's Eole – a shape changer in 1890 [1].

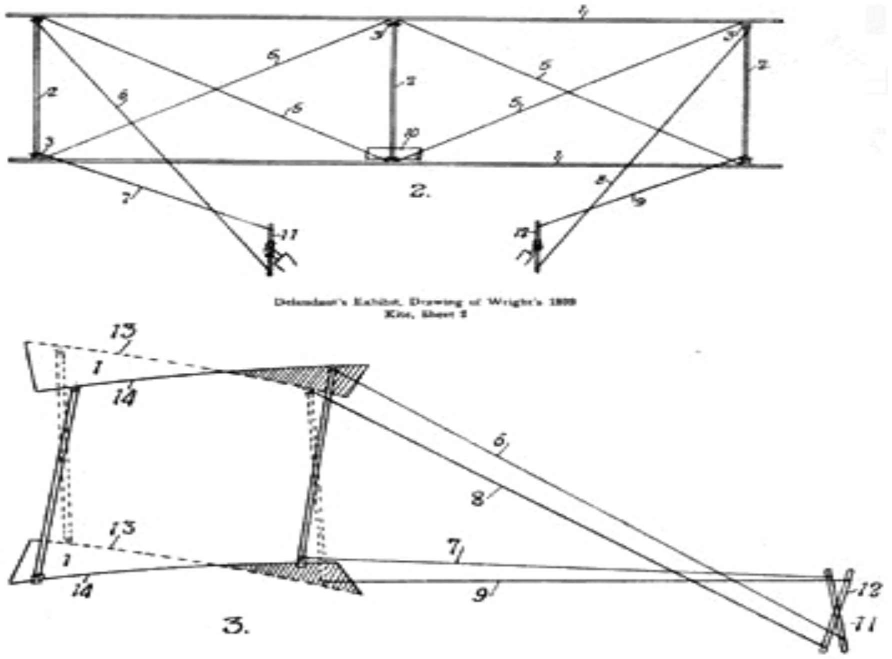

Defendant's Exhibit, Drawing of Wright's 1899 Kite, Sheet 2

Figure 1.2 Wright brothers' kite with control sticks (top), Wing twisting (bottom) [2].

Most of the early flying machines used wing warping with morphing mechanisms to maneuver. Obviously, this required complex mechanisms and manpower to operate, which rendered them highly inefficient. After the first powered flight, aviation mainly focused on military purposes, such as reconnaissance and bombing [3]. These military objectives drew the roadmap of today's aviation. As hunter-prey relationship in the air was uncovered, customers of flying machines demanded to overcome their enemies. Aircraft designers started to give up using wing shape changing systems due to lack of appropriate materials and actuators and high energy that is required by them in order to meet the customer requirements for manned flying machines. Replacement of wing warping with energy efficient ailerons is an outcome of this situation [4].

Among early attempts to change planform during flight, one may mention G.T.R Hill's Pterodactyl IV, in Figure 1.3, which had a variable sweep between 4 to 75 degrees, and Ivan Makhonine's MAK-10, in Figure 1.3, which had a telescoping wing that could increase its span by 162% [1]. These airplanes both flew in 1931.

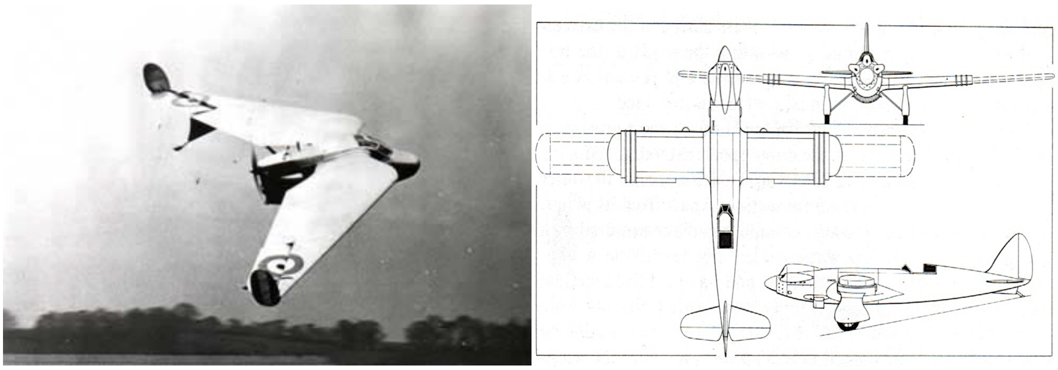

Figure 1.3 Pterodactyl IV (left) [1], MAK-10 (right) [5].

In 1937, BAKSAEV LIG-7, in Figure 1.4, which had telescoping wing sections that could extend the chord in the inner 2/3 of the half span when high lift was required and could fully retract into fuselage, was tested and no serious control problems were encountered [1].

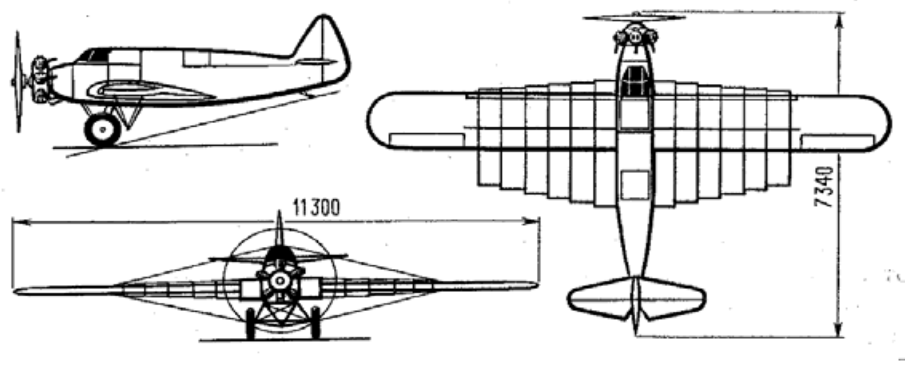

Figure 1.4 BAKSAEV LIG-7 [1].

As it is known, aviation is developing with the investments for fulfilling military and civilian demands. As a result, the most applicable wing shape change, i.e. sweep change applications were implemented not only to experimental fighter aircraft such as Grumman XF10F Jaguar, first flight in 1952 and Dassault Mirage G, first flight in 1967, [1] but also fighter aircraft that were mass produced such as the F-111, in Figure 1.5, last example retiring in 2010 [6] and Tornado F3, in Figure 1.5, which will operate until 2020 with these Royal Saudi Airforce [7].

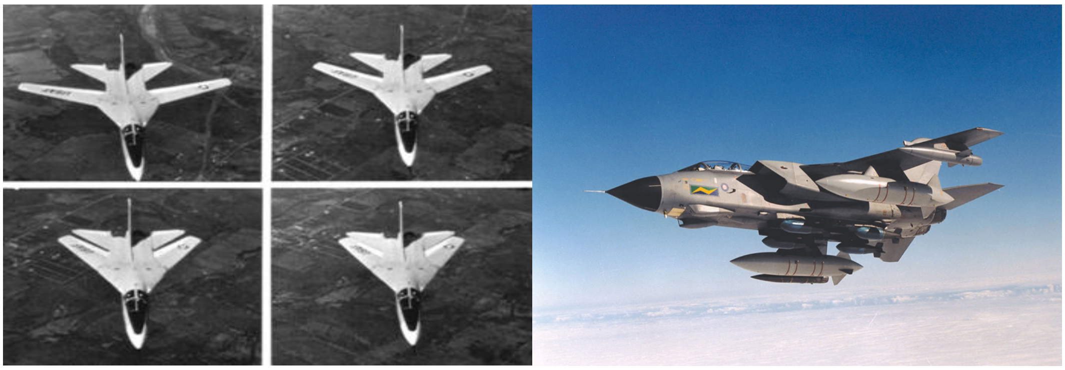

Figure 1.5 F-111 at different sweep phases (left) [8], Tornado F3 (right) [7].

In short, Aviation adventure of mankind was always inspired by the flight of birds. However, during the progress in aviation, wings of the birds cannot be fully mimicked due to lack of advanced materials and mechanisms. This situation brought the world into today's current aircraft configurations, which are designed and optimized for one or only a few flight conditions with fixed wing geometry. Contrary to this, due to success in advancing smart materials, including sensors, actuators, and their associated support hardware and micro-electronics in recent years, there has been a growing interest in shape changing, morphing, wings [9]. In general, morphing wing applications are developed by implementing them on unmanned air vehicles (UAV). The ability of wing morphing promises the following improvements: improved performance covering the entire flight envelope, simplification of conventional control surfaces and their mechanisms, improvement of the quality of the flow field surrounding the vehicle which will result in drag reduction and lift increase, reduction of manufacturing costs, reduction of the vehicle empty weight, hence improved payload capacity and fuel economy [9].

In 2003, the Defense Advanced Research Projects Agency (DARPA) announced the Morphing Aircraft Structure (MAS) program, which would end in 30 months, with three contractors that are Lockheed-Martin, Hypercomp/NextGen and Raytheon Missile Systems. The goals of the program were to develop morphing wing structures and air vehicle systems that would provide aerodynamic performance, flight control and operational effectiveness, which were not possible with conventional air vehicles [1]. Lockheed-Martin's design, which is in Figure 1.6, uses an advanced skin material in order to fold the wing for transonic dash mission of the UAV flight envelope.

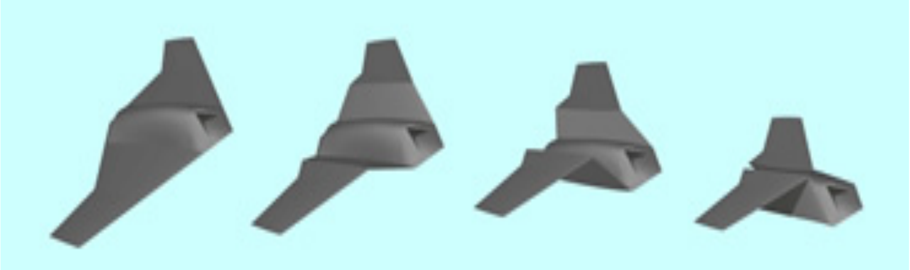

Figure 1.6 Lockheed-Martin's morphing wing on UAV [10].

Hypercomp/NextGen used stretching and sliding skins in order to obtain a morphing mechanism, which is depicted in Figure 1.7, and it was designed in order to obtain stand-alone motion of the left and right wing for flight control [1].

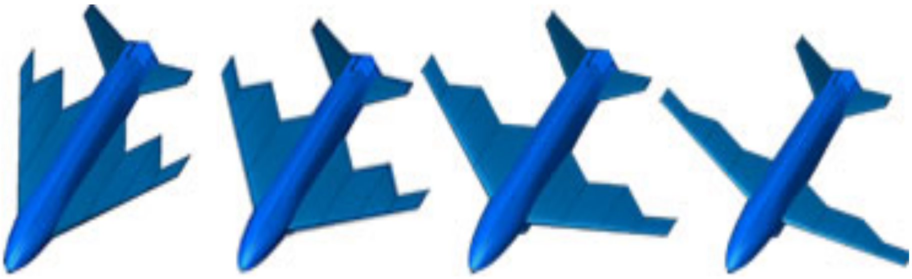

Figure 1.7 Hypercomp/NextGen's morphing wing on UAV [10].

Contrary to the design approaches of Lockheed-Martin and Hypercomp/NextGen, Raytheon focused only on missiles for Navy systems. In the design, wing area and aspect ratio of the wing were increased by using telescopic systems. However, this approach was problematic due to the required internal volume for the structural mechanism [1].

Figure 1.8 Raytheon morphing wing on missile [11].

DARPA's MAS program encouraged scientists whose main research areas are aerodynamics, structures, material, mechanisms, sensors and actuators or even polymer and nano science technology to focus and study morphing wing technology.

1.2 Review of Literature

The scientists that are interested in morphing wings mainly concentrate on shape changing mechanism design. The main aim of most of the studies in the literature is to design a mechanism that will make the wing perform the prescribed planform and airfoil change.

Blondeau et al. [12] studied the inflatable telescopic spar concept, which consists of a pneumatic telescopic spar, rigid airfoil skins and rib elements. Six different tests were performed in a wind tunnel. Three of them were performed for fixed wings, which have the same wingspan with the telescoping wings. Remaining tests were for the telescopic wing, which is seen in Figure 1.9.

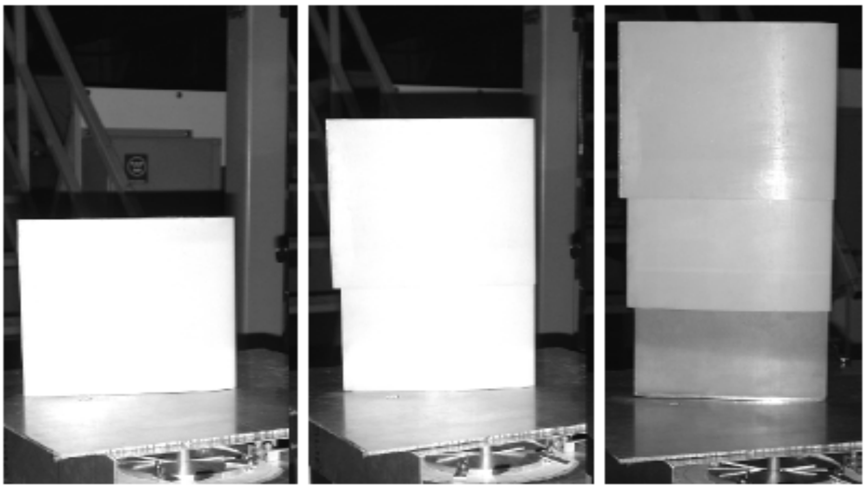

Figure 1.9 Telescopic wing in testing configurations [12].

According to the results, fully extended telescopic wing yields higher lift to drag ratio when it is compared with fully retracted telescopic wing, which is an expected result of the morphing concept. However, fully extended telescoping wing has lower lift-to-drag ratio than fixed wing with the same wingspan, because the seams between the wing sections increase the parasite drag according to the results in Figure 1.10.

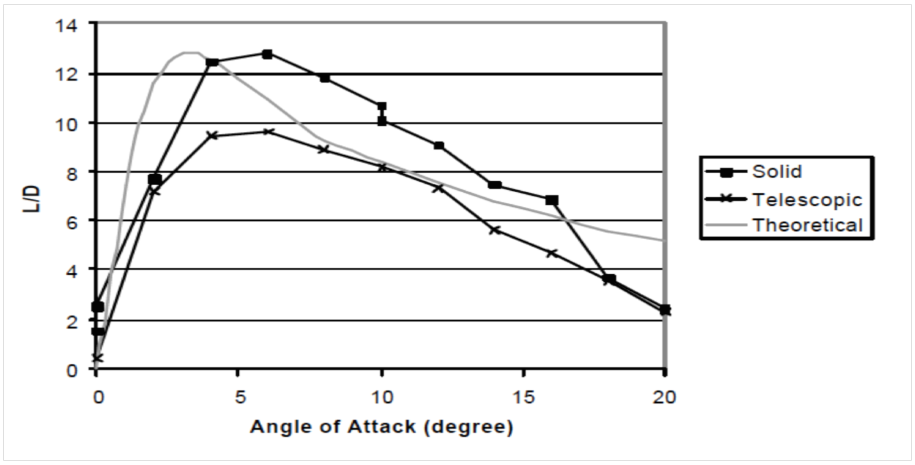

Figure 1.10 Comparison of telescoping wing with fixed wing and theoretical results [12].

Yin et al. [13] used a shape memory polymer (SMP) wing skin that has electric wire springs, which provide the required heat that makes the SMP elongate, inside the chord extension mechanism that is in Figure 1.11. Achievable airfoil shapes can be seen in Figure 1.12.

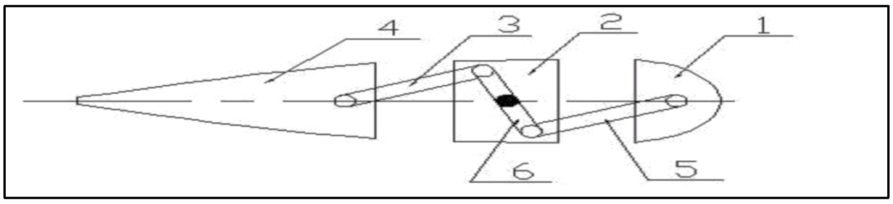

Figure 1.11 Chord change mechanism [13].

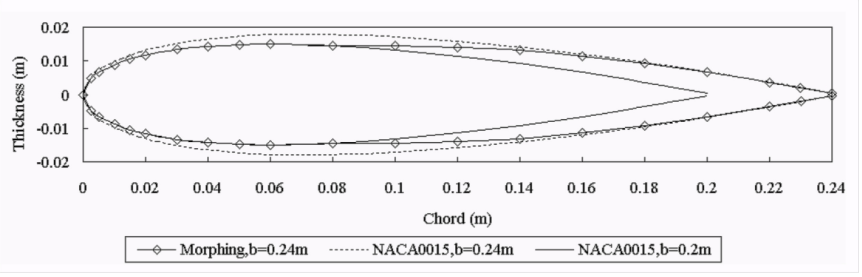

Figure 1.12 Achievable airfoil shapes [13].

In the study, it is stated that morphing wing has a thickness ratio of 16.7%, which is less than the fixed wing and Fluent results for 0.6 M shows that Mach number values along the wing decreases when the wing is morphed.

Neal et al. [14] designed and constructed a fully adaptive wing for experimental aerodynamic and flight control analysis, which is shown in Figure 1.13. Sweep change and span extension influence were analyzed at different morphing wing configurations. According to some featured results, when the wing is upswept, at small lift coefficient values (high speed), the least drag coefficient value is obtained for the shortest span. However, when the lift coefficient value is higher at a higher angle of attack, fully extended span morphing wing gives less drag coefficient results, which is seen in Figure 1.14. Actually, this is an expected result. When lift coefficient is less the speed is high and parasite drag is dominant and a wing with less surface area generates less drag. At high lift coefficient values, induced drag becomes dominant and a wing with a higher aspect ratio generates less drag. When the wing is swept, at small lift coefficient values, extended span or unextended span wing drag coefficient results are similar. However, for higher lift coefficient results, similar comments to the ones mentioned above are made.

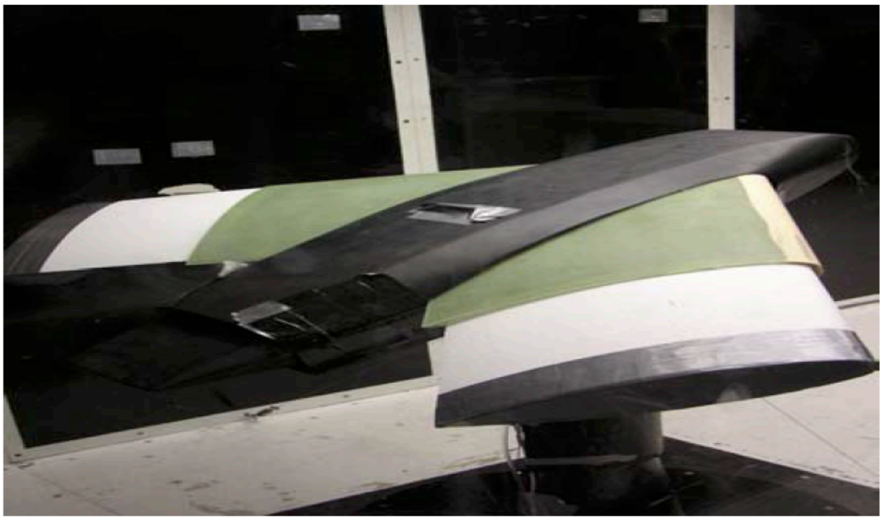

Figure 1.13 Experimental model in test tunnel [14].

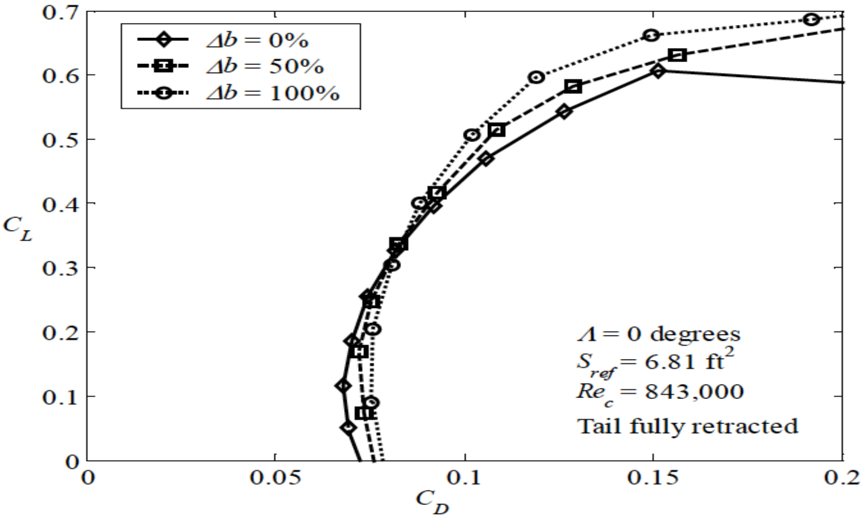

Figure 1.14 The influence of span extension on the drag for the upswept case [14].

Another important and influential morphing mechanism is changing the airfoil shape of the wing. Boria et al. [15] introduced an exceptional study in order to find the optimum camber line by using evolutionary optimization, which uses instant wind tunnel data. Primary servo, which is located at 21% of the chord, is used to provide positive camber, whereas, secondary servo is responsible for giving negative camber at the trailing edge, which are seen in Figure 1.15.

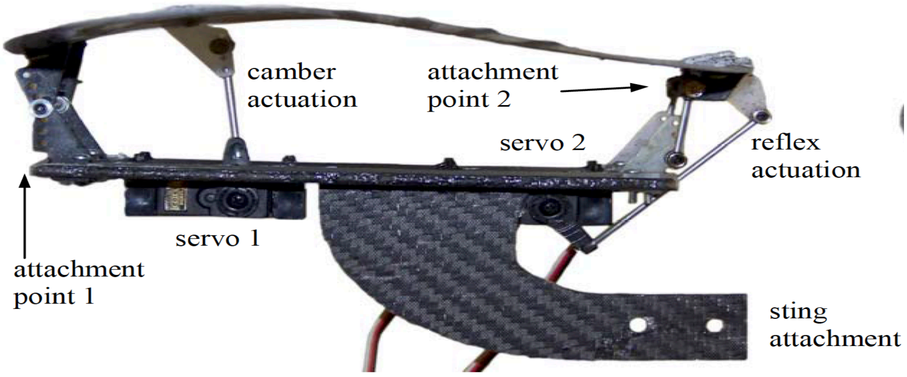
camber
actuation
attachment
point 2
servo 2
reflex
actuation
servo 1
attachment
point 1
sting
attachment

Figure 1.15 Two-design-variable morphing wing [15].

According to the results, highest lift to drag ratio is obtained at an angle of attack less than the one obtained from the cambered wing and lift to drag ratio is increased approximately by 50%, which is shown in Figure 1.16. However, repeatability and error problems in function evaluation are defined as an obstacle for optimization.

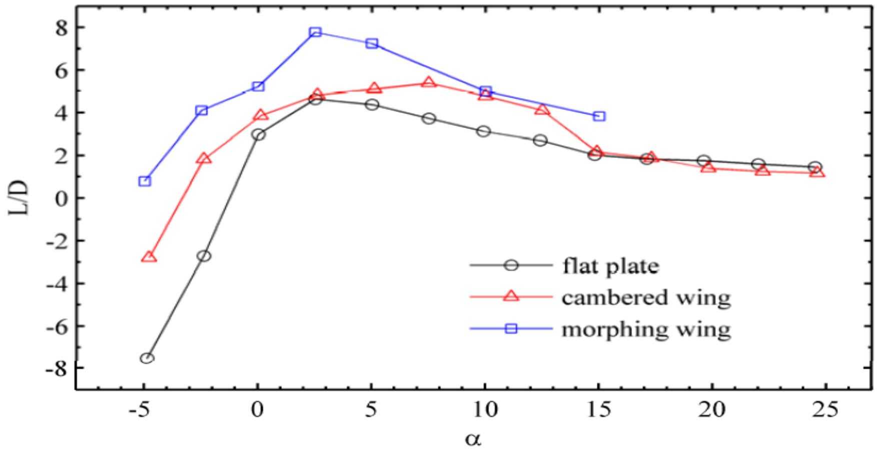

Figure 1.16 Morphing wing comparison with cambered wing and flat plate [15].

Bilgen et al. [16] proposed an airfoil concept whose continuous surface is obtained by a substrate that wraps the airfoil surface. Two actuators are used in order to obtain highest lift coefficient and lift-to-drag ratios, as it is seen in Figure 1.17. By using XFOIL, which is a two dimensional two-way panel method coupled boundary layer solver, the best lift coefficients and lift-to-drag ratios were obtained, which is demonstrated in Figure 1.18.

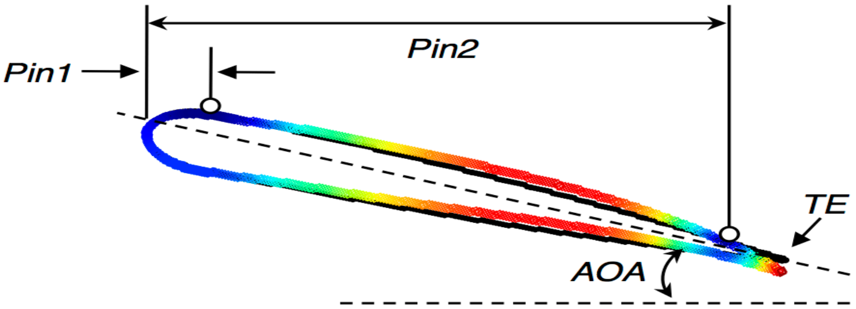

Figure 1.17 Actuated and non-actuated illustration of variable camber airfoil [16].

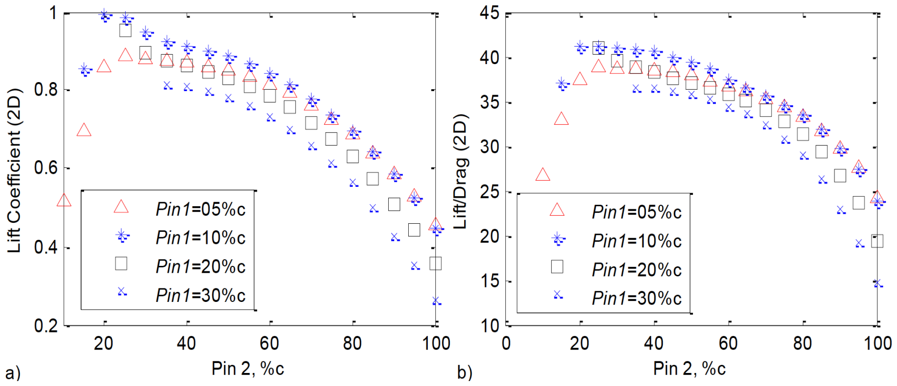

Figure 1.18 XFOIL lift and lift to drag ratio results [16].

Gonzales [17] designed a twisting mechanism for a finite wing by using Nitinol, which is a shape memory alloy (SMA), and 5.5° twist angle was obtained in the experiments, which can be seen in Figure 1-19.

Figure 1.19 Wing twisting mechanism [17].

Vos et al. [18] introduced a twist system that is obtained by four ribs, which is rotatable about the main spar independently. This mechanism yields a 27° twist angle. Threaded rod and house mechanisms are used in order to close the gap at the trailing edge, which is seen in Figure 1.20.

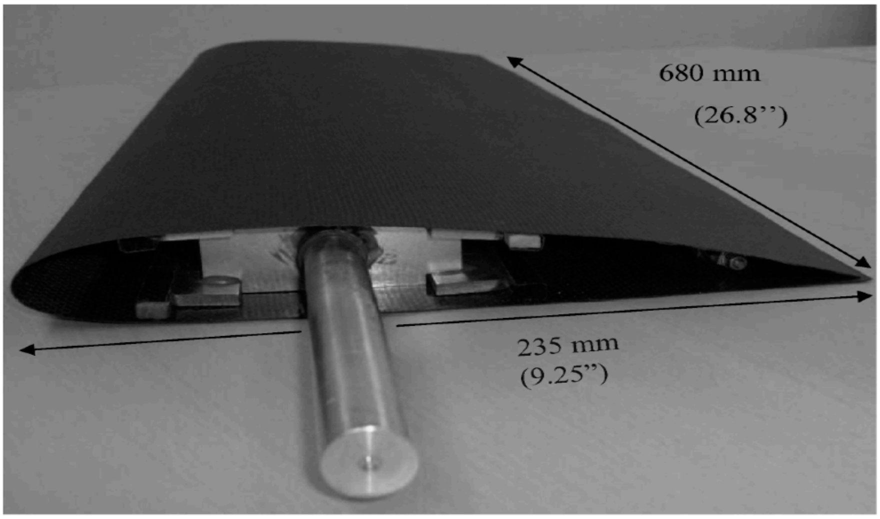

Figure 1.20 Wing with twist and warping mechanism [18].

In the experiments, a linear correlation between tip twist angle and displacement of the upper and lower surface at the trailing edge is observed. In the study, both experimental results and theoretical results are compared for lift and drag coefficient values, which is depicted in Figure 1.21.

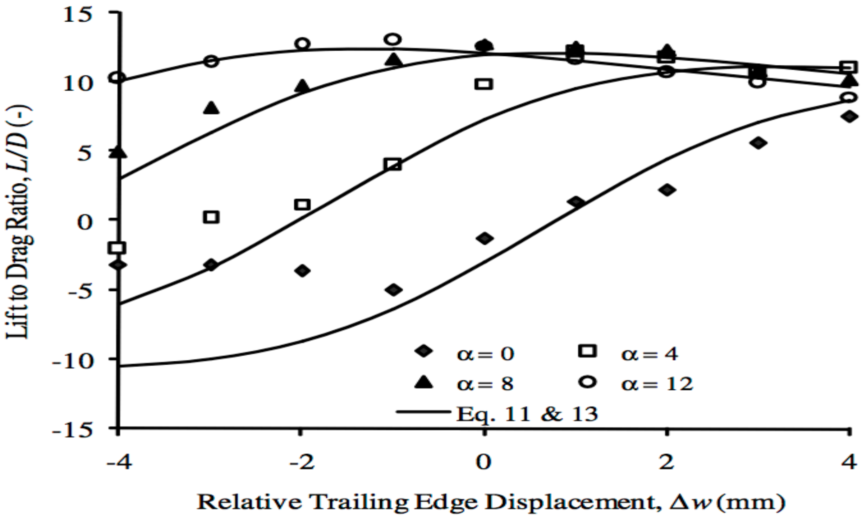

Figure 1.21 Lift to drag ratio results at different twist angle and angle of attack values [18].

According to the results in Figure 1.21, experimental and theoretical results get closer to each other as angle of attack increases.

1.3 Objectives

Before defining the aims of this thesis, it is vital to review the study of Gamboa et al. that inspires it. In their study [19], aerodynamic shape optimization code, whose objective function is to minimize drag over the intended speed range of the experimental UAV, is coupled with a structural morphing model. Their design concept is based on variable root chord, tip chord, span, and airfoil shape. The chord extension mechanism is designed not only for increasing the chord but also for airfoil thickness change by using vertical screws on the expanding mechanism, on which there are no vertical screws at the leading and the trailing edge, which is seen in Figure 1.22.

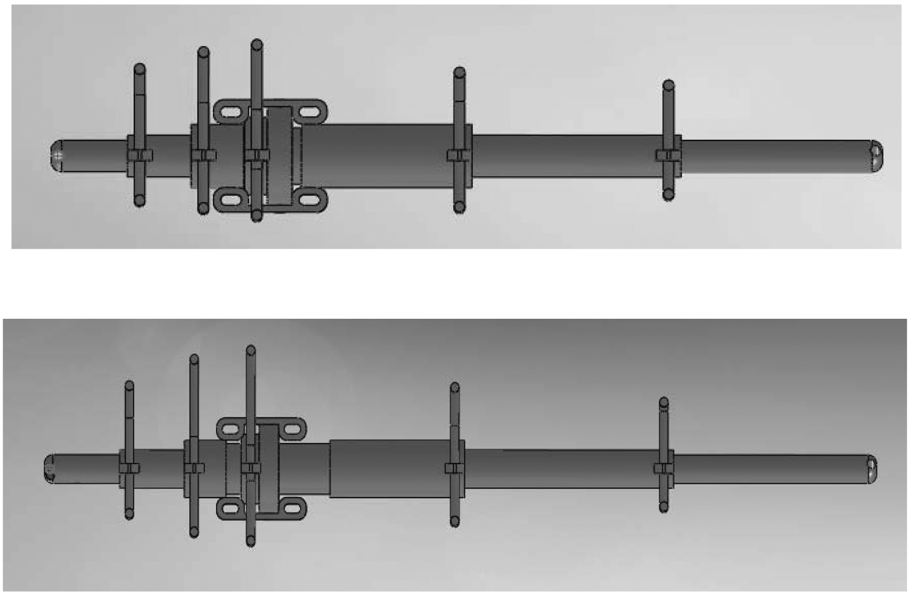

Figure 1.22 Chord and airfoil change mechanism retracted (top), extended (bottom) [19].

During the design of span extension mechanism, primary concern is even distribution of the chord and airfoil change mechanism along the span so that stiffness of the mechanism is not affected. This is performed by moving the chord and airfoil change mechanisms along span in equal distance, which is shown in Figure 1.23.

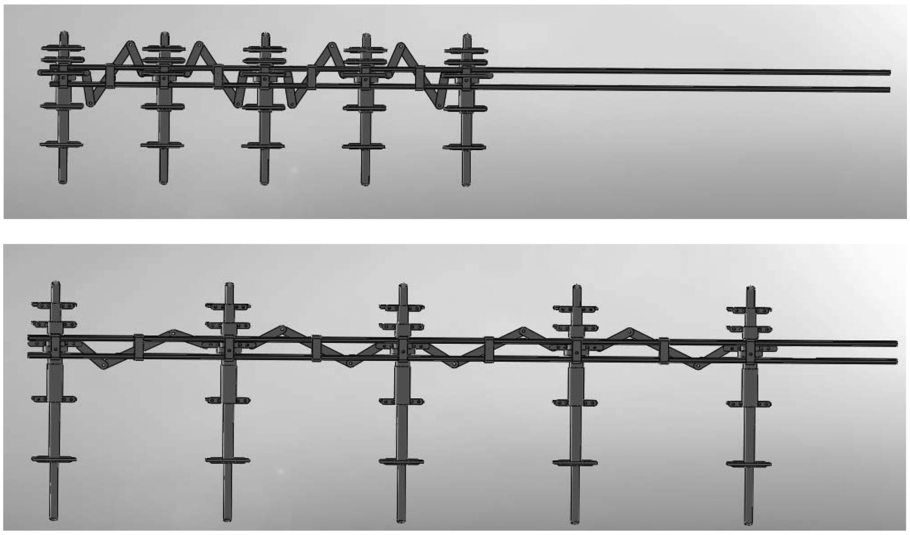

Figure 1.23 Span extension mechanism retracted (top), extended (bottom) [19].

Natural rubber is chosen as skin material due to its allowance to high strain. Aerodynamic optimization is performed for drag minimization for different velocities at level flight, where lift equals to weight, which is a constraint for the optimization problem. XFOIL is used for obtaining the parasite drag and a nonlinear lifting-line method algorithm was used in order to obtain the lift and the induced drag values. The airfoil is created with the b-spline method with 11 control points. In the optimization problem, length of the vertical screws at different chord wise locations is defined as geometric constraints as well as root chord, tip chord and span. Airfoil shapes, which are seen in Figure 1.24, and planform geometric values, which are shown in Figure 1.25, for minimum drag at different velocities are obtained by sequential quadratic programming, which is a gradient based optimization algorithm.

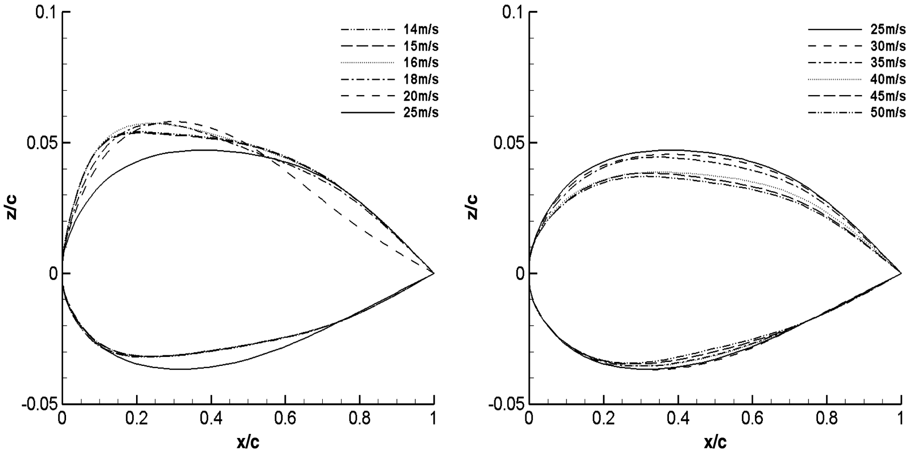

Figure 1.24 Optimum morphing airfoil shape [19].

According to the results in Figure 1.24, as the velocity increases, airfoil physical thickness decreases especially around the upper part of the airfoil, i.e., camber decreases. For velocities less than 25 m/s airfoil camber increases around the leading edge in order to obtain the required lift coefficient.

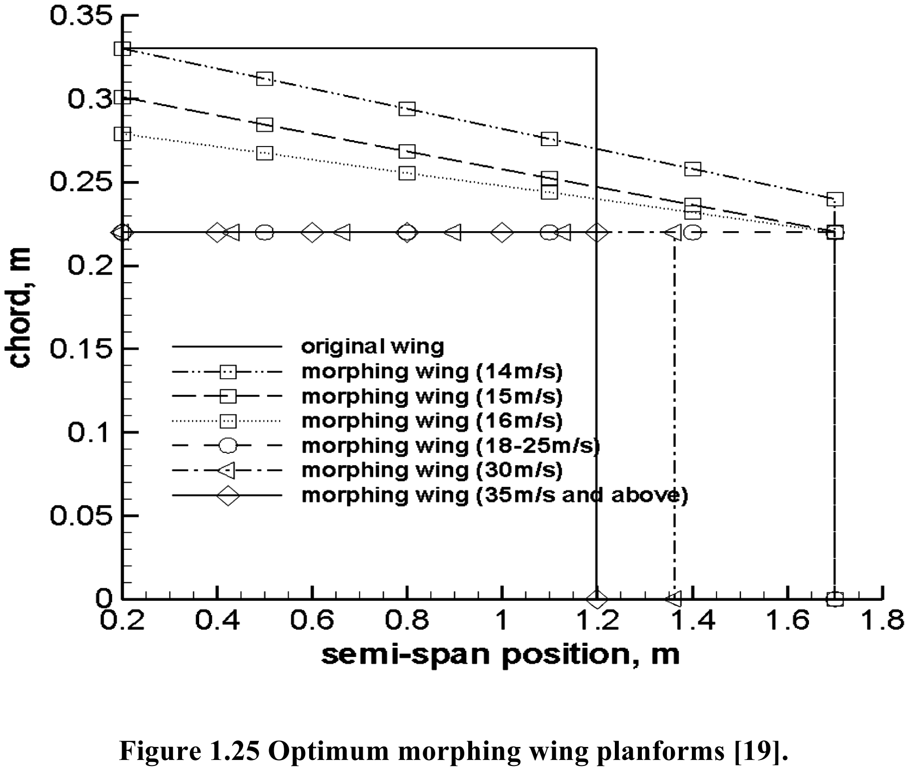

Figure 1.25 Optimum morphing wing planforms [19].

When Figure 1.25 is investigated, for lower velocities, aircraft flies at higher angles of attack and in this situation induced drag is the main source of the drag. Therefore, optimization process increases the aspect ratio and decreases the taper ratio in order to decrease the induced drag. When velocity gets higher, parasite drag, which increases as wing wetted area increases, becomes the main source for drag. Therefore, planform area decreases at high speeds.

The study in this thesis mainly comprises and gives alternative aerodynamic analysis solvers and optimization methods to the aerodynamic optimization part of the study of Gamboa et al. Morphing wing aerodynamic optimization is performed by assuming that mechanisms and materials, which are described in the study of Gamboa et al., are available for the current study as well.

The main objective of this thesis is to manifest a more realistic preliminary design tool for fixed wings and morphing wings by using finite wing data. Lift, induced drag and pressure drag are obtained by using three dimensional panel method, which is a first order method and consists of constant strength sources and doublets. Skin friction drag is found by using two dimensional laminar and turbulent boundary layer models of Thwaites and Head, respectively. Transition prediction is made by using the e^n method. As a result, the constituting components of the total drag for subsonic incompressible flow are obtained. Empirical formulations, which are defined as correction functions in the aerodynamic analysis solver, are used in order to add the influence of separation to lift and drag. For the optimization solver, generalized reduced gradient method (GRGM), which is a gradient based optimization method and whose main advantage is to maintain feasibility in spite of highly nonlinear equality or inequality constraints, is used. Three dimensional panel method, two dimensional boundary layer solver and GRGM were developed by using Fortran programing language and a deep literature survey was made for the theoretical background.

CHAPTER 2

THREE DIMENSIONAL PANEL METHOD

2.1 Introduction

Three dimensional panel method solvers are used in conceptual and preliminary design in order to obtain lift coefficient (C_L), pressure drag coefficient (C_{DP}), and induced drag coefficient (C_{DI}) values. The first use of panel methods is in late 1950s and is totally based on analytical solutions due to non-existing computers. Then, Hess and Smith gave valuable contributions to the development of panel methods, whose growth was limited by computer memory and power in the 1960s. Many low order panel methods were developed and coupling with boundary layer models was performed for more realistic solvers and results were in good agreement with experimental results at low to moderate angles of attack in the 1970s and 1980s [20]. With the help of more powerful computers, Navier-Stokes solvers became the main solver to be developed in the 1990s. But, further methods were developed for faster panel methods and wake alignment behind the lifting body and panel methods were used for rotor aerodynamic and flapping propulsion problems. In the first chapter of this thesis, examples of use of panel methods in morphing wing studies are given.

2.2 Theory

Continuity equation for steady, incompressible and irrotational flows is a second order partial differential equation, which can be seen in Equation 2.1 when velocity is defined as the gradient of velocity potential function, Φ [21].

$$\nabla^2 \Phi = 0 \tag{2.1}$$

If a flow particle cannot enter in the solid body that is immersed in a fluid, velocity component that is normal to solid body surface is zero, which is the first boundary condition and shown in Equation 2.2

$$\vec{\nabla}\Phi . \vec{n} = 0 \tag{2.2}$$

In above equation $\vec{n}$ is the normal vector of the body surface. The second boundary condition is the far field velocity boundary condition that is equal to the freestream velocity, which is shown in Equation 2.3.

$$\vec{\nabla}\Phi = V_\infty \text{ for } r \rightarrow \infty \tag{2.3}$$

By using divergence theorem, Green's identities and applying Drichlet boundary condition, which equates total velocity potential to freestream velocity potential, equation 2.4 is obtained [21].

$$\begin{aligned} &\sum_{k=1}^{N} \frac{1}{4\pi} \int_{\text{body panel}} \mu n \cdot \nabla\left(\frac{1}{r}\right) dS + \sum_{l=1}^{N_w} \frac{1}{4\pi} \int_{\text{wake panel}} \mu n \cdot \nabla\left(\frac{1}{r}\right) dS \\ &- \sum_{k=1}^{N} \frac{1}{4\pi} \int_{\text{body panel}} \sigma\left(\frac{1}{r}\right) dS = 0 \end{aligned} \tag{2.4}$$

μ value is body and wake doublet strengths and σ is the value of source strength, which are unknown. N and N_w are the number of body panel and wake panels, respectively. For constant doublet and source strength values, summation elements in above equation are defined in equations between 2.5-2.7.

$$\sum_{k=1}^{N} \frac{1}{4\pi} \int_{\text{body panel}} \mu n \cdot \nabla\left(\frac{1}{r}\right) dS = C_k \tag{2.5}$$

$$\sum_{l=1}^{N_w} \frac{1}{4\pi} \int_{\text{wake panel}} \mu n \cdot \nabla \left(\frac{1}{r}\right) dS = C_l \qquad (2.6)$$

$$-\sum_{k=1}^{N} \frac{1}{4\pi} \int_{\text{body panel}} \sigma \left(\frac{1}{r}\right) dS = B_k \qquad (2.7)$$

After these definitions, Equation 2.4 is takes the form in Equation 2.8.

$$\sum_{k=1}^{N} C_k \mu_k + \sum_{l=1}^{N_w} C_l \mu_l + \sum_{k=1}^{N} B_k \sigma_k = 0 \qquad (2.8)$$

In Equation 2.8, C_k and C_l are the influence coefficients of the body and wake panel doublets, B_k is the influence coefficient of the source of the body. These influence coefficients are calculated according to the doublet and source distributions and discretization of the geometry [21]. The source strength value is defined for each body panel as in Equation 2.9 so that Equation 2.4 is valid.

$$\sigma = \vec{n} \cdot \vec{Q}_{\infty} \qquad (2.9)$$

In above equation, $Q_{\infty}$is the freestream velocity. As a result, one of the unknown values turns out to be a known value.

Application of simple Kutta condition is based on defining the doublet strength of the wake panels by the difference between doublet strength values of upper and lower trailing edge panels at each strip along the span in Equation 2.10, which is shown in Figure 2.1. This value is constant along chordwise wake panels.

$$\mu_l = \mu_r - \mu_s \qquad (2.10)$$

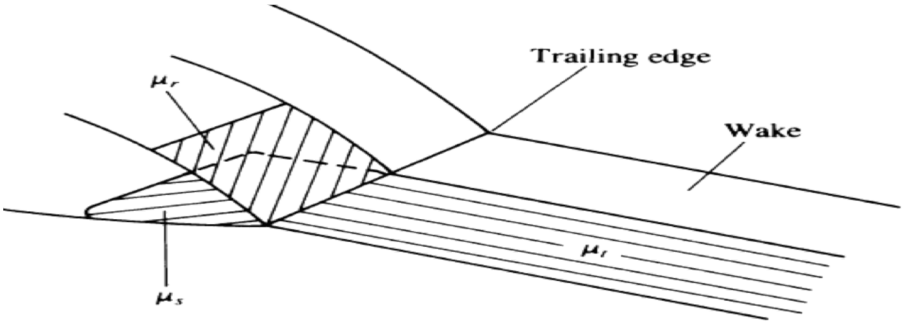

Figure 2.1 Wake doublet strength at trailing edge [21].

By using the relation in Equation 2.10 and after some conditional algebraic manipulations due to dependency of the wake panel doublets to trailing edge panel doublets, Equation 2.11 is obtained in order to find the unknowns, μ_k.

$$\sum_{k=1}^{N} A_k \mu_k = -\sum_{k=1}^{N} B_k \sigma_k \tag{2.11}$$

Once μ_k values are obtained, perturbation velocities due to the presence of the body along chordwise and spanwise panels are calculated by using a central difference formula. Total velocity is the summation of freestream and perturbation velocities and pressure coefficient values are obtained according to these velocities.

By using the theory above, a Fortran code (pan3d.f) was developed, which can model finite wings with different airfoils, root chord (c_r), span (b), taper ratio (λ), leading edge sweep angle (Λ), dihedral angle (Γ), incidence angle (θ) and twist angle (φ) values, and various tests were performed by comparing the results with XFLR5, which is a free but not open source analysis tool for airfoils, wings and planes operating at low Reynolds Numbers [22]. Body and wake panels that are generated by pan3d.f can be seen in Figure 2.2

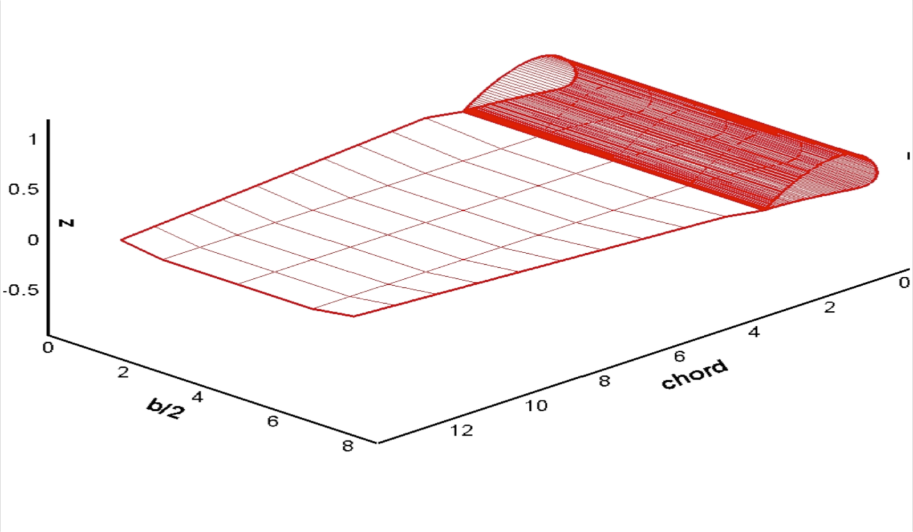
1
0.5
0
-0.5
z
0
2
4
6
8
b/2
12
10
8
6
4
2
0
chord

Figure 2.2 Body and wake panels of pan3d.f.

2.3 Comparison of pan3d.f Results with XFLR5

Prediction of XFLR5 for the model aircraft, which is shown in Figure 2.3, is in good agreement with the experimental results that can be seen in Figure 2.4 [23].

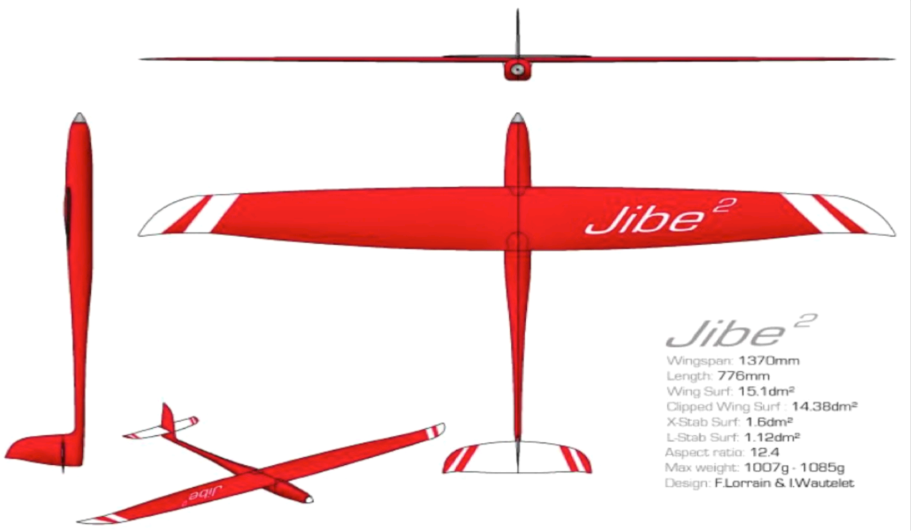
Jibe²
Jibe²
Wingspan: 1370mm
Length: 776mm
Wing Surf: 15.1dm²
Clipped Wing Surf : 14.38dm²
X-Stab Surf: 1.6dm²
L-Stab Surf: 1.12dm²
Aspect ratio: 12.4
Max weight: 1007g - 1085g
Design: F.Lorrain & I.Wautelet

Figure 2.3 Aircraft, Jibe, used in experiments [23].

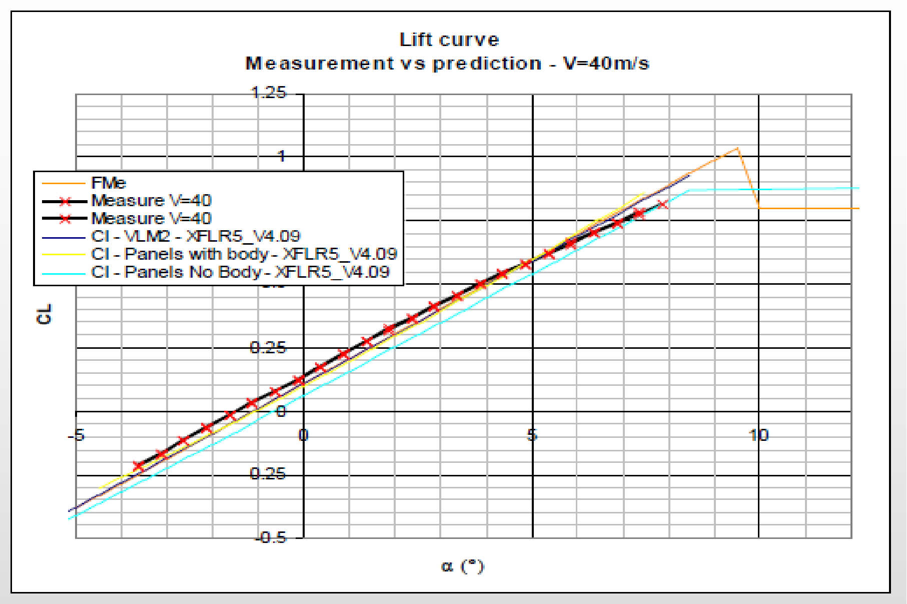

Figure 2.4 Comparison of XFLR5 and experimental results [23].

As it is seen in Figure 2.4, XFLR5 results are in good agreement with experimental results especially when the full geometry of the aircraft is modeled with panels.

In order to compare pan3d.f results with XFLR5, two different wings are used. These wings, Wing A and Wing B, can be seen in Figure 2.5 and 2.6, respectively. Comparison of aerodynamic results is given in Table 2.1 and Table 2.2, respectively.

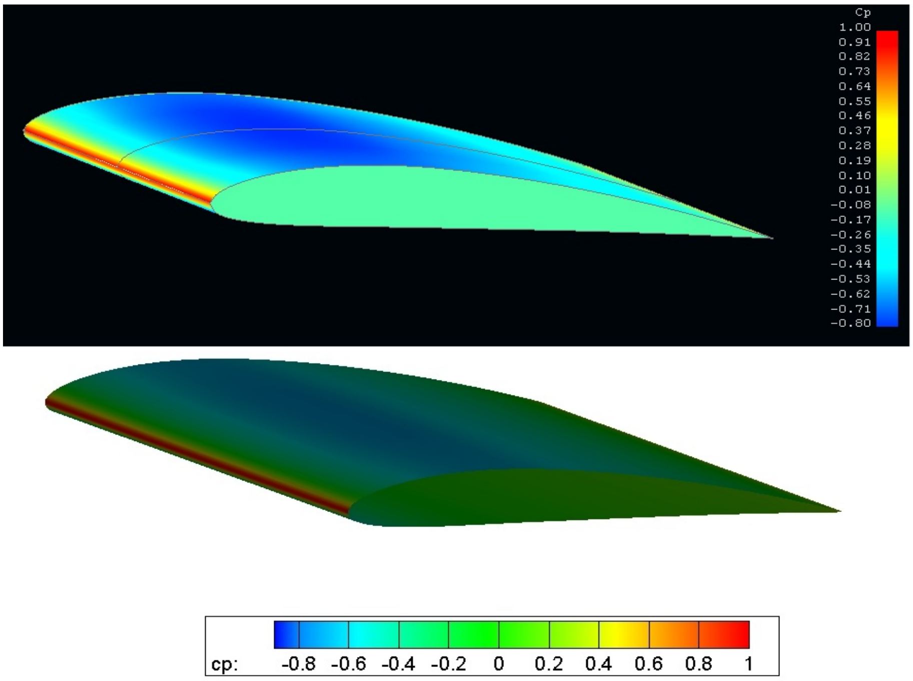
Cp
1.00
0.91
0.82
0.73
0.64
0.55
0.46
0.37
0.28
0.19
0.10
0.01
-0.08
-0.17
-0.26
-0.35
-0.44
-0.53
-0.62
-0.71
-0.80
cp:
-0.8
-0.6
-0.4
-0.2
0
0.2
0.4
0.6
0.8
1

Figure 2.5 Wing A from XFLR5 (top), pan3d.f (bottom) (NACA 4412, c_r = 0.4 m., b/2 = 3 m., $\lambda = 0$, $\Lambda = 0$, $\Gamma = 0$, $\theta = 0$, $\varphi = 0$).

Table 2.1 C_L, C_{DP} and C_{DI} results for pan3d.f and XFLR5 for different α (NACA 4412, c_r = 0.4 m., b/2 = 3 m., $\lambda = 0$, $\Lambda = 0$, $\Gamma = 0$, $\theta = 0$, $\varphi = 0$).

	pan3d.f		XFLR5	
angle of attack (α)	C_L	$C_{DP} + C_{DI}$	C_L	$C_{DP} + C_{DI}$
0	0.4104	0.0059	0.4191	0.006
2	0.5993	0.01728	0.6033	0.01553
4	0.7881	0.02032	0.7904	0.02183
6	0.9732	0.03105	0.9812	0.03224
8	1.1569	0.04393	1.1593	0.04678

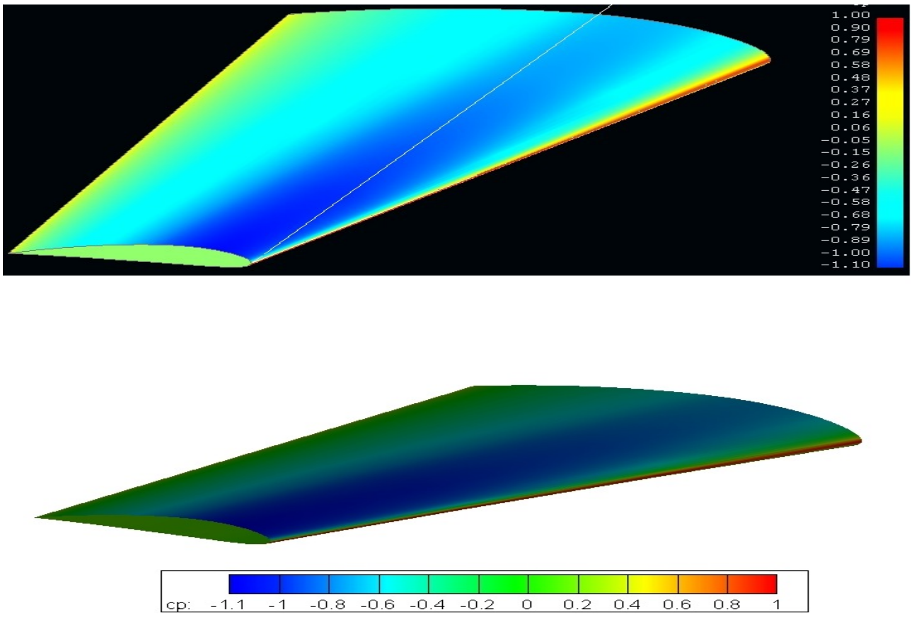

Figure 2.6 Wing B from XFLR5 (top), pan3d.f (bottom) (NACA 4412, c_r = 0.4 m., b/2 = 3 m., λ = 0.5, Λ = 5°, Γ = 5°, θ = 0, φ = 5°).

Table 2.2 C_L, C_{DP} and C_{DI} results for pan3d.f and XFLR5 for different α (NACA 4412, c_r = 0.4 m., b/2 = 3 m., λ = 0.5, Λ = 5°, Γ = 5°, θ = 0, φ = 5°).

	pan3d.f		XFLR5	
angle of attack (α)	C_L	$C_{DP} + C_{DI}$	C_L	$C_{DP} + C_{DI}$
0	0.6049	0.00985	0.6098	0.00977
2	0.7886	0.01673	0.7923	0.01698
4	0.9793	0.02539	1.0012	0.02618
6	1.1591	0.03579	1.1941	0.03727
8	1.3376	0.04789	1.3844	0.0501

As it is seen in Table 2.1, when the wing geometry is not complex like Wing A, pan3d.f results match very well with the results of XFLR5. This situation is also valid for small angles of attack when the geometry is getting more complex like Wing B. For higher angles of attack, the predictions of pan3d.f get different from

XFLR5 results according to the results in Table 2.2. But it is obvious that pand3d.f is a very useful tool as a fast aerodynamic solver for some geometries.

2.4 Wake Alignment

The geometry of a wake behind a wing is crucial for the application of the Kutta condition. Geometry of wake panels is obtained either by using the assumption that wake panels have zero net force ($C_{pwakepanels}=0$) [24] or wake streamlines should be tangent to the velocity vector [25]. In order to satisfy these assumptions, iterative procedures, which make the solution time longer, are applied. In addition to this, it is stated in Morino’s study that wake alignment has no significant role on wing loading, if the wing has no rotary motion [26]. In order to ensure this, two wake shapes are generated, which are seen in Figure 2.7.

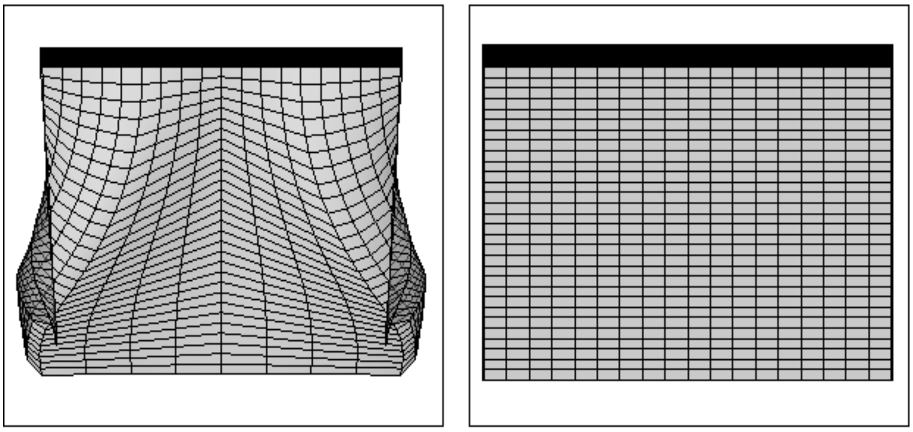

Figure 2.7 Rolled-up wake (left) and straight wake (right) alignment for a rectangular wing (NACA 4412 AR = 6).

The shape on the left, rolled-up wake, in Figure 2.7 is emulated according to Gaggero and Brizzolara’s study for a rectangular wing with aspect ratio 6 [27]. The alignment on the right, straight wake, is generated according to trailing edge coordinates of the wing.

2.4.1 Results

Results obtained with pan3d.f after these modifications are compared with Euler solver of FLUENT. For this, a rectangular wing with NACA 4412 profile, 1 m. chord and aspect ratio 6 was generated and meshed with GAMBIT, which is depicted in Figure 2.8.

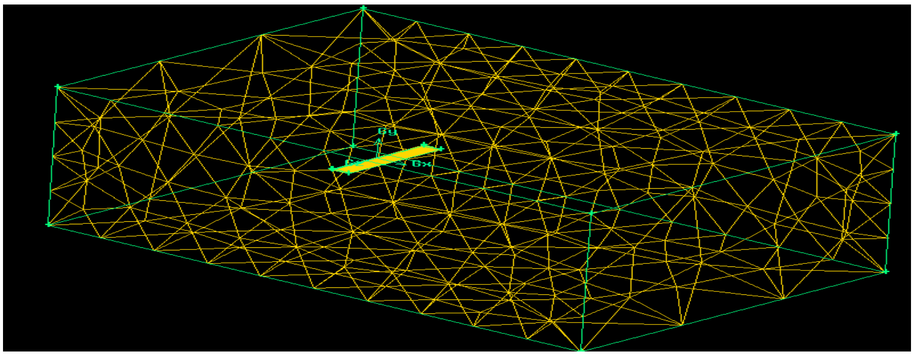

Figure 2.8 Mesh generated in GAMBIT (786584 triangular wall faces, 3956733 tetrahedral cells in domain).

Results obtained with Fluent are compared with pan3df. Figure 2.9 shows how pressure coefficient contours are in agreement.

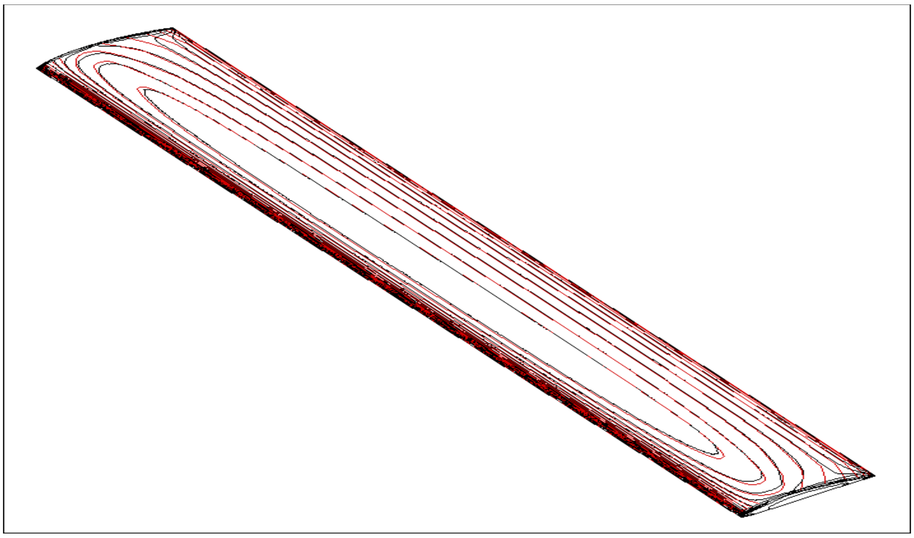

Figure 2.9 Comparison of pressure contours α=4° (− Fluent — pan3d.f, Straight Wake).

Table 2.3 shows the C_L, C_{DI} and C_{DP} results at different angle of attack values for FLUENT (F), rolled-up wake panel method (RW) and straight wake panel method (SW).

Table 2.3 C_L, C_{DP} and C_{DI} values that are obtained with FLUENT (F) and panel method, RW (Rolled-up wake), SW (Straight wake) at different angle of attack values.

	C_L			$C_{DI} + C_{DP}$		
α	F	RW	SW	F	RW	SW
0	0.3488	0.3505	0.3515	0.0125	0.0065	0.0066
2	0.5091	0.5098	0.5111	0.0201	0.0152	0.0155
4	0.6748	0.6672	0.6691	0.0314	0.0241	0.0238
6	0.8309	0.8222	0.8245	0.0462	0.0523	0.0519

Table 2.3 depicts that C_L results obtained with rolled-up wake and straight wake are very close to each other. In addition to this, the difference between these results and the results that are obtained with FLUENT is acceptable for the purposes of this study. It is difficult to say whether RW results are better than SW results or vice versa because at lower angle of attack values RW results are closer to FLUENT results whereas, SW results are closer at higher angle of attack values. On the other side, summation of induced drag and pressure drag coefficients of panel method are significantly different from FLUENT results.

2.5 Application of Iterative Kutta Condition

It is important to say that the flow around a lifting surface must leave from the trailing edge with a finite velocity. The classical method of Kutta condition is satisfied for 2-D flows by equating the tangential velocity at the lower and upper panels at the trailing edge that yields Equation 2.10. However, this method is inadequate for the satisfaction of Kutta condition in 3-D flows due to cross flow effect [27]. Therefore, Iterative Pressure Kutta (IPK) condition is applied in order to ensure a zero pressure difference at the trailing edge, Equation 2.12.

$$\Delta\mathrm{Cp} = \mathrm{Cp}^{+}_{\mathrm{T.E}} - \mathrm{Cp}^{-}_{\mathrm{T.E}} = 0 \tag{2.12}$$

Since the behavior of pressure is nonlinear, an iterative procedure is needed to satisfy the above equation. Since pressure is a function of vortex strengths of wakes (μ_l), Newton's formula for this iterative procedure is written as below [28]:

$$[\mu_l^{n+1}] = [\mu_l^{n}] + \left(\frac{[\Delta\mathrm{Cp}^{n}] - [\Delta\mathrm{Cp}^{n-1}]}{[\mu_l^{n}] - [\mu_l^{n-1}]}\right)[\Delta\mathrm{Cp}^{n}] \tag{2.13}$$

Iteration procedure is started with the initial values obtained by simple Kutta condition, Equation 2.10. As a result, μ_l^{n-1} and $\Delta\mathrm{Cp}^{n-1}$ values are obtained. μ_l^{n} is defined as follows:

$$[\mu_l^{n}] = t * [\mu_l^{n-1}] \text{ where } t \ll 0.1 \tag{2.14}$$

After employing this relation, $\Delta\mathrm{Cp}^{n}$ values are obtained. According to Equation 2.13, all values for the calculation of $\Delta\mathrm{Cp}^{n+1}$ are ready. Newton's formula is iterated until norm of $\Delta\mathrm{Cp}^{n+1}$ array is less than $5*10^{-3}$ [29]. During these analyses, two changes have been performed in order to decrease the solution time:

1. The influence coefficient matrices are generated using the symmetry law. The panel on one side of a wing has a symmetrical panel, which has the same vortex strength, on the other side of the wing with respect to wing root. As a result, the number of elements of matrix C_k is one fourth of the original C_k matrix.
2. During the application of IPK, Equation 2.8 is written in new matrix form for n^th iteration, which is shown in Equation 2.15.

$$[C_k][\mu_k^{n}] + [C_l][\mu_l^{n}] = -[B_k][\sigma_k] \tag{2.15}$$

Right side and influence coefficient values of the Equation 2.15 does not change due to no variation in body and wake geometries. By using Gauss elimination method for the solution of system of linear equations, μ_k^{n+1} values can be obtained. This is the first method. In the second method, Equation 2.15 is written for n+1st iteration and Equation 2.15 is subtracted from the new equation. This manipulation results in Equation 2.16.

$$[\mu_k^{n+1}] = [\mu_k^{n}] - [C_k]^{-1}[C_l]\left([\mu_l^{n+1}] - [\mu_l^{n}]\right) \tag{2.16}$$

By doing so, it is assumed that finding the inverse of C_k, by using the Gauss elimination method, and doing multiplication with right hand side vector once takes shorter time than solving linear system of equation, also by using Gauss elimination method, at each iteration [30].

2.5.1 Results

Before, revealing the results related with solution time, it is better to show the absolute ΔCp results (in logarithmic scale), which are obtained by simple Kutta condition for 2-D flows, on the trailing edge panels of the wing at the beginning of IPK procedure at 0 angle of attack, which is shown in Figure 2.10.

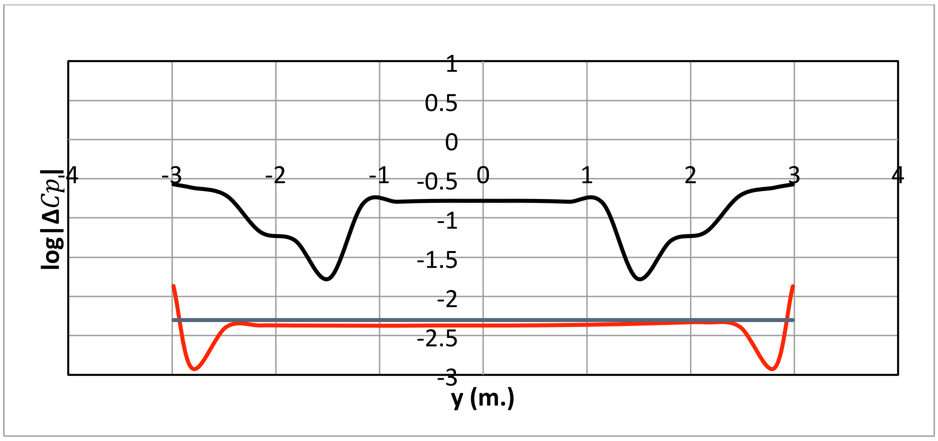

Figure 2.10 Absolute ΔCp at the trailing edge of the wing, (— (rolled-up), — (straight), — (convergence criteria)).

Figure 2.10 shows that when rolled-up wake alignment is used, pressure difference at the trailing edge is bigger, which requires higher number of iterations in order to satisfy the convergence criteria. Figure 2.11 shows the pressure coefficient distribution at the mid section of the wing with rolled-up wake that is depicted in Figure 2.7 when the angle of attack is 6.

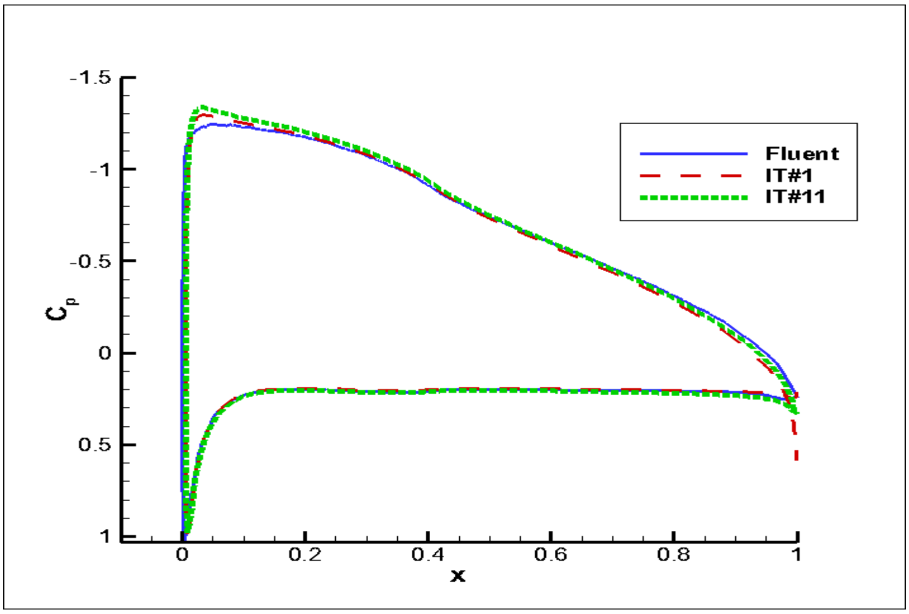

Figure 2.11 Pressure coefficient distribution at mid section.

According to the results, stopping criteria for iterative pressure Kutta condition is satisfied at 11th iteration. This method is important to satisfy the Kutta condition for 3-D flows. But, it changes the pressure coefficient results at the trailing edge, where the panel areas are small and increases the solution time significantly.

In order to investigate wake alignment and iterative pressure Kutta condition further, number of panels along half span (kp), chord (ip) and side of wing (ip/2) are altered and CPU time is measured, when the angle of attack is 0. The results can be seen in Table 2.4 and Table 2.5 for straight wake and rolled-up wake alignment, respectively. In these tables, elements of influence coefficient matrix for the wing, C_k, are altered by changing, kp or ip values. Multiplication result of CPU time for Gauss elimination method with iteration number for IPK is compared with CPU time for inverse of C_k, because inverse of C_k matrix is solved once, whereas Gauss elimination method is applied at each iteration during process.

Table 2.4 Straight wake results at different element number of A.

element # of A	CPU time (Gauss)	CPU time (C_k^{-1})	Iteration # for IPK
780 (kp=6, ip=120)	10.231	10.498	6
1260 (kp=10, ip=120)	50.124	51.495	7
1575 (kp=10, ip=150)	97.794	112.753	7
2100 (kp=17, ip= 120)	194.672	227.078	7

Table 2.5 Rolled-up wake results at different element number of A.

element # of A	CPU time (Gauss)	CPU time (C_k^{-1})	Iteration # for IPK
780 (kp=6, ip=120)	20.403	10.592	12
1260 (kp=10, ip=120)	100.247	51.604	14
1575 (kp=10, ip=150)	195.588	112.972	14
2100 (kp=17, ip= 120)	417.153	227.702	15

From the results two important conclusions can be drawn. Rolled-up wake alignment increases the solution time in order to satisfy the pressure Kutta condition because it provides higher initial values for the IPK when it is compared with straight wake alignment. In addition to this, when straight wake alignment is used, it is more convenient to use the linear system solver during IPK procedure in order to decrease the solution time. Use of this method becomes more favorable as the element number of C_k matrix increases. But, inverse of C_k should be applied if rolled-up wake alignment is used.

2.6 Conclusion

In this chapter, three dimensional panel theory is described briefly and the Fortran code, which is written by using this theory, is compared with XFLR5 results. In addition to this, algorithms of wake alignment and Iterative Pressure Kutta condition are implemented into the Fortran code and results related to them are discussed. Wake alignment is important for rotary wings and it gives high pressure coefficient difference for trailing edge. Therefore, straight wake alignment is preferred. Iterative Pressure Kutta condition is not used for further studies because it increases the solution time.

CHAPTER 3

TWO DIMENSIONAL BOUNDARY LAYER SOLVER

3.1 Introduction

In the introduction section of the previous chapter, it is mentioned that panel methods were coupled with boundary layer models in the 1980s. Eppler and Somers [31] used conformal mapping method for airfoil design and combined panel method and boundary layer method for aerodynamic loads. For boundary layer results, they solved both integral momentum and integral energy equations. Empirical expressions for velocity profiles were used in order to remedy the closure problem. In their studies, a certain value of the momentum thickness Reynolds number, which is dependent on the kinetic energy shape parameter, defined the location of transition. Laminar separation location is also defined as the transition location if it occurs before the transition location, which is defined previously. Turbulent separation location is defined as the location when energy shape parameter is greater than a certain value. Drag value was corrected by using modified Squire-Young formula and lift values were corrected by an empirical formula, which was a function of the separation location and the trailing edge slope that is seen in Figure 3.1.

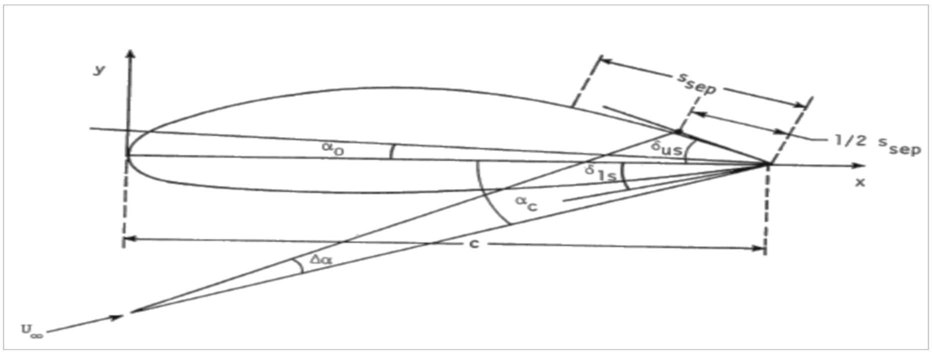

Figure 3.1 Lift coefficient correction due to separation [31].

In their study, one way coupled method, in which panel method velocity distribution is used in order to make the boundary layer analysis at one iteration without taking into consideration of thickness of boundary layer profile for the velocity profile, was used. The other method is the two way coupled method. In this method, two approaches are used. In the first approach, panel method results are fed into boundary layer model and boundary layer thickness is obtained. Airfoil shape is modified by using this thickness and panel method results are obtained by using the modified shape and new boundary layer results are obtained. This iteration process continues until a converged solution is obtained. In the second approach, normal velocity is defined as a function of displacement thickness, which is defined as zero for potential flow [32].

Drela and Giles [33] studied boundary layers for transonic flows. In their study, they coupled inviscid Euler equations with discrete boundary layer equations and coupling problem was solved by using Newton method. In the study, e^n method that is based on the amplification theory of the Orr-Sommerfeld equation was used. By using Falkner–Skan velocity profiles, Orr-Sommerfeld equation was solved for different momentum shape parameters and unstable frequencies and integrated rates were approximated by straight lines as it is seen in Figure 3.2.

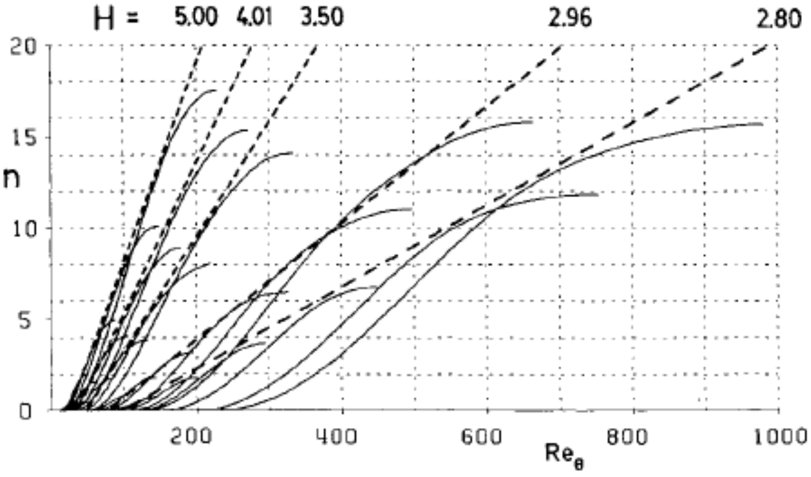

Figure 3.2 Orr-Sommerfeld spatial amplification curves [33].

The n value, which was chosen as 9 in the study, that is name of the vertical axis in Figure 3.2 is the logarithm of the maximum amplification ratio and its value is found by using empirical formulations for the straight lines. In Figure 3.3, how their results are in good agreement with experimental results are shown.

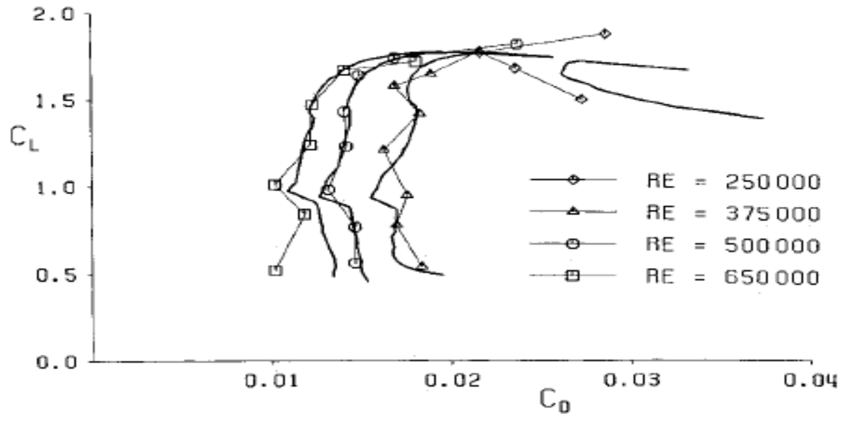

Figure 3.3 Calculated (bold) and experiential (symbols) drag polar for LNV109A airfoil [33].

Wang and Shan [34] followed almost exactly the same aerodynamic analysis utilized in this thesis. They used one way coupled method by using three dimensional panel method and boundary layer models. In their studies, Thwaites' method is used as the model for the laminar boundary layer region, whereas Head's method is used for the turbulent region. Transition from laminar to turbulent flow is either found by the e^n transition prediction method or laminar separation location is accepted as the starting location of the turbulent region. However, correction of drag due to turbulent separation is not mentioned in their study. They obtained the optimum shape of the airship body, which had a length of 367.9 m, which is shown in Figure 3.4, by using a hybrid genetic algorithm that is composed of the genetic algorithm and Nelder–Mead simplex search method.

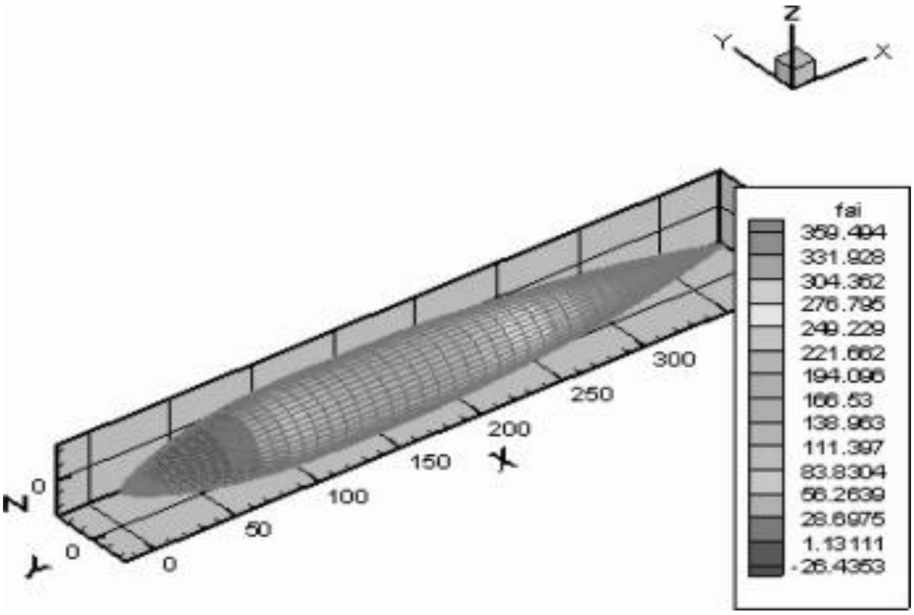

Figure 3.4 Velocity potential distribution of optimum airship body [34].

The boundary layer modeling in this thesis is very similar to the modeling in Wang and Shan. Thwaites method is used for the laminar region. Transition location is decided by using e^n transition prediction method or laminar separation location, which is according to a certain value of momentum shape factor, is defined as the start of turbulent boundary layer. Head’s Method is used for the turbulent boundary layer. Turbulent separation is decided for a certain value of the momentum shape factor, which is the same process for laminar separation. Skin friction is assumed to be zero downstream of the turbulent separation point, whereas in reality the separation is accompanied by an increase in drag and a decrease in lift. Therefore, drag and lift correction functions are used. As a result of this, a two dimensional boundary layer solver, 2DBLS, is obtained.

3.2 Theory

3.2.1 Laminar Boundary Layer

Modeling of the laminar boundary layer starts with Von Karman's momentum integral equation presented in Equation 3.1.

$$\frac{d\theta}{dx}+\frac{\theta}{V_e}(2+H)\frac{dV_e}{dx}=\frac{1}{2}c_f \tag{3.1}$$

If both sides of the equation is manipulated so that $Re_\theta = \rho V_e \theta/\mu$ and rewritten according to the parameter that is defined by Thwaites as $l = 0.5Re_\theta c_f$ and $\lambda = (\rho\theta^2/\mu)(dV_e/dx)$, Equation 3.2 is obtained [35].

$$\frac{\rho V_e}{\mu}\frac{d\theta^2}{dx} = 2[l-(2+H)\lambda] \tag{3.2}$$

Thwaites found a relation for the right hand side of Equation 3.2 by using Pohlhausen's quadratic velocity profile, shown in Equation 3.3 [35].

$$2[l-(2+H)\lambda] \approx 0.45-6\lambda \tag{3.3}$$

If Equation 3.3 is substituted into Equation 3.2, λ is rewritten in expanded form and both sides of the equation is multiplied by V_e^5, Equation 3.4 is obtained [35].

$$\frac{\rho}{\mu}\frac{d}{dx}(\theta^2 V_e^6) = 0.45V_e^5 \tag{3.4}$$

Since Equation 3.4 is a first order ordinary differential equation, it needs an initial condition, which is given in Equation 3.5 [35].

$$\theta(0) = \sqrt{\frac{0.075\mu}{\rho \frac{dV_e}{dx}}} \tag{3.5}$$

Since the initial condition is known, Equation 3.4 is solved by numerical integration with the correlation of Cebeci and Bradshaw for Thwaites equations for $l(\lambda)$ and $H(\lambda)$, that are given in Equation 3.6 and Equation 3.7, respectively [35].

$$\begin{aligned} l(\lambda) &= 0.22 + 1.57\lambda - 1.8\lambda^2 \text{ for } 0 < \lambda < 0.1 \\ l(\lambda) &= 0.22 + 1.402\lambda + 0.018\lambda/(\lambda + 0.107) \text{ for } -0.1 < \lambda < 0 \end{aligned} \tag{3.6}$$

$$\begin{aligned} H(\lambda) &= 2.61 - 3.75\lambda + 5.24\lambda^2 \text{ for } 0 < \lambda < 0.1 \\ H(\lambda) &= 2.08 + 0.0731\lambda/(\lambda + 0.14) \text{ for } -0.1 < \lambda < 0 \end{aligned} \tag{3.7}$$

3.2.2 Transition from Laminar to Turbulent Flow

By using the linear stability theory, the envelopes of the amplification rate for n versus Re_θ by straight lines are approximated. The approximation is expressed by Equation 3.8, Equation 3.9 and Equation 3.10 [36].

$$n = \frac{dn}{dRe_\theta}(Re_\theta - Re_{\theta crit}) \tag{3.8}$$

$$\frac{dn}{dRe_\theta} = 0.028(H - 1) - \frac{0.0345}{e^{-(\frac{3.87}{H-1} - 2.52)^2}} \tag{3.9}$$

$$\log_{10}(Re_{\theta crit}) = 0.7\tanh\left(\frac{14}{H-1} - 9.24\right) + 2.492\left(\frac{1}{H-1}\right)^{0.43} + 0.62 \tag{3.10}$$

During development of the boundary layer in laminar region, when λ=-0.0842, laminar separation is predicted. When this situation occurs, algorithm assumes that transition from laminar region to turbulent region is obtained [35].

3.2.3 Head’s Method for Turbulent Region

Head’s method is based on the entrainment velocity concept that increases the volume flow rate in the boundary layer. In this method, a new shape parameter is defined as shown in Equation 3.11 [35].

$$H_1 = \frac{\delta - \delta^*}{\theta} \tag{3.11}$$

Cebeci and Bradshaw set the following formulas after several experiments, Equation 3.12 and Equation 3.13 [35].

$$\frac{1}{V_e}\frac{d}{dx}(V_e \theta H_1) = 0.0306(H_1 - 3)^{-0.6169} \tag{3.12}$$

$$\begin{aligned} H_1 &= 3.3 + 0.8234(H - 1.1)^{-1.287} \text{ for } H \leq 1.6 \\ H_1 &= 3.3 + 1.5501(H - 0.6778)^{-3.064} \text{ for } H > 1.6 \end{aligned} \tag{3.13}$$

If Von Karman’s momentum integral formula is taken into account, in order to solve the unknowns, which are θ, H, H_1 and c_f, a fourth equation is needed, which is given in Equation 3.14 [35].

$$c_f = 0.246 * 10^{-0.678H} Re_\theta^{-0.268} \tag{3.14}$$

System of equations is solved by 2nd order Runge-Kutta Method. When H value is greater than 2.4, it is predicted that turbulent separation starts [35].

3.2.4 Separation Correction Functions for Lift and Drag

Skin friction is assumed to be zero downstream of the turbulent separation point, whereas in reality the separation is accompanied by an increase in drag and a decrease in lift. Therefore, lift and drag correction functions are defined. For lift, a linear correction function that is shown in Equation 3.15 is used [36].

$$L = L(1 - 0.2(x_{te} - x_{sep})) \tag{3.15}$$

The above equation is valid and used for both upper and lower part of each wing strip. It is always active in order to take into account the effect of shape changes on lift during optimization problem. In Figure 3.5, the effect of lift correction can be observed on the baseline wing in the optimization problem.

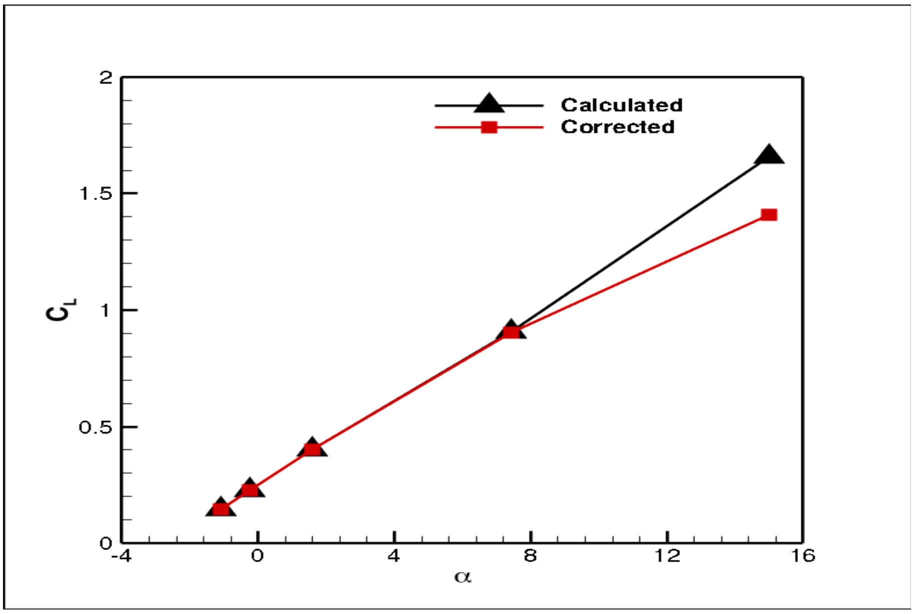

Figure 3.5 Calculated and corrected C_L values for baseline wing.

Eppler's modified Square-Young formula [31] is used for drag correction, which is shown in Equation 3.16.

$$D = D(\frac{U_{sep}}{U_{te}})^{0.15} \tag{3.16}$$

In Equation 3.16, U_{sep} and U_{te} are the velocities at separation location and trailing edge, respectively. During the optimization process, it is observed that the optimization solver tends to produce a bump on airfoil at locations that are close to the leading edge, where panel velocities are close to the trailing edge velocity, in order to promote separation. By doing this, flow separates very early and skin friction coefficient values after separation become 0. In addition to this, since separation velocity value is close to trailing edge velocity, effectiveness of Equation 3.16 reduces. In order to overcome this problem two changes are applied;

1. If separation develops before 75% of the chord, the skin friction coefficient values of the panels that are downstream of the separation location are taken as 90% of the previous panel skin friction coefficient value,
2. Modify Equation 3.16 as is shown in Equation 3.17.

$$D = D(\frac{X_{te}}{X_{sep}})^{0.15} \tag{3.17}$$

Equation 3.17 is active and used for both upper and lower surface of the wing strip in the same manner as lift correction.

3.3 Comparison of the Results with XFOIL

XFOIL is an aerodynamic analysis program that initially calculates inviscid panel edge velocities, which are fed into boundary layer model until zero normal velocity condition for boundary layer model is satisfied, as it is described in the introduction part of this chapter [37]. However, 2DBLS is a one way solver and boundary layer is modeled by using inviscid panel edge velocities. For comparison, airfoil shape and panel edge velocities are taken from XFOIL for NACA 4412 airfoil for angle of attack values of 0, 4, 8 and 12 for 151 nodes at Re=266000 and they are provided as input data for 2DBLS. After that, the skin friction and momentum thickness results are compared for given angle of attack values. In the subsequent graphs, x values between -1 and 0 (from trailing edge to leading edge) shows the lower surface, whereas results between 0 and 1 (from leading edge to trailing edge) depict the upper surface. Figure 3.6, Figure 3.7, Figure 3.8 and Figure 3.9 depict skin friction coefficient and momentum thickness comparison results of 2DBLS and XFOIL for angle of attack values of 0, 4, 8 and 12, respectively.

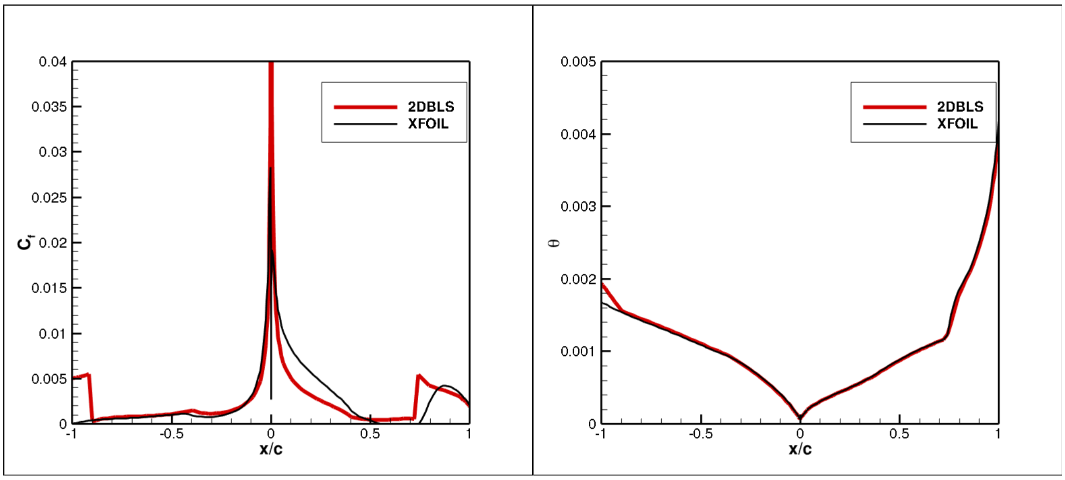

Figure 3.6 Skin friction coefficient (left) and momentum thickness (right) comparison for $\alpha=0^o$.

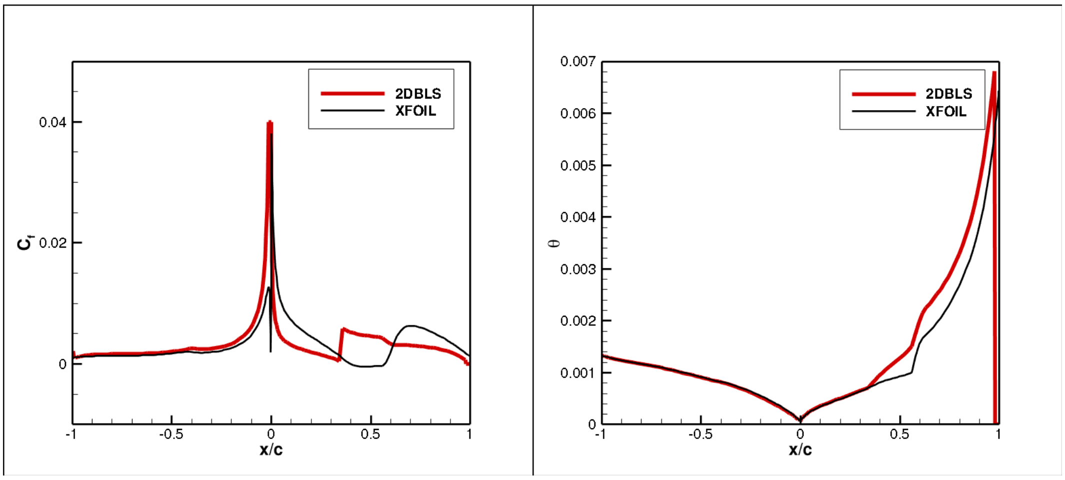

Figure 3.7 Skin friction coefficient (left) and momentum thickness (right) comparison for α=4°.

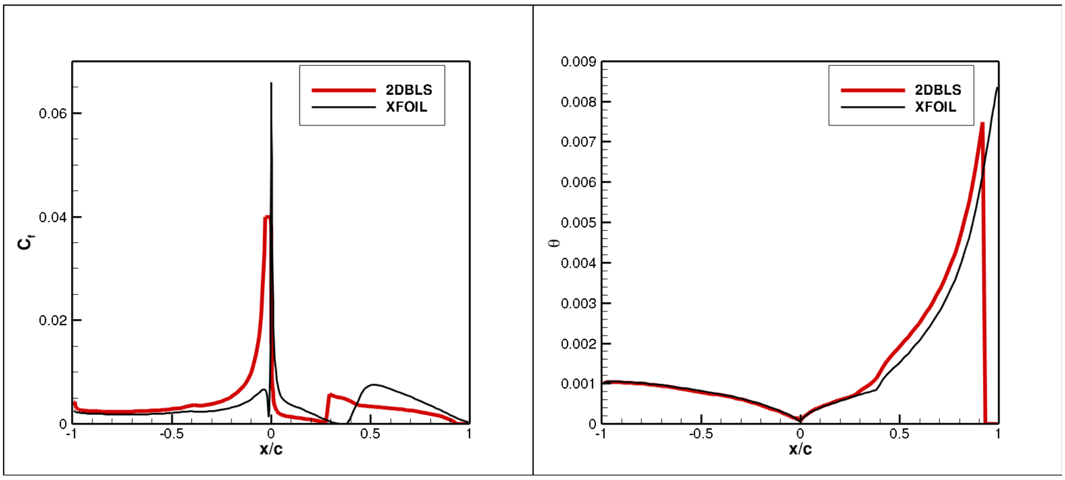

Figure 3.8 Skin friction coefficient (left) and momentum thickness (right) comparison for α=8°.

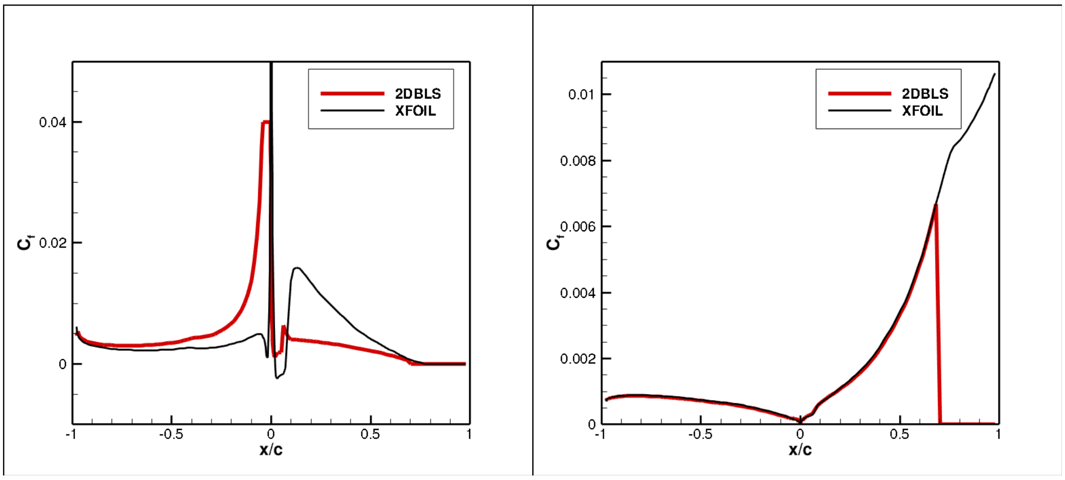

Figure 3.9 Skin friction coefficient (left) and momentum thickness (right) comparison for α=12^o.

According to the results shown in the figures above, skin friction coefficient results are different especially near the leading edges of both upper and lower surfaces. But it should be stated that formulas for calculation of skin friction results are completely different because velocity profiles that are used in order to obtain these formulas are different. The sudden increment in skin friction coefficient values shows transition locations. Momentum thickness results of 2DBLS are close to XFOIL momentum thickness results up to the transition location. After transition location, 2DBLS results get different from XFOIL results. Comparison of transition and separation locations and total skin friction drag coefficients are given in Table 3.1.

Table 3.1 Comparison of XFOIL and 2DBLS.

	XFOIL				2DBLS			
α	X_{trup}	X_{trlow}	X_{sepup}	Cd_f	X_{trup}	X_{trlow}	X_{sepup}	Cd_f
0	0.737	-	-	0.00517	0.750	0.908	-	0.00574
4	0.557	-	-	0.00651	0.367	-	0.978	0.00683
8	0.373	-	-	0.00644	0.301	-	0924	0.00785
12	0.084	-	0.806	0.00749	0.066	-	0.692	0.00872

According to results in Table 3.1, 2DBL skin friction drag results are always higher than XFOIL results. This difference increases as angle of attack increases because 2DBLS finds turbulent separation except for $\alpha=0^o$. As it is discussed above, when there is turbulent separation drag correction is active. As a result of this, higher skin friction coefficient results are found. Upper surface laminar to turbulent transition locations are close to each other except for 4 degree angle of attack. For 12 degree, XFOIL does not output a turbulent separation but, when the results are carefully investigated, it is seen that skin friction coefficient values are negative after 0.806c. Therefore, this location is defined as turbulent separation location.

3.4 Conclusion

In this chapter, theory of 2-D boundary layer solver is described and its results are compared with XFOIL program. In the comparison part, it is observed that the results of two solvers are in agreement even if the angle of attack values are high. The difference between results increases as angle of attack values increases but they are still similar. Penalty function for lift makes the solver more realistic by taking into account the separation location for lift calculation. In the optimization part, it is observed that correction function for drag promotes attached flow.

CHAPTER 4

GENERALIZED REDUCED GRADIENT METHOD

4.1 Introduction

Generalized reduced gradient method (GRGM) is an extension of the reduced gradient method, which solves only equality constrained optimization problems [38]. It was developed by Leon Lasdon from the University of Texas at Austin, and Allan Waren from the Cleveland State University and Microsoft Excel Solver uses this method for nonlinear optimization problems [39]. In this thesis, generalized reduced gradient method is used due to its ability to maintain feasibility with respect to nonlinear constraints [40].

4.2 Theory

4.2.1 Generalized Reduced Gradient Method

In order to understand the details of generalized reduced gradient method, consider the following nonlinear optimization problem [41]:

$$\text{Minimize } f(X) \tag{4.1}$$

subject to

$$h_j(X) \leq 0 \quad j = 1,2, \dots \dots, m \tag{4.2}$$

$$d_k(X) = 0 \quad k = 1,2, \dots \dots, l \tag{4.3}$$

$$x_i^l \leq X_i \leq x_i^u \quad i = 1,2, \dots \dots, n \tag{4.4}$$

In Equation 4.1, f(X) is the objective function that will be minimized and X is the design variables. In Equation 4.2, m is the number of inequality constraints, h. In Equation 4.3, l is number of equality constraints, d. n is number of design variables that have upper limit, x^u, and lower limit, x^l, in Equation 4.4. Since generalized reduced gradient method theory is based on finding optimum design variables while all constraints are active, which means all constraints are equal to 0, the nonlinear optimization problem outlined above is rewritten by adding nonnegative slack variables to inequality constraints.

Equation 4.6 is obtained by summing equality constrains and slack variables added inequality constraints, which become equality constraints. Equation 4.7 is the rewritten form of Equation 4.4 by adding slack variables. Upper bound for slack variables has no limit whereas lower bound is 0.

$$\text{Minimize } f(X) \tag{4.5}$$

subject to

$$g_j(X) = 0 \quad j = 1,2, \dots \dots, m + l \tag{4.6}$$

$$x_i^l \leq x_i \leq x_i^u \quad i = 1,2, \dots \dots, m + n \tag{4.7}$$

The idea behind GRG method is to eliminate the variables by using Equation 4.6. Therefore, it is required to divide design variables into 2 groups:

$$\mathrm{X} = \begin{Bmatrix} \mathrm{Y} \\ \mathrm{Z} \end{Bmatrix} = \begin{matrix} \text{Basic Variables} \\ \text{Nonbasic Variables} \end{matrix} \tag{4.8}$$

If first derivative of objective function and constraints are written according to this division:

$$\mathrm{df(X)} = \sum_{i=1}^{n-l} \frac{\partial f}{\partial y_i} dy_i + \sum_{i=1}^{m+l} \frac{\partial f}{\partial z_i} dz_i = \nabla_Y^T f dY + \nabla_Z^T f dZ \tag{4.9}$$

$$dg_i(X) = \sum_{j=1}^{n-l} \frac{\partial g_i}{\partial y_j} dy_j + \sum_{j=1}^{m+l} \frac{\partial g_i}{\partial z_j} dz_j = [C]dY + [D]dZ \tag{4.10}$$

Generalized reduced gradient method is based on the satisfaction of all constraints. Any change of a design variable should be compensated by the other design variables so that constraint is satisfied or constraints are satisfied. This yields the left side of the Equation 4.10 is zero and Equation 4.11 is obtained.

$$dZ = -[D]^{-1}[C]dY \tag{4.11}$$

If Equation 4.9 is manipulated by using Equation 4.10, following formula is obtained:

$$\frac{df(X)}{dY} = G_r = \nabla_Y^T f - [D]^{-1}[C]\nabla_Z^T f \tag{4.12}$$

G_r in the above equation is the generalized reduced gradient vector. Geometrically, the reduced gradient can be described as a projection of the original n-dimensional gradient onto the (n-m)-dimensional feasible region described by the basic variables [42]. G_r value is used in order to find a suitable search direction (S) for minimization of objective function. For example, if steepest descent method is used, S is described as follows:

$$\mathrm{S} = -\mathrm{G_r} \tag{4.13}$$

If $||\mathrm{S}||$ is less than some certain value algorithm is considered to have converged and current X values are taken as optimum design variables of the problem. During the search direction analysis, upper and lower bounds of X should be taken into account. For this, Equation 4.13 is modified as follows:

$$\mathrm{S} = \begin{cases} 0 \text{ if } \mathrm{Y_i} = \mathrm{Y_i^u} \text{ and } \mathrm{G_{r_i}} < 0 \\ 0 \text{ if } \mathrm{Y_i} = \mathrm{Y_i^l} \text{ and } \mathrm{G_{r_i}} > 0 \\ \quad -\mathrm{G_{r_i}} \text{ otherwise} \end{cases} \tag{4.14}$$

S is the search direction vector for basic variables. For nonbasic variables T vector is defined by using Equation 4.15.

$$\mathrm{T} = -[\mathrm{D}]^{-1}[\mathrm{C}]\mathrm{S} \tag{4.15}$$

4.2.2 Step Length Selection

In order to find how far the algorithm will move on the search direction, optimal step length (λ) should be found. This can be done by both looking at the upper and lower limits of the basic and nonbasic design variables and finding the upper limit of value of the optimum step length, which makes the objection function minimum at current X, S and T values, by using Equation 4.16.

$$\lambda_i = \begin{cases} \dfrac{Y_i^u - Y_i}{S_i} & \text{if } S_i > 0 \\ \dfrac{Y_i^l - Y_i}{S_i} & \text{if } S_i < 0 \end{cases}$$

$$\lambda_i = \begin{cases} \dfrac{Z_i^u - Z_i}{T_i} & \text{if } T_i > 0 \\ \dfrac{Y_i^l - Y_i}{T_i} & \text{if } T_i < 0 \end{cases} \tag{4.16}$$

4.2.2.1 Golden Search Method

Among step length values that are obtained by Equation 4.16, minimum one is chosen as upper bound step size for one dimensional search algorithm. The lower bound is zero. In this thesis, golden search method is used as one dimensional search algorithm [38]. However, this algorithm can procedure a local minimum, which is seen in Figure 4.1 [43].

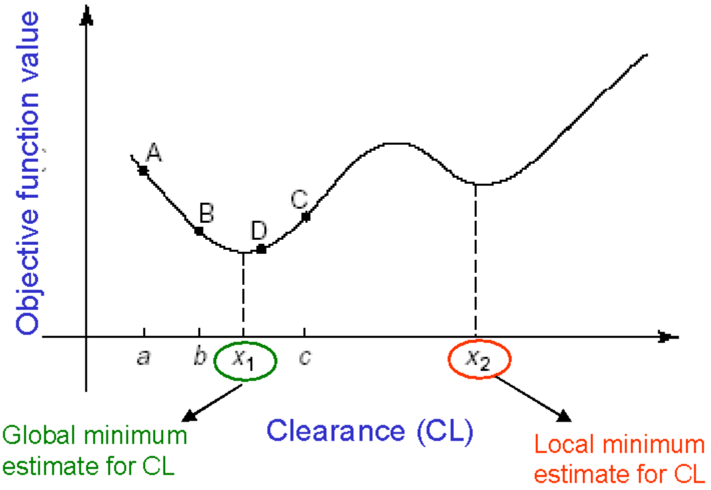
Objective function value
A
B
C
D
a
b
x_1
c
x_2
Global minimum estimate for CL
Clearance (CL)
Local minimum estimate for CL

Figure 4.1 Local or global estimation of Golden search method [43].

In order to prevent this situation, objective function domain is searched for nearly global optimum location by decreasing the initial step length value to 70% of it at each iteration, which is performed 10 times. When minimum objective function is obtained, previous step length value is defined for the upper bound and the lower bound is defined as the next step length value for golden search algorithm. According to Figure 4.1, this procedure is explained as follows; for nearly global optimum location point D is found. After that, point C is defined as the upper bound and point A is defined as the lower bound for the golden search algorithm.

In golden search algorithm, optimum step length value is found by evaluating the value of the objective function at intermediate step length values that are obtained by golden section ratio, expressed as in Equation 4.17 and Equation 4.18 [38].

$$\lambda_1 = 0.61803\lambda_l + 0.38197\lambda_u \tag{4.17}$$

$$\lambda_2 = 0.38197\lambda_l + 0.618037\lambda_u \tag{4.18}$$

If the objective function value for λ_1 is grater than the objective function value λ_2, minimum objective function should be at the right of λ_1, because objective is decreasing from λ_1 to λ_2. As a result, new lower bound for next iteration becomes λ_1. In adverse conditon, new upper bound would be λ_2. After finding optimal step length new design variables are found according to the formula in Equation 4.19.

$$X_{new} = \begin{matrix} Y + \lambda S \\ Z + \lambda T \end{matrix} \tag{4.19}$$

4.2.3 Selection of Basic and Nonbasic Variables

First difficulty that was faced in the development process is related to how basic and nonbasic variables are defined. Ravindran et al. choose basic and nonbasic variables without considering whether they are design or slack variables. In the method, the distance between variables and their lower and upper bounds is calculated. After that, variables that are farthest from their boundaries are taken as basic variables.

Remaining ones are nonbasic variables [42]. However, Rao defines slack variables at the beginning of array of elements to be chosen. Then, design variables are added to this array with the same method of Ravindran et al. [41]. It is important to mention that defining basic and nonbasic variables should be performed at each iteration of the optimization process.

4.2.4 Algorithm for Going Back to Feasible Region

Another difficulty arises when initial design variables are in the infeasible region. Vanderplaats states that Equation 4.20 can be used to overcome this problem [38].

$$\mathrm{X}_{\mathrm{infeasible}}^{\mathrm{i+1}} = \mathrm{X}_{\mathrm{infeasible}}^{\mathrm{i}} - [\mathrm{D}]^{-1}\mathrm{g}(\mathrm{X}) \tag{4.20}$$

For this procedure Newton Method is used. After finding the optimum λ value, new X values are found, a feasible region check is applied. If any of the constraints is in the infeasible region, Newton method is used to pull back the infeasible constraint to feasible region. Above iteration continues until all constraints appear in the feasible region.

However, Chinneck's study shows that it is more appropriate to find a feasibility vector among the currently violated constraints and achieve feasibility instead of using all constraints without checking whether they are in the infeasible region or not [44]. The details of Chinneck's method need the feasibility vector for violated constraints and design variables are in these constraints. After that, components of feasibility vector are summed and divided to the number of design variables that exist in violated constraints for each design variable. Design variables are updated by adding the previous design variables values and results that are obtained by this division. The fact that if design variables exceed their bounds, they should be reset to the nearest bound is a remarkable point of method [45].

4.3 Comparison of the Results for A Structural Optimization Problem

The following example is an optimization problem for minimum material volume in a structural design under load due to the 50000 N, P, force at tip, which is shown in Figure 4.2 [38].

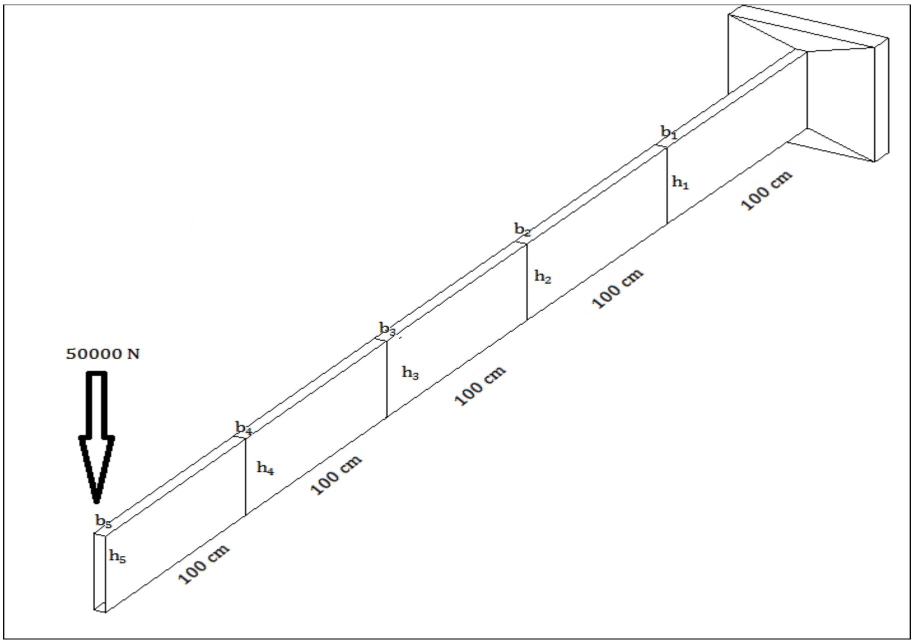

Figure 4.2 Cantilevered beam.

The design parameters are the width, b, and height, h, at each of the N segment, where N=5. It is asked to find the minimum weight of the system subject to limits on bending stress (σ) (14000 N/cm^2) at right end of each segment according to the side view in Figure 4.2 and tip deflection under load (y_5) (2.5 cm) and the geometrical requirement that the height of any segment does not exceed twenty times the width. Each segment has a length of 100 cm, l. Total length, L, is 500 cm. Young's modulus, E, is same for all segments that is $2\times10^7\ \mathrm{N/cm^2}$. The moment of inertia value, I, for segment i is shown in Equation 4.21.

$$I_i = \frac{b_i h_i^3}{12} \tag{4.21}$$

The deflection, y_i, and derivative of deflection, y_i', at the left end of segment i is found by using Equation 4.22 and Equation 4.23, respectively.

$$y_i = \frac{P l_i^2}{2EI_i}\left[L - \sum_{j=1}^{i} l_j + \frac{2l_i}{3}\right] + y_{i-1}' l_i + y_{i-1} \tag{4.22}$$

$$y_i' = \frac{P l_i}{EI_i}\left[L + \frac{l_i}{2} - \sum_{j=1}^{i} l_j\right] + y_{i-1}' \tag{4.23}$$

At the right end of first segment, fix boundary condition is applied. The bending Moment, M, at the right end and corresponding bending stress of segment i are found according to the formula in Equation 4.24 and Equation 4.25, respectively.

$$M_i = P\left[L + l_i - \sum_{j=1}^{i} l_j\right] \tag{4.24}$$

$$\sigma = \frac{M_i h_i}{2I_i} \tag{4.25}$$

As a result, mathematical definition of optimization problem is defined in Equation 4.26.

$$\text{Min} \quad f(X) = V = \sum_{i=1}^{5} b_i h_i l_i$$

$$\sigma_i - 14000 \leq 0 \quad i = 1, N$$

$$y_5 - 2.5 \leq 0 \tag{4.26}$$

$$h_i - 20b_i \leq 0 \quad i = 1, N$$

$$b_i \geq 1 \quad i = 1, N$$

$$h_i \geq 5 \quad i = 1, N$$

In this part, results are discussed according to the order of optimization procedure. The values of initial design variables are 5 cm and 40 cm for width and height of segments. As a result of this, constraints are not in feasible region. As a beginning, it is important to see how initial design variables in infeasible region are taken back to the feasible region. Figure 4.3 and Figure 4.4 show the variation σ and y_5 values during this procedure.

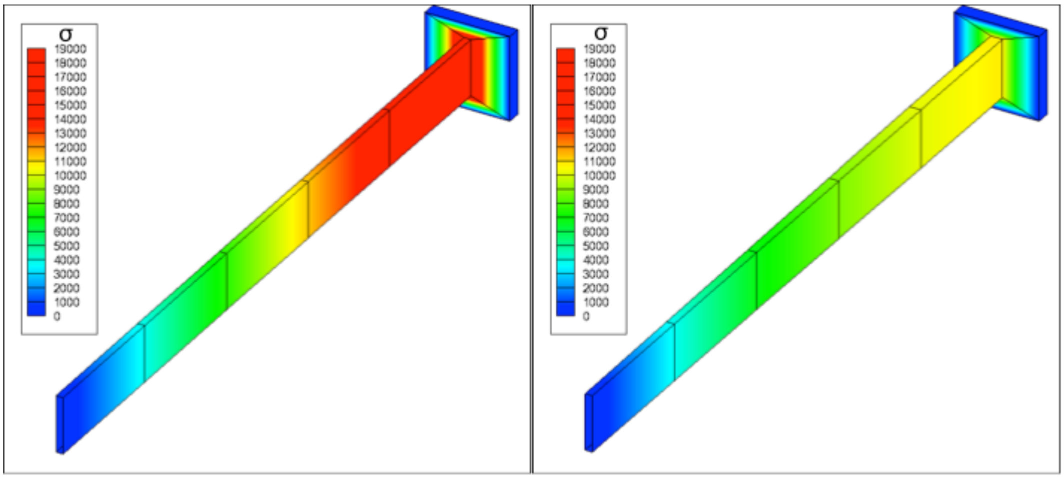
σ
19000
18000
17000
16000
15000
14000
13000
12000
11000
10000
9000
8000
7000
6000
5000
4000
3000
2000
1000
0
σ
19000
18000
17000
16000
15000
14000
13000
12000
11000
10000
9000
8000
7000
6000
5000
4000
3000
2000
1000
0

Figure 4.3 σ values according to initial infeasible design variables (left) and initial feasible design variables (right).

According to the results in Figure 4.3, bending stress at the right end of first segment of the cantilever beam decrease from around 19000 N/cm^2 to around 11000 N/cm^2.

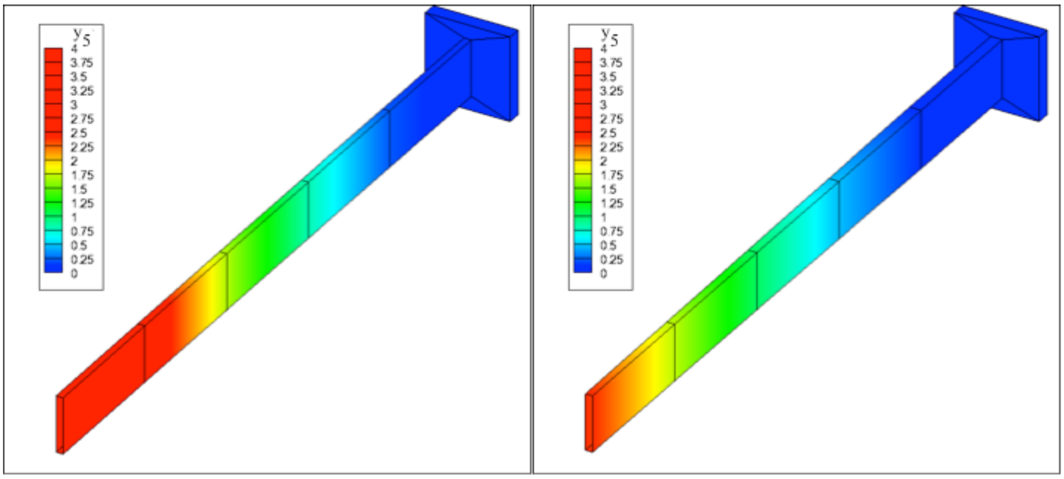

Figure 4.4 y_5 values according to initial infeasible design variables (left) and initial feasible design variables (right).

Results in Figure 4.4 shows the tip deflection at the left end of each segment. Since the tip deflection at the left end of fifth segment is a constraint, the results are shown as y_5. Results reveal that y_5 decreases from around 4 cm to around 2.5 cm after constraints are taken back to feasible region.

The algorithm that is developed by generalized reduced gradient method is compared with the following methods [38]:

1. Genetic search of EVOLVE software
2. Sequential linear programming of DOT optimization software contained in the visualDOC PROGRAM,
3. Method of feasible directions of ADS research program,
4. Generalized reduced gradient method of ADS research program,
5. Modified feasible directions method of DOT optimization software contained in the visualDOC PROGRAM,
6. Sequential quadratic programming of DOT optimization software contained in the visualDOC PROGRAM.

Method 7 and Method 8 are the developed methods. In former method, Ravindran's selection is used, while in latter, Rao's selection is used. Iteration history of optimization problem and comparison of the results can be seen in Table 4.1.

Table 4.1 Iteration history of the methods (cm^3 volume at iterations).

Iteration number	Methods							
	1	2	3	4	5	6	7	8
0	0	100000	100000	100000	100000	100000	100000	100000
1	56680	60805	106425	104500	110735	88901	130840	130840
2	56680	59351	111014	95849	88454	69929	116690	107326
3	56.60	64753	92922	93329	80427	64284	97300	94321
4	71570	64732	82511	76763	71711	64628	91059	81425
5	71570	64097	73805	68960	69500	64694	82895	78546
6	71590	64418	70683	67445	67843	65480	80526	73454
7	71590	64294	69540	65898	67636	65436	73123	71221
8	66880	64519	68133	65814	66362	65427	69270	68543
9	66880	64434	66830	65422	65426	-	65780	66716
10	66880	65530	65906	65399	65425	-	65949	65860
11	66880	65493	65906	65399	65425	-	65478	65590
Iterations	6667	12	18	11	11	8	20	12

According to the results in Table 4.1, Method 7 and Method 8 reach the optimum value, when it is compared with other methods. However, Method 7's iteration number is highest among them. Method 8 reaches optimum value at less iteration number when it is compared with Method 7. But, this method also is slow when it is compared with other methods. This could be due to the algorithm, which is used for movement from infeasible region to feasible region. If a better method is applied, all design variables reach feasible region without increasing objective function value too much. Values of optimum design variables are tabulated in Table 4.2, respectively.

Table 4.2 Optimum design variable values.

Variables	Methods								
	Initial	1	2	3	4	5	6	7	8
b_1	5.00	3.12	3.10	3.14	2.99	3.13	3.14	3.146	3.132
b_2	5.00	2.91	2.87	2.89	2.78	2.88	2.88	2.886	2.925
b_3	5.00	2.62	2.64	2.59	2.52	2.58	2.57	2.537	2.532
b_4	5.00	2.25	2.21	2.21	2.20	2.21	2.20	2.237	2.234
b_5	5.00	1.76	1.75	1.76	2.19	1.75	1.75	1.753	1.796
h_1	40.00	62.48	61.96	62.68	59.84	62.67	62.82	62.925	62.634
h_2	40.00	58.12	57.37	57.71	55.55	57.66	57.61	57.712	58.422
h_3	40.00	50.00	52.87	51.67	50.48	51.60	51.47	50.826	50.624
h_4	40.00	45.00	44.20	44.10	44.09	44.09	44.09	44.125	44.712
h_5	40.00	35.17	34.99	35.03	34.84	35.00	35.03	35.068	36.122

According to the results in Table 4.2, it is observed that there are some differences between the values of optimum design variables that are obtained by the developed solver and by the solvers in the literature. These differences are mainly due to selection of the bounds of the optimization solver.

Figure 4.5 and Figure 4.6 show σ values for initial feasible and optimum design variables that are obtained via Method 7 and Method 8, respectively.

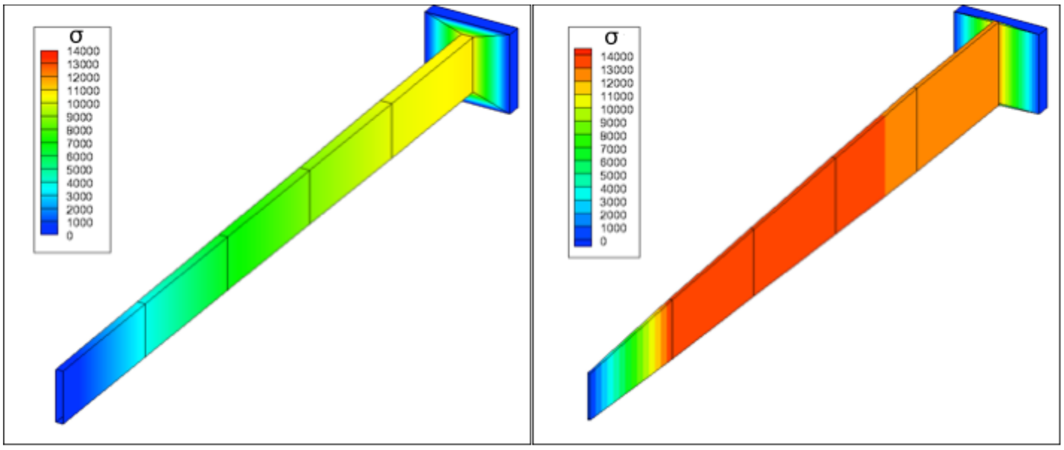
σ
14000
13000
12000
11000
10000
9000
8000
7000
6000
5000
4000
3000
2000
1000
0
σ
14000
13000
12000
11000
10000
9000
8000
7000
6000
5000
4000
3000
2000
1000
0

Figure 4.5 σ values according to initial feasible design variables (left) optimum design variables (right) of Method 7.

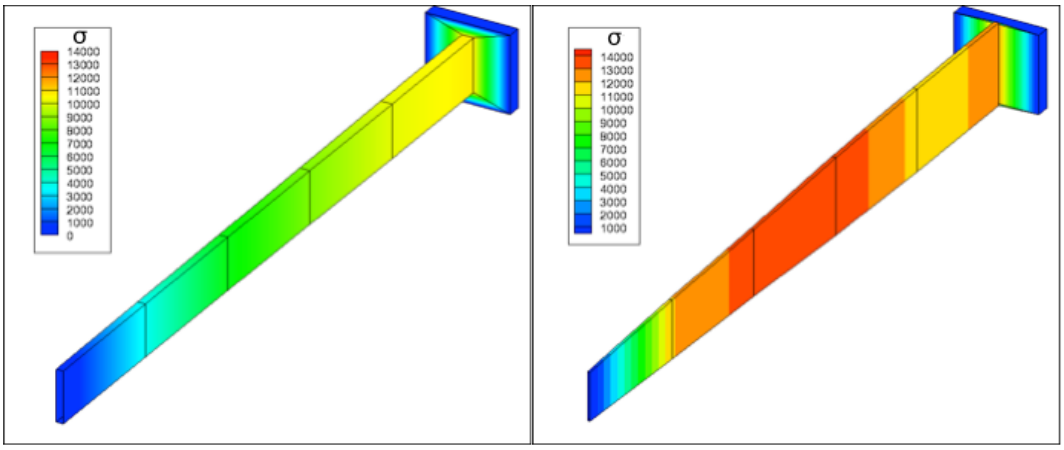
σ
14000
13000
12000
11000
10000
9000
8000
7000
6000
5000
4000
3000
2000
1000
0
σ
14000
13000
12000
11000
10000
9000
8000
7000
6000
5000
4000
3000
2000
1000

Figure 4.6 σ values according to initial feasible design variables (left) optimum design variables (right) of Method 8.

According to the results in Figure 4.5 and Figure 4.6, maximum allowed bending stress is observed at the mid section of the cantilevered beam. Figure 4.7 and Figure 4.8 show y_5 value for initial feasible and optimum design variables that are obtained via Method 7 and Method 8, respectively.

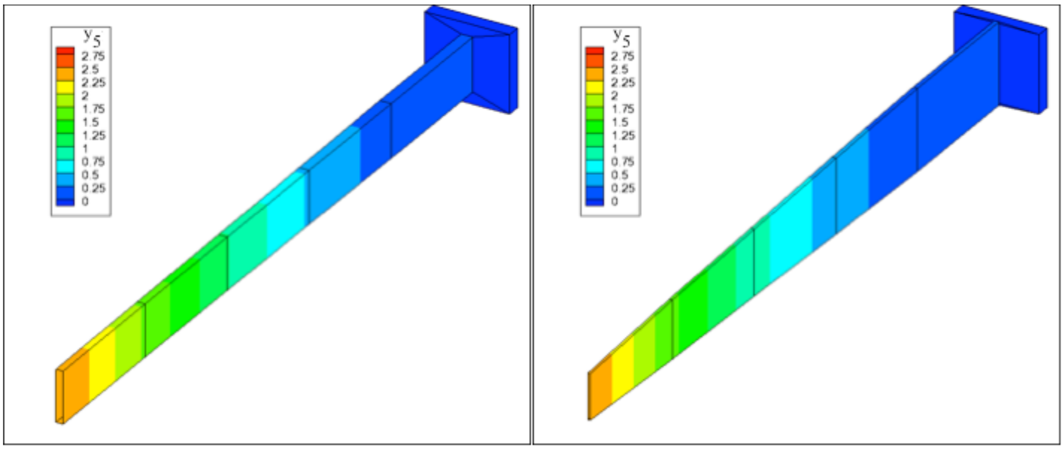
y5
2.75
2.5
2.25
2
1.75
1.5
1.25
1
0.75
0.5
0.25
0
y5
2.75
2.5
2.25
2
1.75
1.5
1.25
1
0.75
0.5
0.25
0

Figure 4.7 y_5 values according to initial feasible design variables (left) optimum design variables (right) of Method 7.

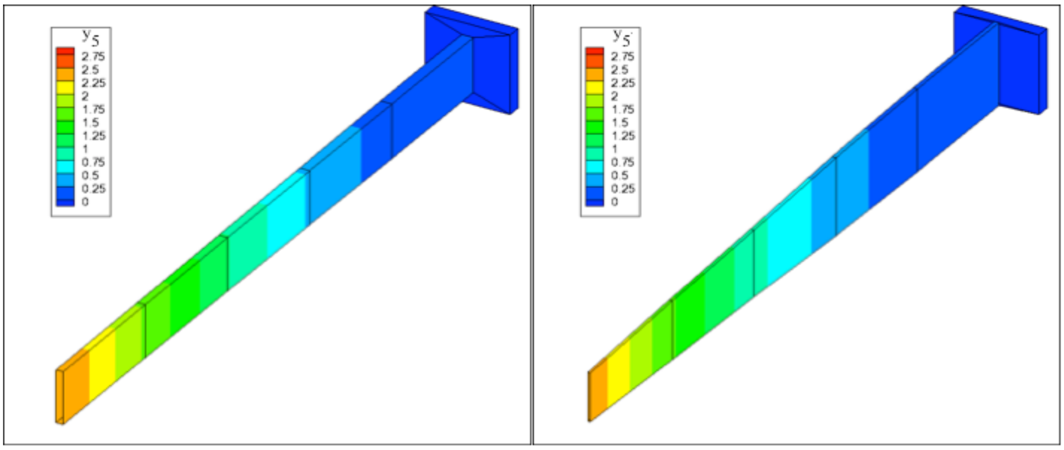
y5
2.75
2.5
2.25
2
1.75
1.5
1.25
1
0.75
0.5
0.25
0
y5
2.75
2.5
2.25
2
1.75
1.5
1.25
1
0.75
0.5
0.25
0

Figure 4.8 y_5 values according to initial feasible design variables (left) optimum design variables (right) of Method 8.

According to the results in Figure 4.7 and Figure 4.8, orange color shows that tip deflection constraint is not violated.

4.4 Conclusion

In this chapter, development of the generalized reduced gradient method is discussed. An optimization solver is developed by using the Fortran programming language, a structural optimization problem is solved and the results are compared with other commercial optimization solvers. The results of the developed solver are in agreement with the results of the commercial ones. But new modifications are required in order to decrease the iteration number that is required to find the optimum solution. As a result of this effort, an optimization solver is developed not only for aerodynamic problems but also for other engineering problems.

CHAPTER 5

MORPHING WING OPTIMIZATION

5.1 Introduction

In this part, fixed wing optimization is performed for airfoil shape change, planform change and the combination of them. This process is performed at 30 m/s at which the baseline wing has the least drag. After that it is assumed that morphing mechanisms are installed into the optimized wing and morphing optimization process starts. Morphing wing optimization is done for airfoil shape change, planform change and the combination of them at velocities 16 m/s, which is the stall velocity of baseline wing, 20 m/s, 40 m/s and 50 m/s.

5.2 Use of the Optimization Solver

Gradient based optimization solvers terminate under the following conditions [46]:

1. If Kuhn-Tucker conditions are satisfied;
   This is the best possible sign that optimum point has been found.
2. If fractional change of objective function is below than a certain value;
   It is not as good as first condition but it is defined as an optimum point.
3. Solver could not find a better point;
   Solver bounds should be checked. Another starting value can be used.
4. Feasible point is not found;
   Solver bounds should be checked. Another starting value can be used.

Before discussing the first condition, it should be stated that the developed optimization solver terminates if only and only if no appropriate step length value is found, which means that there is no better objective function value than the current one during step length search. Another important parameter is the definition of bounds. The bounds of optimization solver for the optimization problems in this chapter are defined as follows:

$$\left|g_j(X)\right| \leq 0\,.000001 \; j = 1,2,\dots\dots,m \tag{5.1}$$

$$\left|g_j(X)\right| \leq 0.001 \; j = m+1, m+2,\dots\dots,m+l \tag{5.2}$$

$$S = \begin{cases} 0 \text{ if } |Y_i - Y_i^u| \leq |Y_i^u * 0.0001| \text{ and } G_{r_i} < 0 \\ 0 \text{ if } \left|Y_i - Y_i^l\right| \leq |Y_i^u * 0.0001| \text{ and } G_{r_i} > 0 \\ \qquad -G_{r_i} \text{ otherwise} \end{cases} \tag{5.3}$$

When conditions in Equation 5.1 for inequality constraints and Equations 5.2 for equality constraints are satisfied, the solver regards the constraints to be satisfied. Equation 5.3 defines the search direction vector for design variables.

Kuhn-Tucker condition is the first order necessary condition for the objective function to be optimum. For constraint optimization problem, it is assumed to be satisfied if Lagrange multipliers, λ, are positive, which are found according to the formula in Equation 5.4 [41].

$$\begin{aligned} \lambda &= -(G^T G)^{-1} G^T F \quad && \text{for } m + l > 1 \\ \lambda &= -\frac{G^T F}{(G^T G)} && \text{for } m + l = 1 \end{aligned} \tag{5.4}$$

In Equation 5.4, G is Jacobian of the constraints with respect to the design variables, while F is the derivative array of the objective function with respect to the design variables. In Figure 5.1, variation of the Lagrange multiplier with the objective function for one equality constraint optimization problem, which is the fixed wing optimization that is performed only with planform design variables, is given.

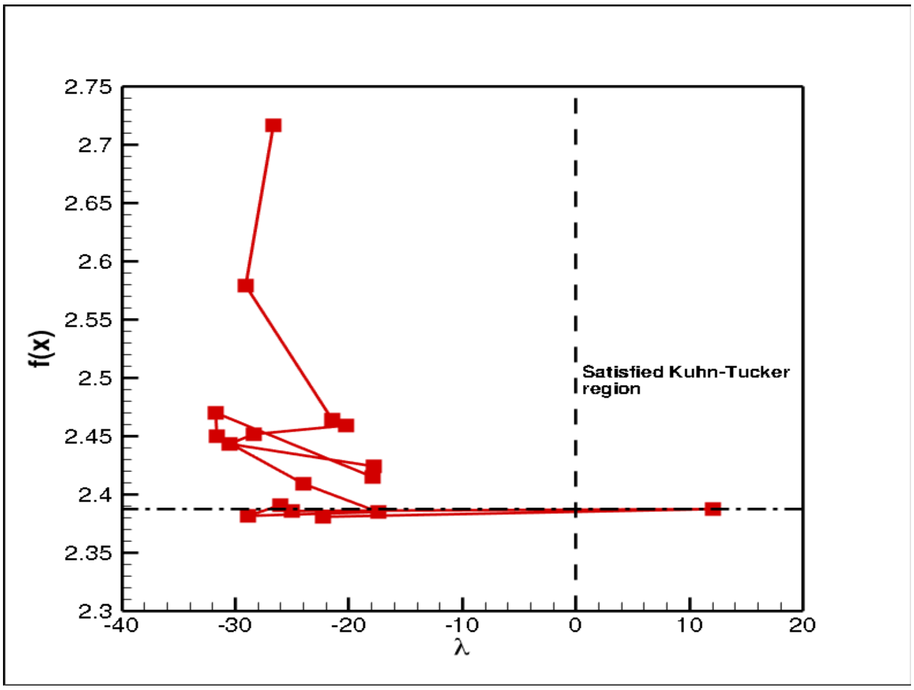

Figure 5.1 Variation of Lagrange multiplier with objective function value.

In Figure 5.1, red line shows the variation of the Lagrange multiplier with the objective function. Value at the right side of the dashed line is the optimum objective function according to Kuhn-Tucker condition. However, the developed optimization solver finds lower objective function values when Lagrange multiplier is less than zero according to the dashed dotted line. This situation can arise due to the selection of the bounds that are defined above and central difference parameter, h, which changes the sensitivity of the derivatives [41]. The central difference formula that is used in the optimization solver is shown in Equation 5.5.

$$f' = \frac{f\big(x(1+h)\big) - f\big(x(1-h)\big)}{2h} + O(h^2) \tag{5.5}$$

h value in the above equation is chosen as 0.01. New starting point is obtained with the multiplication of all design variables with 0.98 or 1.02 according to the values of F array and sending them to back to feasible algorithm in the solver. The solver is allowed to stop 10 times due to no appropriate step length value. For morphing wing optimization that is obtained with airfoil shape and planform change, this value is 30. But it does not necessarily mean that the solver finds a better optimum result at each new starting point.

5.3 Baseline Wing

In this study, the morphing mechanism, design and analysis methods are similar to those outlined in the study of Gamboa et al. [19]. In this thesis, induced drag and pressure drag are obtained by the 3-D panel method. Half span is divided into 8 spanwise strips, while the chord is divided into 150 panels. As a result, 3-D panel method solves the inverse of a 1275x1275 matrix to obtain a solution including side panels. 2DBLS calculates skin friction drag at each strip along half span. Airfoil shape is generated by using the b-spline method, which uses first 6 points for thickness generation at 0.95c, 0.8c, 0.5c, 0.2c, 0.05c and 0, and uses remaining 5 points for camber generation at 0.95c, 0.8c, 0.5c, 0.2c and 0.05c. The sixth control point of the thickness distribution is used for defining leading edge diameter. Weight of UAV is taken as 106.01 N, which is the weight that is calculated after fixed wing optimization process in the study of Gamboa et al. [19].

In Figure 5.2, baseline wing airfoil is shown with thickness control points (tcp) and camber control points (ccp).

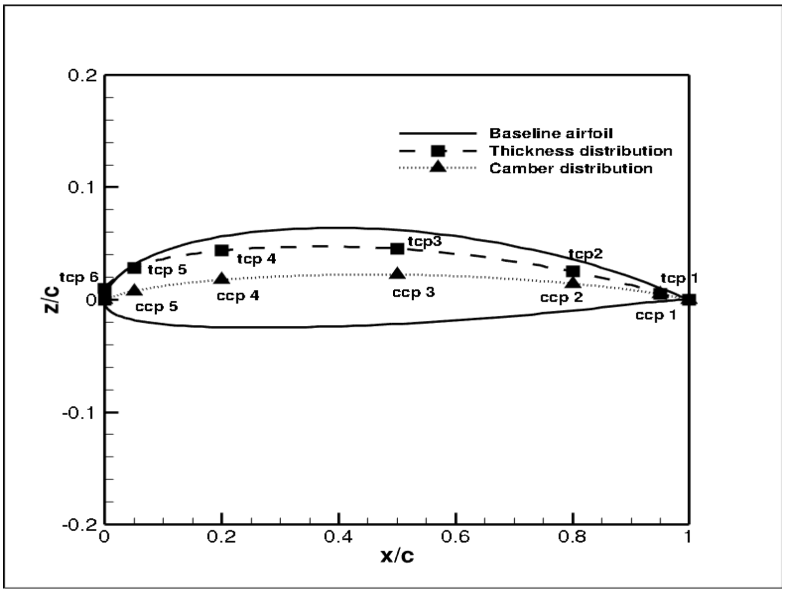

Figure 5.2 Baseline wing airfoil.

Baseline wing is a rectangular wing that has 1.2 m half span and 0.2 m chord, which is shown in Figure 5.3.

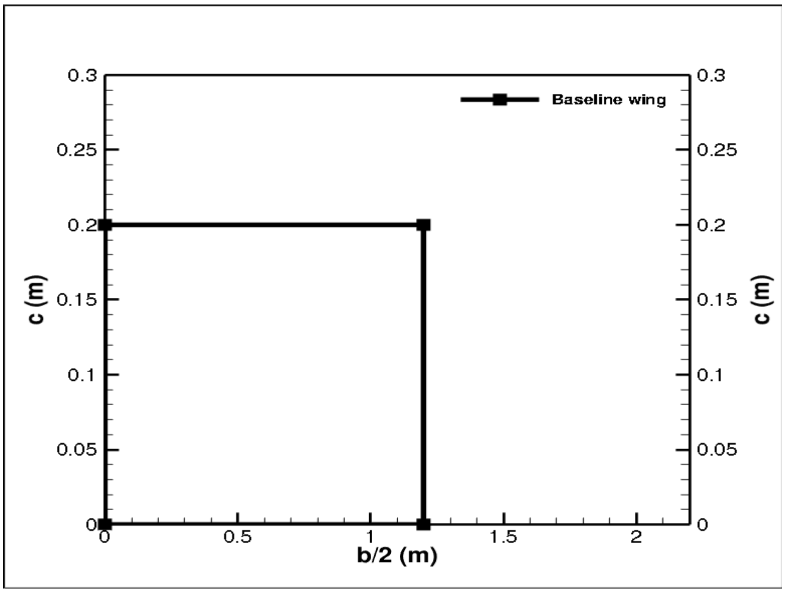

Figure 5.3 Baseline wing, top view.

Figure 5.4 shows drag vs. velocity curve for the baseline wing at steady level flight at different velocities.

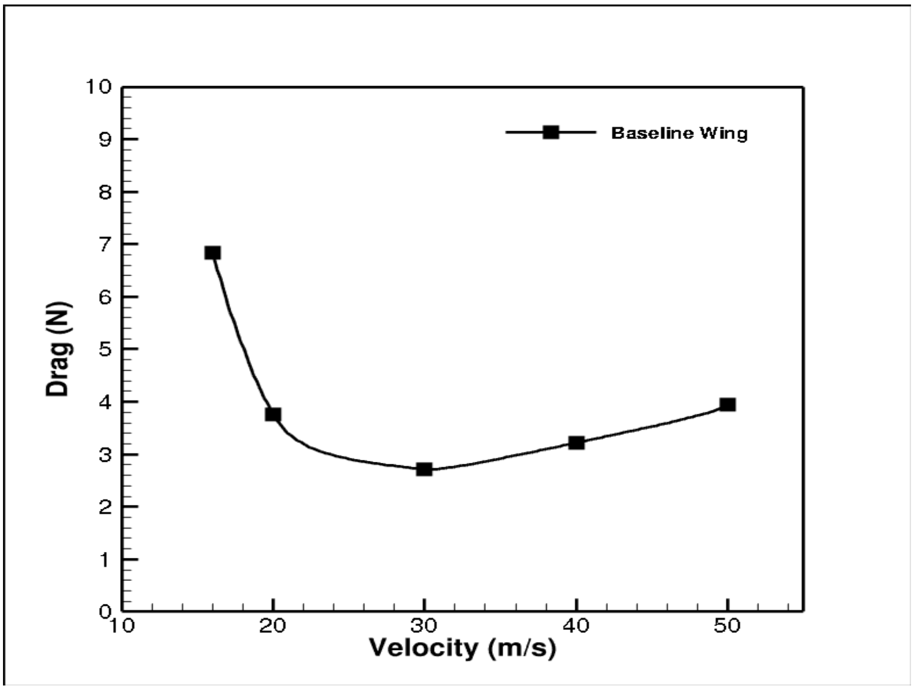

Figure 5.4 Drag vs. velocity for baseline wing.

According to the drag results that are shown in Figure 5.4, minimum drag is obtained at 30 m/s. This is the velocity at which fixed wing optimization process is performed since it is assumed that the UAV flies its design mission at this velocity. Table 5.1 shows velocity, lift, corrected lift, induced and pressure drag, total drag and required angle of attack values in steady level flight for the baseline wing.

Table 5.1 Steady level flight data for baseline wing.

Velocity (m/s)	Lift (N)	Corrected Lift (N)	Induced Drag + Pressure Drag (N)	Total Drag (N)	α (deg)
16	124.684	106.010	4.882	6.846	14.988
20	106.729	106.010	2.496	3.758	7.440
30	106.013	106.010	1.155	2.718	1.591
40	106.011	106.010	0.723	3.219	-0.253
50	106.011	106.010	0.510	3.941	-1.106

According to the results in Table 5.1, it is seen that when the angle of attack value is 14.988 degree, the UAV can fly at 16 m/s. This velocity is accepted as the stall velocity of the UAV since no converged solution could be obtained below this velocity. Calculation of drag vs. velocity values is not performed below this velocity in fixed wing and morphing wing optimization.

Before going into details of optimization problems, it is important to discuss about the drag at steady level flight. Equation 5.6 shows the drag formula for steady level flight.

$$D = \frac{1}{2}\rho V_\infty^2 S C_{D0} + \frac{2KW^2}{\rho V_\infty^2 S} \tag{5.6}$$

In Equation 5.6, first term corresponds to the parasite drag, whereas the second one depicts induced drag. Parasite drag, which is the main source of drag at high speeds, decreases when wing area and parasite drag coefficient decrease. Induced drag, which is the main source of drag at low speeds, decreases as wing area increases and K value decreases. K value is a function of aspect ratio and taper ratio and it decreases as aspect ratio increases and taper ratio decreases. The optimization solver is responsible for finding the optimum airfoil shape and planform in order to minimize the total drag.

5.4 Fixed Wing Optimization

Fixed Wing optimization consists of three parts. In the first part, planform design variables do not change, only airfoil is optimized for minimum drag. In the second part, airfoil design variables are constant, planform design variables are optimized for minimum drag. In the last part of this section, both airfoil and planform design variables are changed for the optimization problem.

5.4.1 Fixed Wing Optimization with Only Airfoil Shape Change

For this part, fixed wing optimization problem is defined as follows:

$$\text{Minimize } \mathrm{D} = \mathrm{D_i} + \mathrm{D_p} + \mathrm{D_f} \text{ @ } \mathrm{V_\infty} = 30\ \mathrm{m/s} \tag{5.7}$$

subject to

$$\mathrm{L} = \mathrm{W} = 106.01\ \mathrm{N} \tag{5.8}$$

$$-5^{\mathrm{o}} \leq \alpha \leq 15^{\mathrm{o}} \tag{5.9}$$

$$\mathrm{z_1/c} \geq 0.001 \tag{5.10}$$

$$\mathrm{z_6/c} \geq 0.01 \tag{5.11}$$

$$\mathrm{z_i/c} \geq 0\ \mathrm{i} = 2-5, 7-11 \tag{5.12}$$

$$\mathrm{z_i/c} \leq 0.1\ \mathrm{i} = 1-11 \tag{5.13}$$

Equations between 5.7-5.13 define the optimization problem with one equality constraint. 1st and 6th control points are the control points that create the trailing edge thickness and leading edge diameter, respectively. Therefore, they have a minimum value different than 0. The other control points can have 0 at defined chord locations. The control points can have a value of 0.1 as maximum. Figure 5.5 shows baseline wing airfoil and optimum airfoil, which is obtained with airfoil shape change only.

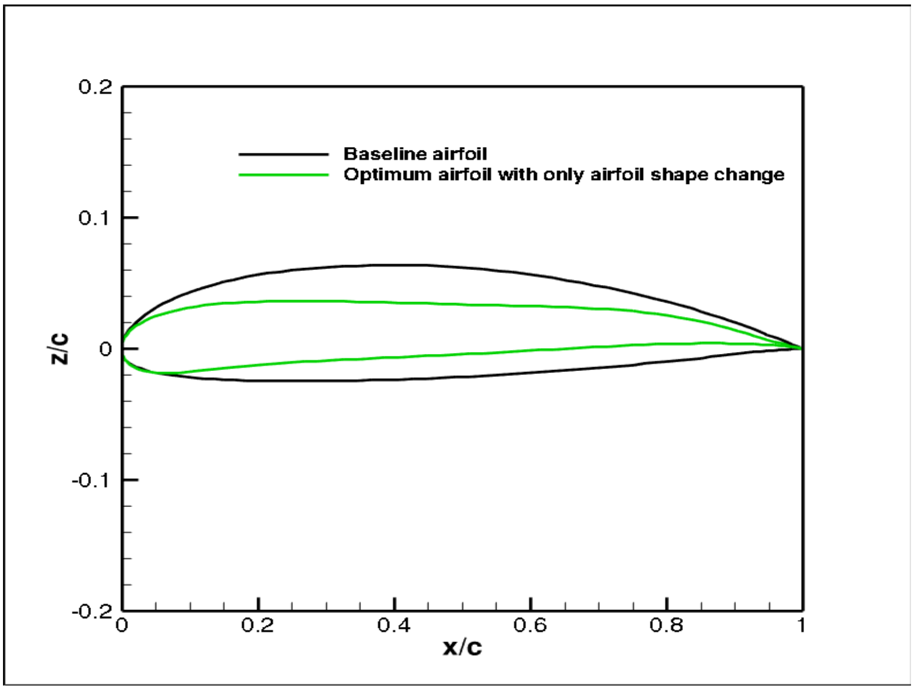

Figure 5.5 Baseline airfoil and optimum airfoil that is obtained with only airfoil shape change.

As it is seen in Figure 5.5, optimum airfoil has a lower physical thickness than baseline wing airfoil. In addition to this, leading edge diameter decreases and it has a sharper trailing edge. Figure 5.6 shows drag vs. velocity for the optimum wing for this optimization problem.

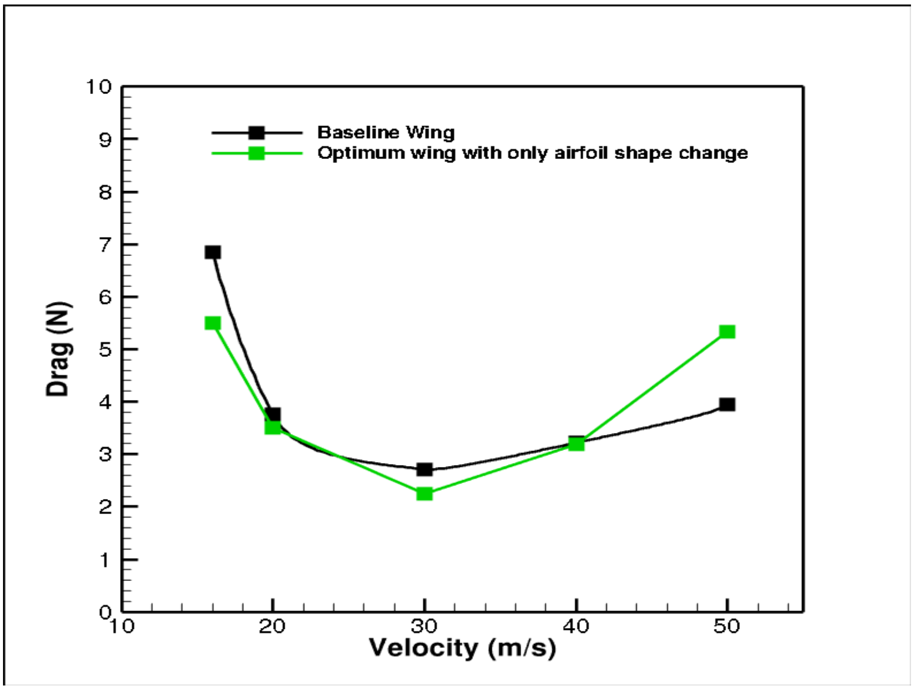

Figure 5.6 Drag vs. velocity for baseline wing and optimum wing that is obtained with only airfoil shape change.

According to the results in Figure 5.6, optimum wing has less drag than the baseline wing apart from 50 m/s. Table 5.2 depicts velocity, lift, corrected lift, induced and pressure drag, total drag and required angle of attack values in steady level flight for optimum wing in this section.

Table 5.2 Steady level flight data for optimum wing that is obtained with only airfoil shape change.

Velocity (m/s)	Lift (N)	Corrected Lift (N)	Induced Drag + Pressure Drag (N)	Total Drag (N)	α (deg)
16	129.666	106.010	4.091	5.508	12.210
20	106.016	106.010	2.315	3.505	7.238
30	106.011	106.010	1.165	2.253	1.821
40	106.011	106.010	0.769	3.197	-0.063
50	106.011	106.010	0.591	5.338	-0.934

Higher skin friction drag results at 50 m/s is observed when Table 5.1 and Table 5.2 are compared. It is due to early transition from to laminar to turbulent region at the lower surfaces of the wing strips for the optimum wing.

5.4.2 Fixed Wing Optimization with Only Planform Change

For this optimization, following optimization problem is defined.

$$\text{Minimize } \mathrm{D} = \mathrm{D_i} + \mathrm{D_p} + \mathrm{D_f} \text{ @ } \mathrm{V_\infty} = 30\ \mathrm{m/s} \tag{5.14}$$

subject to

$$\mathrm{L} = \mathrm{W} = 106.01\ \mathrm{N} \tag{5.15}$$

$$-5^{o} \leq \alpha \leq 15^{o} \tag{5.16}$$

$$0.15\ \mathrm{m} \leq \mathrm{c_r}, \mathrm{c_t} \leq 0.33\ \mathrm{m} \tag{5.17}$$

$$1\ \mathrm{m} \leq \mathrm{b}/2 \leq 1.7\ \mathrm{m} \tag{5.18}$$

According to the optimization problem, tip and root chord varies between 0.15 m and 0.33 m, whereas total span is allowed to vary between 2 m and 3.4 m. Optimum wing that is obtained with only planform change can be seen in Figure 5.7.

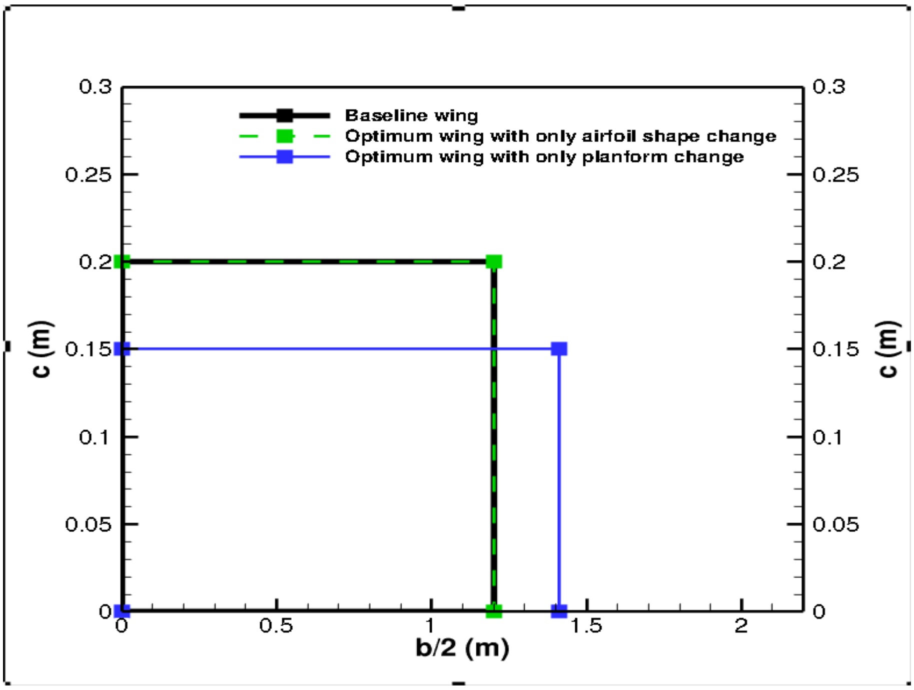

Figure 5.7 Baseline wing and optimum wing that is obtained with only planform change, top view.

According to the results in Figure 5.7, optimization solver finds another rectangular wing whose chord length decreases to 0.15 and half span increases to 1.411 m. As a result of this, wing area decreases from 0.48 m^2 to 0.423 m^2 and aspect ratio increases from 12 to 18.815. Figure 5.8 shows drag vs. velocity for the optimum wing.

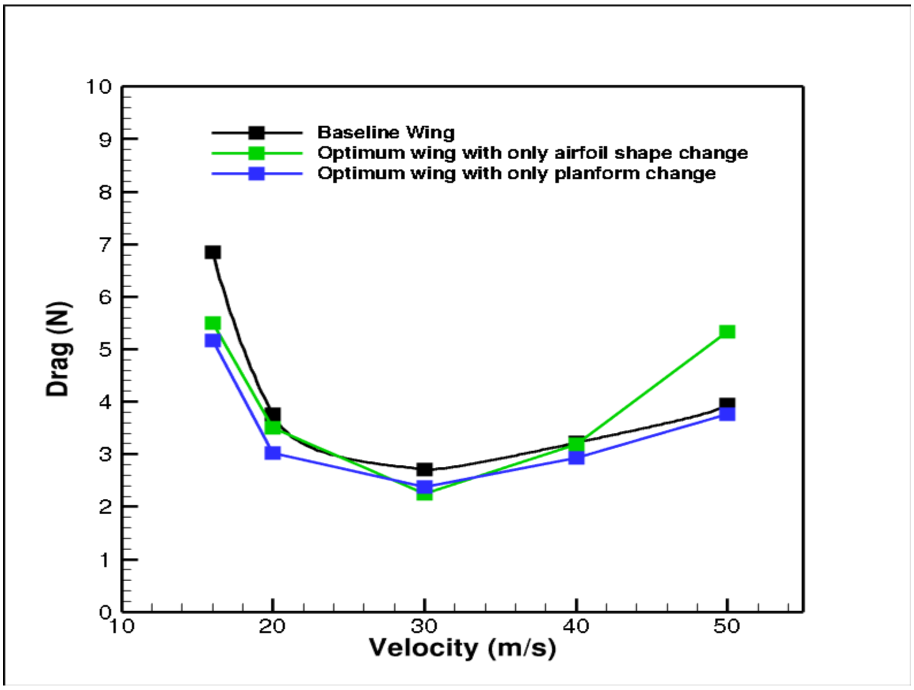

Figure 5.8 Drag vs. velocity for baseline wing and optimum wings that are obtained with only airfoil shape change and only planform change.

According to the results in Figure 5.8, optimum wing that is obtained with only planform change has higher drag than the optimum wing that is obtained with only airfoil shape change at 30 m/s. However, at higher velocities, it has less drag due to decrease in wing area. In addition to this, it has less drag at lower velocities although it has smaller wing area. At lower velocities, higher angle of attack values are required in order to maintain steady level flight, induced drag becomes the main source of drag. However, optimum wing that is obtained with only planform change has higher aspect ratio with respect to baseline wing and optimum wing that is obtained with only airfoil shape change. It is well known that higher aspect ratio means lower induced drag. As a result of this, optimum airfoil in this part has lower drag at lower velocities. Table 5.3 tabulates steady level flight data for the optimum wing in this section.

Table 5.3 Steady level flight data for optimum wing that is obtained with only planform change.

Velocity (m/s)	Lift (N)	Corrected Lift (N)	Induced Drag + Pressure Drag (N)	Total Drag (N)	α (deg)
16	134.000	106.010	3.430	5.171	14.838
20	106.977	106.010	1.708	3.032	7.508
30	106.016	106.010	0.853	2.381	1.842
40	106.011	106.010	0.550	2.925	-0.105
50	106.011	106.010	0.396	3.758	-1.004

5.4.3 Fixed Wing Optimization with Airfoil Shape and Planform Change

This optimization problem is mathematically defined as follows:

$$\text{Minimize } \mathrm{D} = \mathrm{D_i} + \mathrm{D_p} + \mathrm{D_f} \ @\ \mathrm{V_\infty} = 30\ \mathrm{m/s} \tag{5.19}$$

subject to

$$\mathrm{L} = \mathrm{W} = 106.01\ \mathrm{N} \tag{5.20}$$

$$-5^{\circ} \leq \alpha \leq 15^{\circ} \tag{5.21}$$

$$\mathrm{z_1/c} \geq 0.001 \tag{5.22}$$

$$\mathrm{z_6/c} \geq 0.01 \tag{5.23}$$

$$\mathrm{z_i/c} \geq 0 \ \mathrm{i} = 2-5, 7-11 \tag{5.24}$$

$$\mathrm{z_i/c} \leq 0.1 \ \mathrm{i} = 1-11 \tag{5.25}$$

$$0.15\mathrm{m} \leq \mathrm{c_r}, \mathrm{c_t} \leq 0.33\ \mathrm{m} \tag{5.26}$$

$$1\mathrm{m} \leq \mathrm{b}/2 \leq 1.7\mathrm{m} \tag{5.27}$$

The optimization problem that is defined by Equations between 5.19 and 5.27 is the summation of optimization problems that are defined in Sections 5.3.1 and 5.3.2. Optimum wing planform can be seen in Figure 5.9.

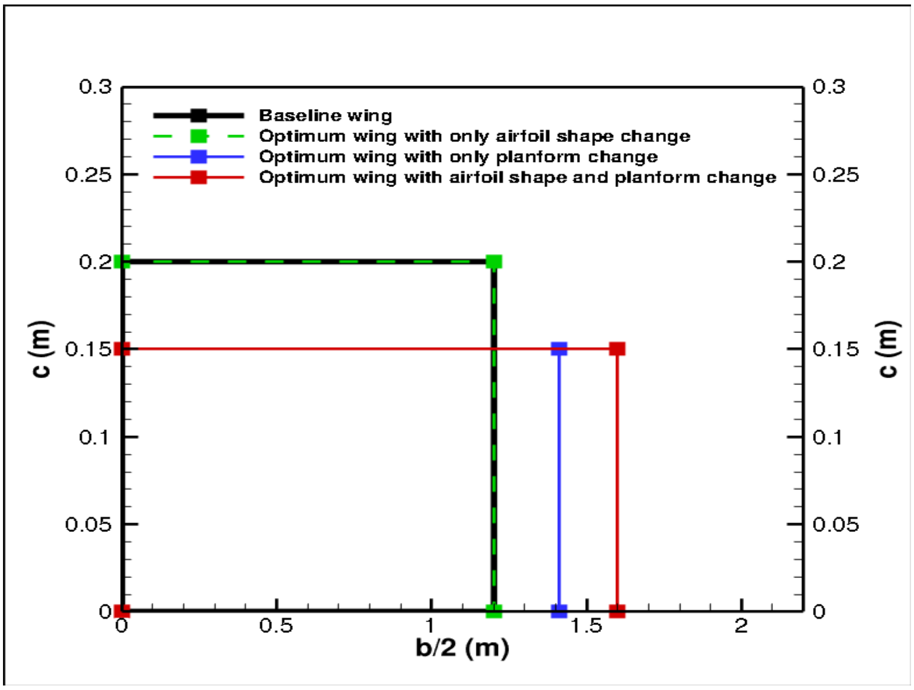

Figure 5.9 Baseline wing and optimum wings that are obtained with only airfoil shape change, only planform change and airfoil shape and planform change, top view.

The results in Figure 5.9 reveal that optimum wing that is obtained with airfoil shape and planform change has longer half span, which increases from 1.2 m to 1.6 m. It is a rectangular wing whose chord value decreases from 0.2 m to 0.15. As a result of these changes, aspect ratio increases from 12 to 21.334. However, wing area remains constant as 0.48 m^2. Optimum airfoil can be seen in Figure 5.10.

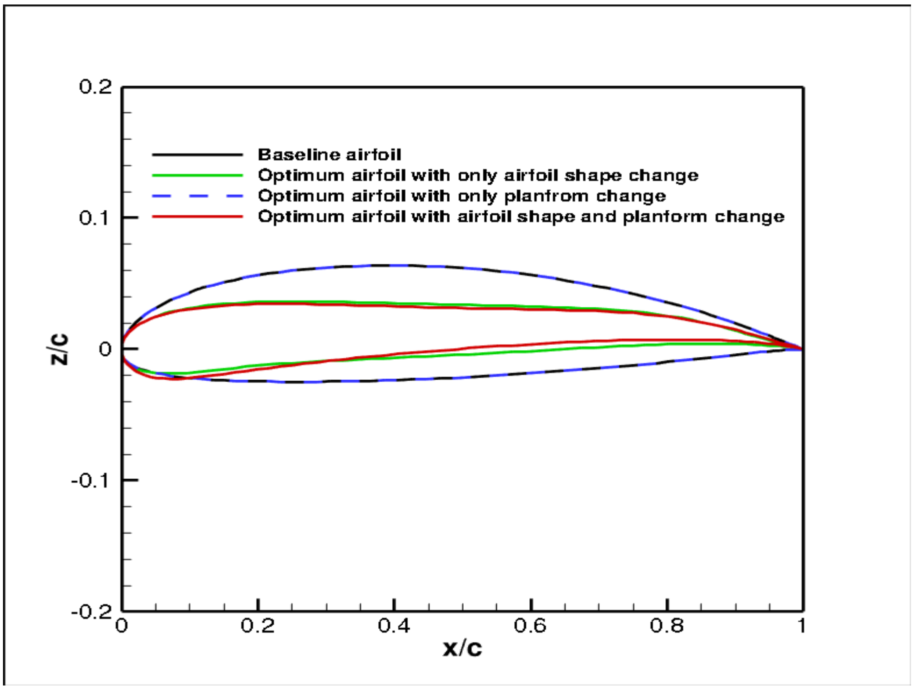

Figure 5.10 Baseline airfoil and optimum airfoils that are obtained with only airfoil shape change, only planform change and airfoil shape and planform change.

In Figure 5.10, it is seen that optimum airfoil that is obtained by the optimization problem in this section has higher physical thickness around the leading edge region and has sharper trailing edge when it is compared with the optimum airfoil that is obtained with only airfoil shape change. Figure 5.11 shows drag vs. velocity curve for the optimum wing.

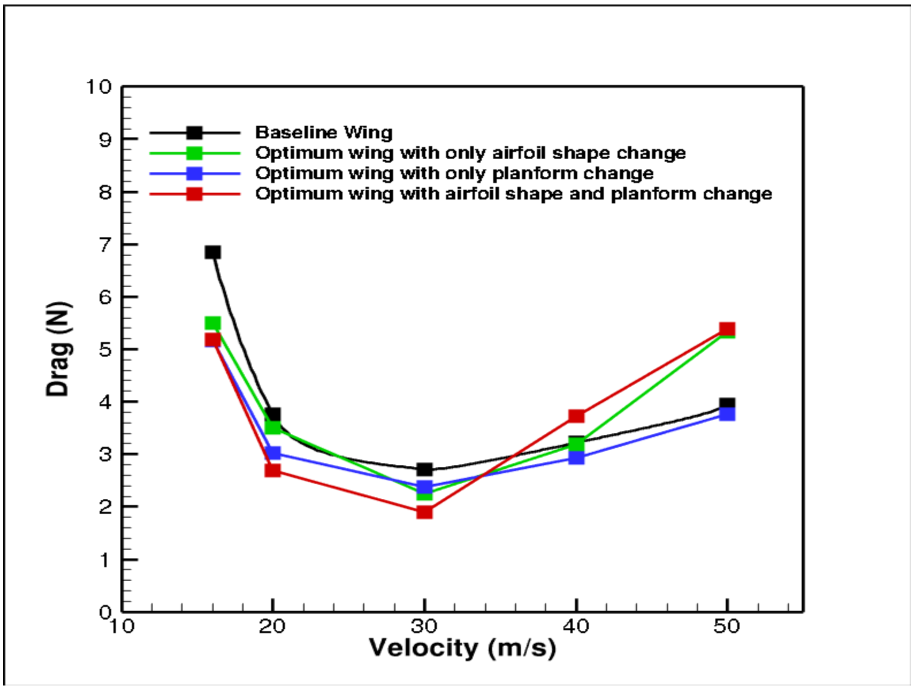

Figure 5.11 Drag vs. velocity for baseline wing and optimum wings that are obtained with only airfoil shape change, only planform change and airfoil shape and planform change.

Results in Figure 5.11 state that smallest wing drag is obtained at 30 m/s when the wing is optimized with airfoil shape and planform change as it is expected. When the results related with wing optimization with only airfoil shape change are discussed it is mentioned that higher drag results are seen at higher velocities. This situation is also valid for optimum wing in this section according to Figure 5.11. When the velocity is greater than 36 m/s drag values of the baseline wing is less than the optimum wing that is obtained with airfoil shape and planform change. The main reason for this is the early transition as it is mentioned in the previous comment. Table 5.4 tabulates steady level flight data for optimum wing. Compared to the wing optimized with only planform change, the wing that is optimized with airfoil shape and planform is bigger, which helps to decrease the induced drag. Although the skin friction drag is first thought to increase due to a larger wing; comparing the results in Table 5.3 and Table 5.4 at suggest that skin friction drag is also reduced because of lower angle of attack and less chamber that delay transition.

Table 5.4 Steady level flight data for optimum wing that is obtained with airfoil shape and planform change.

Velocity (m/s)	Lift (N)	Corrected Lift (N)	Induced Drag + Pressure Drag (N)	Total Drag (N)	α (deg)
16	132.320	106.010	2.930	5.191	14.785
20	106.012	106.010	1.311	2.691	6.142
30	106.011	106.010	0.705	1.897	1.169
40	106.011	106.010	0.494	3.734	-0.563
50	106.011	106.010	0.399	5.394	-1.365

It should be repeated that the baseline wing is optimized for 30 m/s by optimization the airfoil shape, planform and both in this section. When velocity is not equal to 30 m/s, it is an off-design condition for all three optimized wing. Morphing is a way to improve the aerodynamic performance of the optimized wing in off-design conditions, as explained in the next section.

5.5 Morphing Wing Optimization

In the same manner as in fixed wing optimization, this part consists of three subparts. In the first part, only airfoil design variables are used in the optimization problem at defined shape change allowances along the chord, which are defined as inequality constraints in optimization problem. In second part airfoil shape does not vary and planform design variables are responsible for morphing. The optimization problem in third part is a combination of optimization problems in the first and second parts.

5.5.1 Morphing Wing Optimization with Only Airfoil Shape Change

In this optimization process, a parametric study is performed in order to investigate the effect of shape change allowance on the aerodynamic results. Airfoil shape change is allowed according to the physical thicknesses of the upper and lower surfaces with respect to chord at certain chordwise locations, which are 0.9c, 0.75c, 0.5c 0.25c and 0.1c. It is assumed that the physical thickness can vary in certain percentages with respect to its original physical thickness. During the parametric study, these percentages are chosen as 5%, 10% and 15%. The optimization problem for 5% allowance is described below, as an example.

$$\begin{aligned}&\text{Minimize } \mathrm{D} = \mathrm{D_i} + \mathrm{D_p} + \mathrm{D_f}\\ &@\ \mathrm{V}_\infty = 16\,\mathrm{m/s}\,, 20\,\mathrm{m/s}\,, 40\,\mathrm{m/s} \text{ and } 50\ \mathrm{m/s}\end{aligned} \tag{5.28}$$

subject to

$$\mathrm{L} = \mathrm{W} = 106.01\ \mathrm{N} \tag{5.29}$$

$$-5^{\mathrm{o}} \leq \alpha \leq 15^{\mathrm{o}} \tag{5.30}$$

$$\mathrm{z_1/c} \geq 0.001 \tag{5.31}$$

$$\mathrm{z_6/c} \geq 0.01 \tag{5.32}$$

$$\mathrm{z_i/c} \geq 0\ \mathrm{i} = 2 - 5, 7 - 11 \tag{5.33}$$

$$\mathrm{z_i/c} \leq 0.1\ \mathrm{i} = 1 - 11 \tag{5.34}$$

$$\begin{aligned}&0.95 * \left(\frac{\mathrm{z}}{\mathrm{c}}\right)_{\mathrm{upinitial}_{\frac{\mathrm{x}}{\mathrm{c}}}} \leq \left|\left(\frac{\mathrm{z}}{\mathrm{c}}\right)_{\mathrm{up}_{\frac{\mathrm{x}}{\mathrm{c}}=\mathrm{i}}}\right| \leq 1.05 * \left(\frac{\mathrm{z}}{\mathrm{c}}\right)_{\mathrm{upinitial}_{\frac{\mathrm{x}}{\mathrm{c}}}}\\ &\text{for } \frac{\mathrm{x}}{\mathrm{c}} = 0.9, 0.75, 0.5, 0.25 \text{ and } 0.1\end{aligned} \tag{5.35}$$

$$\begin{aligned}&1.05 * \left(\frac{\mathrm{z}}{\mathrm{c}}\right)_{\mathrm{lowinitial}_{\frac{\mathrm{x}}{\mathrm{c}}}} \leq \left|\left(\frac{\mathrm{z}}{\mathrm{c}}\right)_{\mathrm{low}_{\frac{\mathrm{x}}{\mathrm{c}}=\mathrm{i}}}\right| \leq 0.95 * \left(\frac{\mathrm{z}}{\mathrm{c}}\right)_{\mathrm{lowinitial}_{\frac{\mathrm{x}}{\mathrm{c}}}}\\ &\text{for } \frac{\mathrm{x}}{\mathrm{c}} = 0.9, 0.75, 0.5, 0.25 \text{ and } 0.1\end{aligned} \tag{5.36}$$

Equation 5.35 and Equation 5.36 describe the physical thickness allowance for upper and lower region of the airfoil and they create 20 inequality constraints. There is one equality constraint. The optimum airfoil shapes without physical thickness constraints are also given with orange dashed line in the figures below. The initial wing of the morphing wing optimization in this part is the optimum wing that is obtained by fixed wing optimization with airfoil shape and planform change in Section 5.4.3.

Morphing airfoils at different physical allowance changes are given for 16 m/s in Figure 5.12. Vertical lines depict the allowance limit at difference percentages.

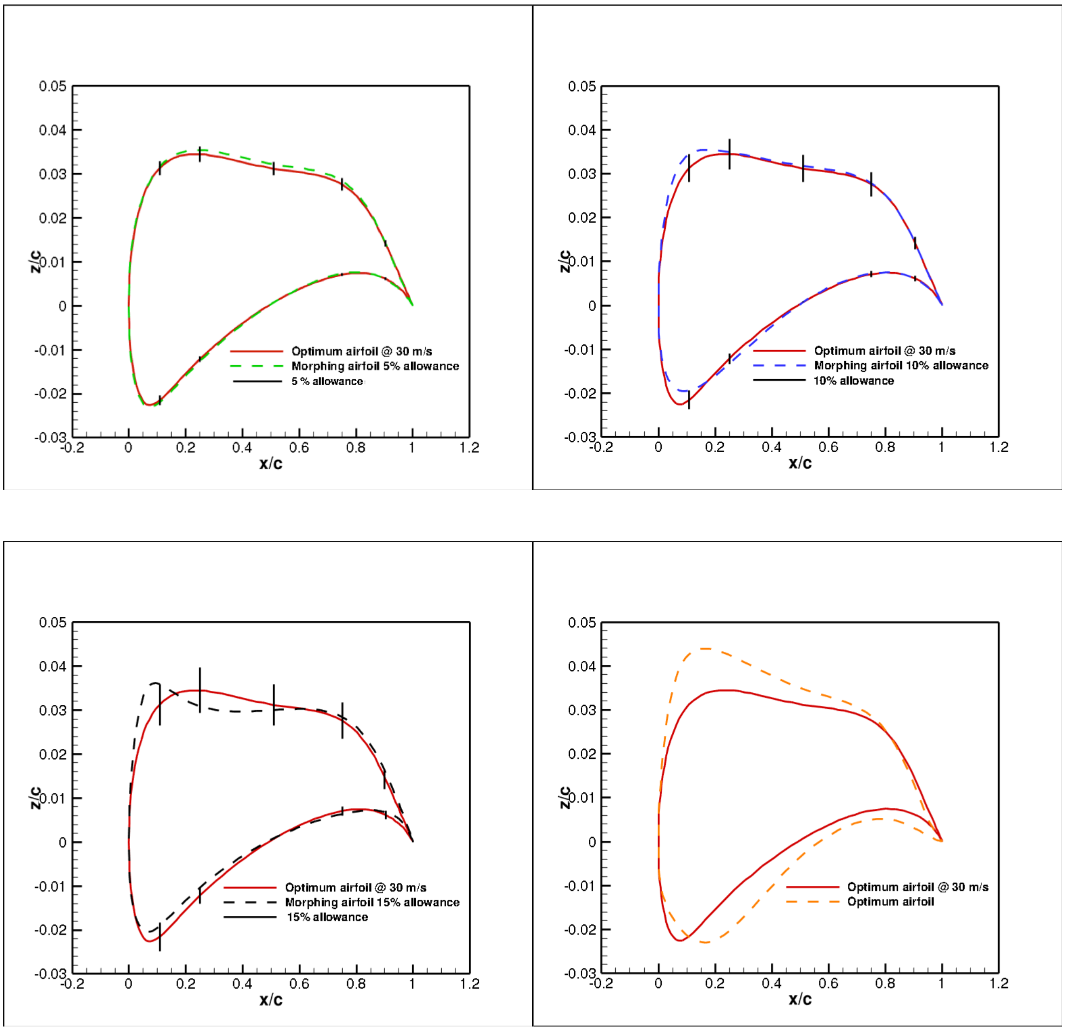

Figure 5.12 Morphing airfoil shapes at % 5 allowance (top left), % 10 allowance (top right), % 15 allowance (bottom left), without physical constraint (bottom right) at 16 m/s.

According to the results in Figure 5.12, it is seen that the morphing airfoil has increased leading edge diameter as allowances increase. The airfoil shapes do not follow a pattern as allowance increase because separation occurs very early at 16 m/s and correction formulas for drag that are discussed in Chapter 3 increase nonlinearity in the optimization problem. When there is no physical limit, trailing edge region of the airfoil shape is different. Airfoil shapes in Figure 5.12 can be seen together in Figure 5.13.

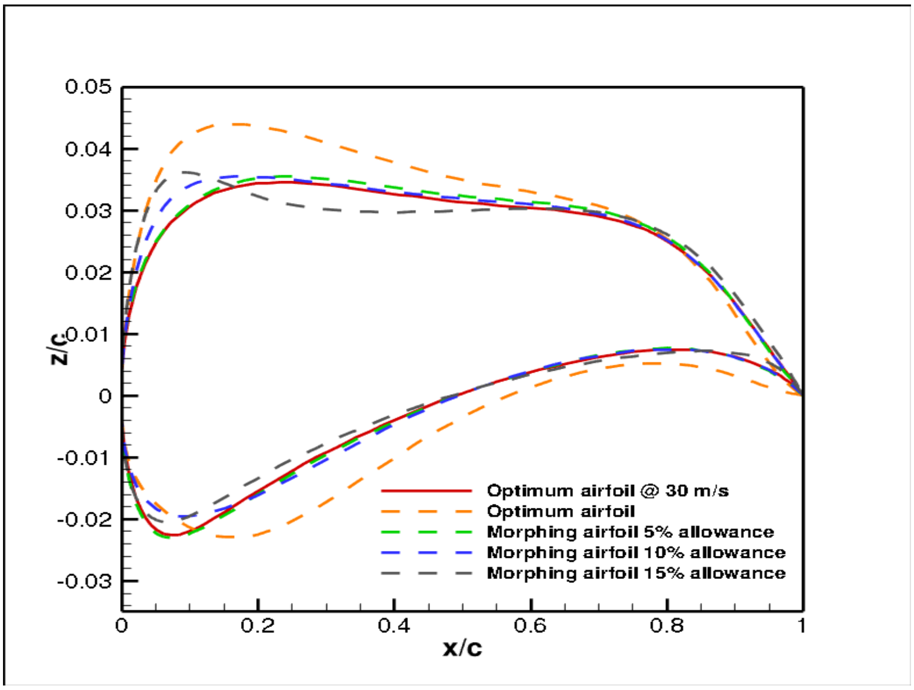

Figure 5.13 Morphing airfoil shapes at different allowances at 16 m/s.

Table 5.5 shows steady level flight data at different airfoil shape change allowance. 0% allowance describe optimum airfoil that is obtained in Section 5.4.3 and 100% allowance describe the optimum airfoil shapes without physical thickness constraints.

Table 5.5 Steady level flight data for morphing wing that is obtained with only airfoil shape change at 16 m/s.

Change Allowance (%)	Lift (N)	Corrected Lift (N)	Induced Drag + Pressure Drag (N)	Total Drag (N)	α (deg)
0	132.320	106.010	2.930	5.191	14.785
5	130.710	106.010	2.942	4.979	14.581
10	131.796	106.010	2.940	4.811	14.666
15	130.093	106.010	3.063	4.509	14.073
100	130.016	106.010	2.904	4.470	14.975

According to the results in Table 5.5, lift and corrected lift values are close to each other for all change allowance values. This is due to early separation as it is mentioned above. 15% change allowance drag result is very close to 100% change allowance.

Figure 5.14 shows the morphing airfoil at different shape change allowances for 20 m/s.

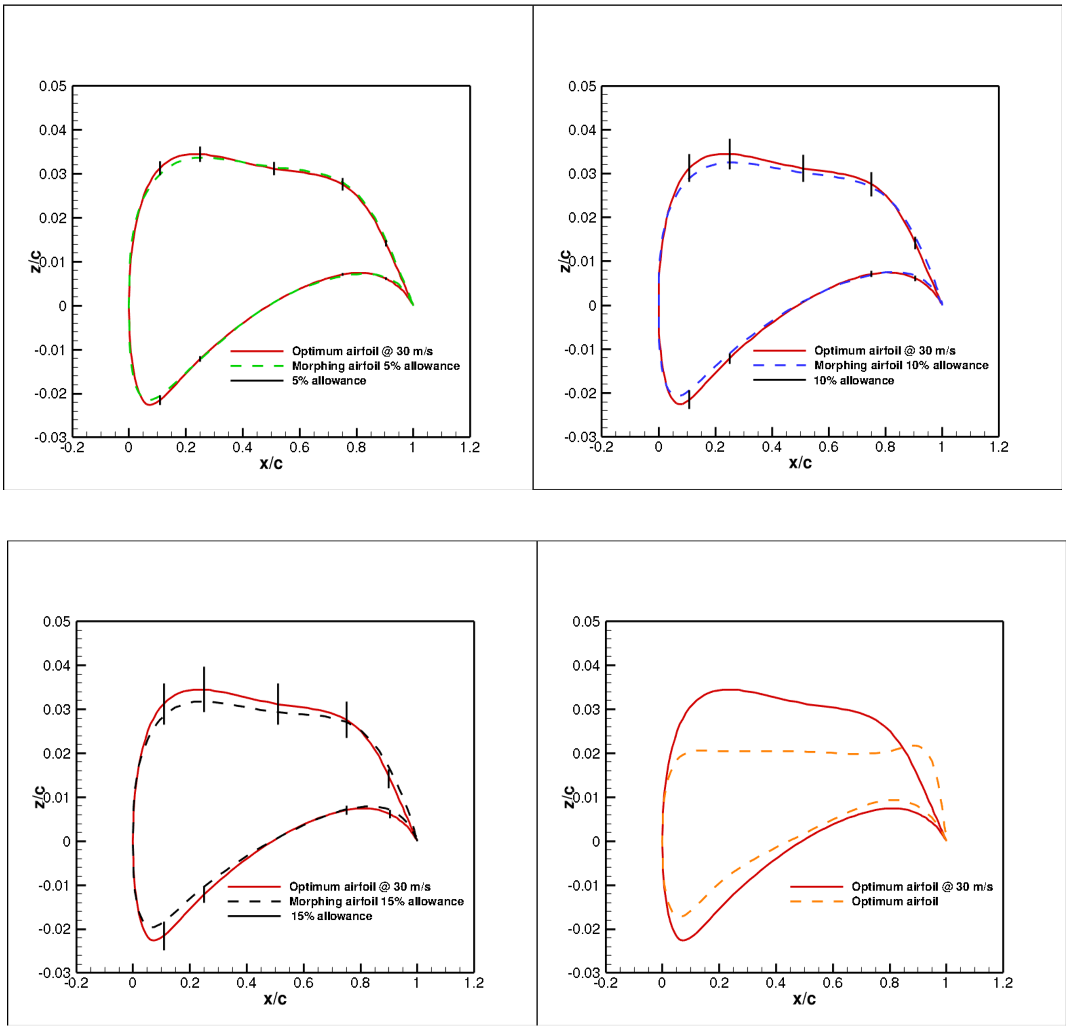

Figure 5.14 Morphing airfoil shapes at % 5 allowance (top left), % 10 allowance (top right), % 15 allowance (bottom left), without physical constraint (bottom right) at 20 m/s.

According to the results in Figure 5.14, it is observed that airfoil tries to decrease the physical thickness that is around 0.1c as allowance increases. When there is no physical limit, trailing edge region of the airfoil shape is different. The morphing airfoil shapes can be seen together in Figure 5.15.

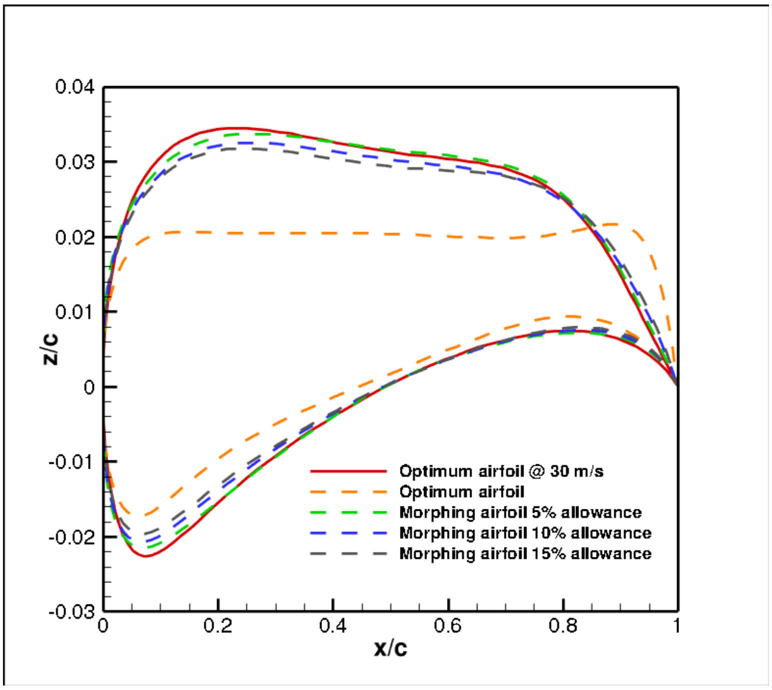

Figure 5.15 Morphing airfoil shapes at different allowances at 20 m/s.

Table 5.6 tabulates steady level flight data at different shape change allowances at 20 m/s.

Table 5.6 Steady level flight data for morphing wing that is obtained with only airfoil shape change at 20 m/s.

Change Allowance (%)	Lift (N)	Corrected Lift (N)	Induced Drag + Pressure Drag (N)	Total Drag (N)	α (deg)
0	106.012	106.010	1.311	2.691	6.142
5	106.016	106.010	1.413	2.515	5.970
10	106.015	106.010	1.396	2.507	5.824
15	106.011	106.010	1.373	2.491	5.711
100	106.010	106.010	1.313	2.432	4.737

All shape change allowance drag results are very close to each other when results in Table 5.6 are investigated.

Figure 5.16 shows morphing airfoil shapes for 40 m/s.

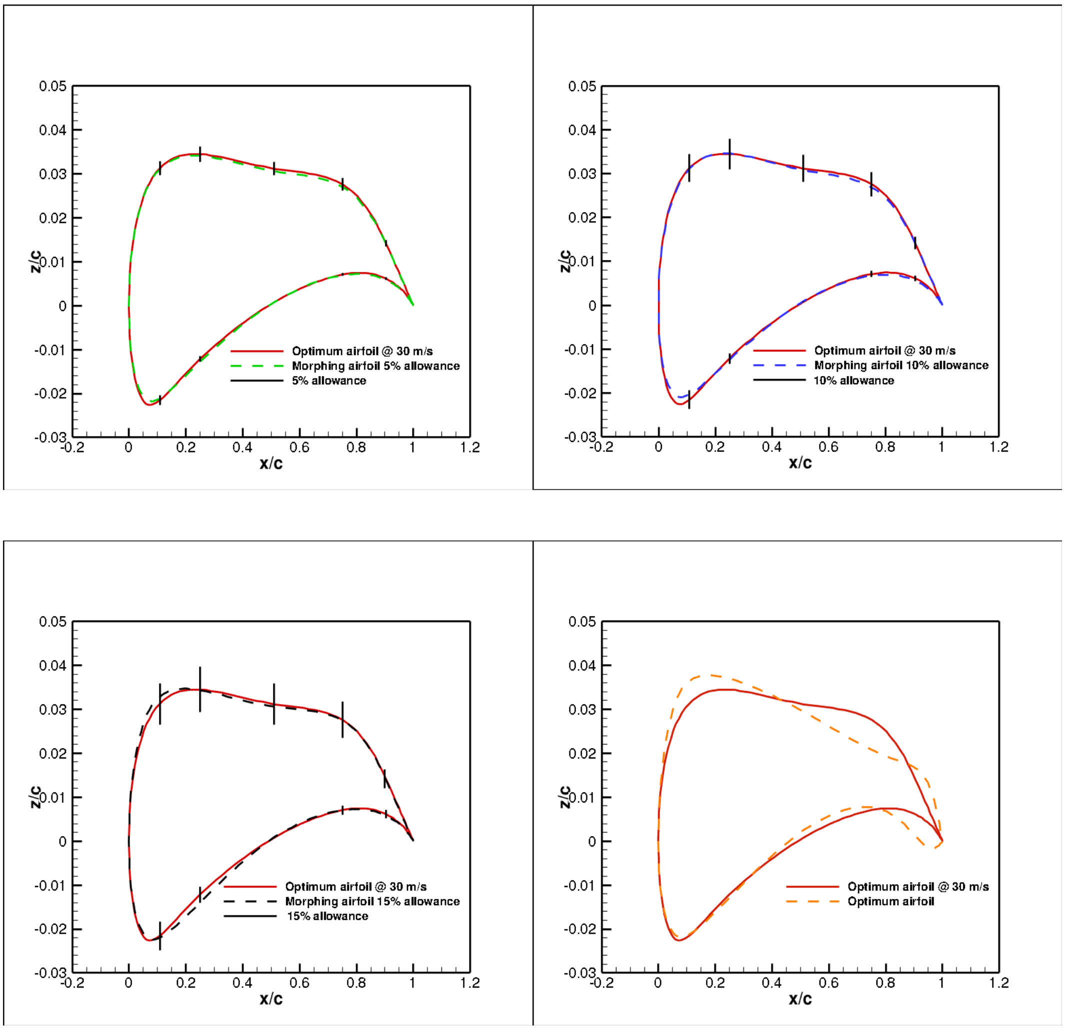

Figure 5.16 Morphing airfoil shapes at % 5 allowance (top left), % 10 allowance (top right), % 15 allowance (bottom left), without physical constraint (bottom right) at 40 m/s.

According to the results in Figure 5.16, upper region of the airfoil shape does not vary significantly for 5 %, 10 % and 15 % allowances apart form the region that is around 0.1c. When there is no physical limit, trailing edge region of the airfoil shape is different. The morphing airfoil shapes can be seen together in Figure 5.17.

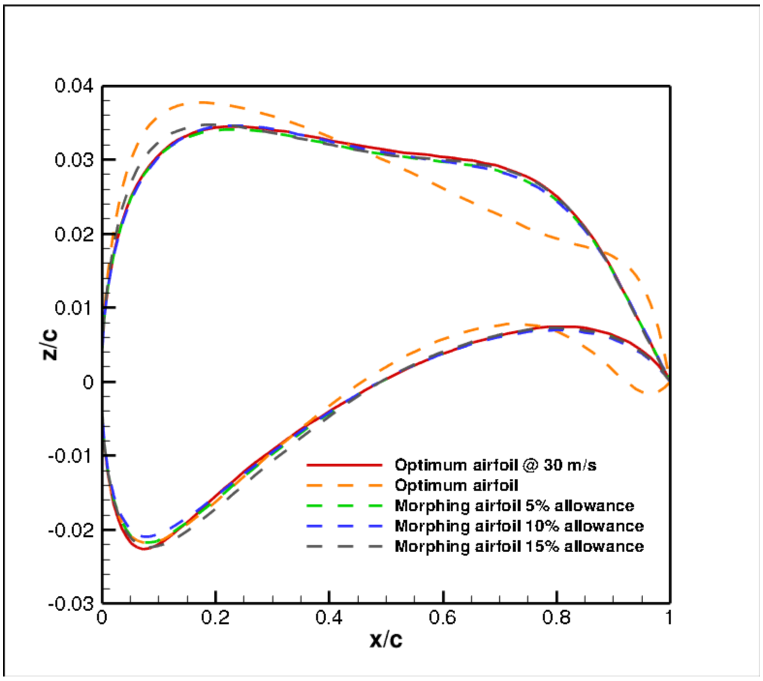

Figure 5.17 Morphing airfoil shapes at different allowances at 40 m/s.

Table 5.7 shows aerodynamic results for 40 m/s at steady level flight.

Table 5.7 Steady level flight data for morphing wing that is obtained with only airfoil shape change at 40 m/s.

Change Allowance (%)	Lift (N)	Corrected Lift (N)	Induced Drag + Pressure Drag (N)	Total Drag (N)	α (deg)
0	106.011	106.010	0.494	3.734	-0.563
5	106.011	106.010	0.504	2.333	-0.510
10	106.011	106.010	0.512	2.302	-0.501
15	106.011	106.010	0.483	2.268	-0.486
100	106.011	106.010	0.493	2.259	-0.533

Contrary to the results for 16 m/s and 20 m/s, more drag reduction is observed at 40 m/s. Even at 5% change allowance, drag result is very close to result of 100% allowance. At higher velocities, the main source of the drag is skin friction drag and it can be reduced by shape change allowance. This is the main reason for this reduction.

Figure 5.18 depicts the results for 50 m/s.

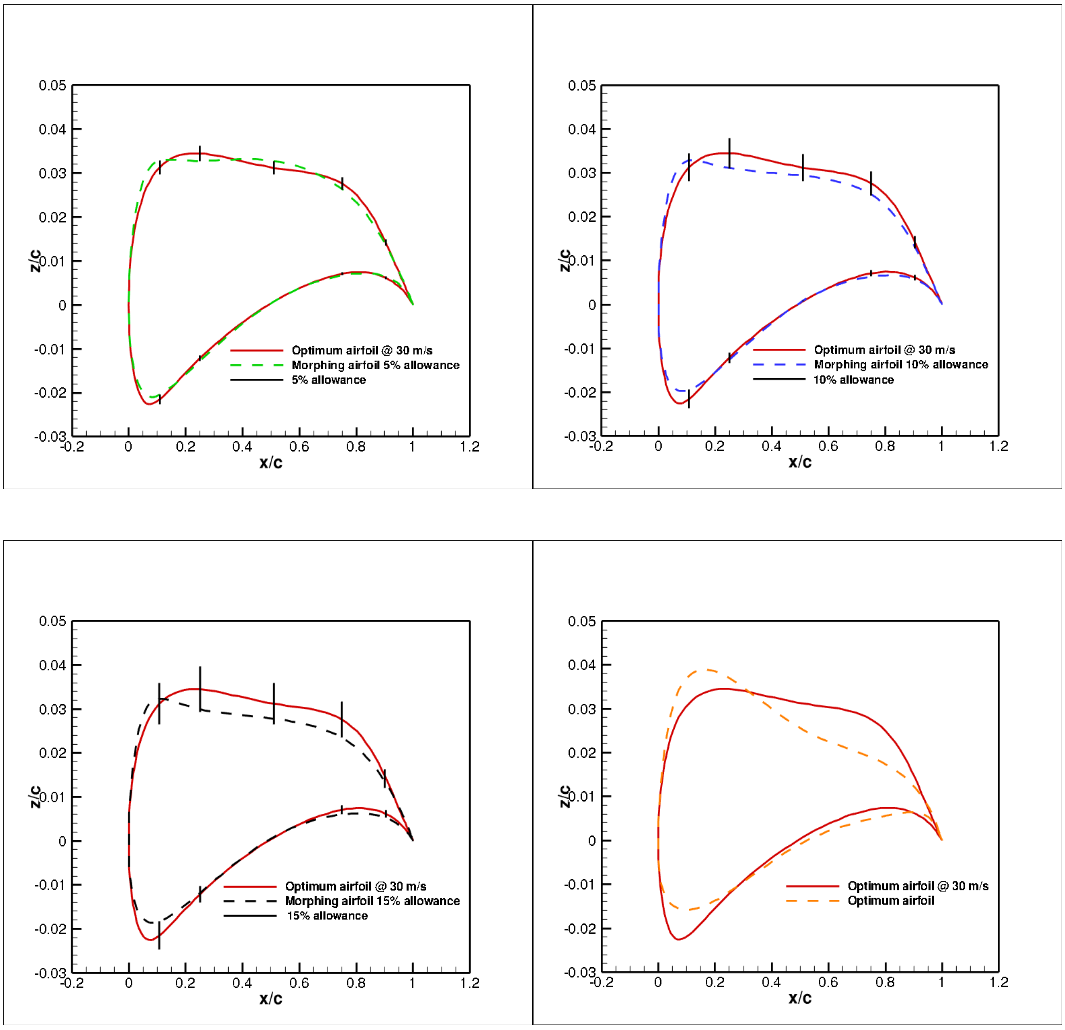

Figure 5.18 Morphing airfoil shapes at % 5 allowance (top left), % 10 allowance (top right), % 15 allowance (bottom left), without physical constraint (bottom right) at 50 m/s.

According to the results in Figure 5.18, as allowance increases physical thickness and curvature slope at lower surface that is around 0.05c-0.1c decreases. At this velocity, stagnation point moves towards the upper surface due to negative angle of attack and airfoil tends to decrease the slope of the leading edge at lower region of airfoil for the propagation of boundary layer development that will create less skin friction drag. When there is no physical limit, trailing edge region of the airfoil shape is different. For this situation, which is also valid for the other velocities, it should be stated that control points that are close to the trailing edge have less change allowance apart from 100 % allowance, because physical thickness at lower surface of the trailing edge is very short. As a result of this, these control points cannot vary effectively. This situation also influences the mathematical representation of airfoils. The morphing airfoil shapes can be seen together in Figure 5.19.

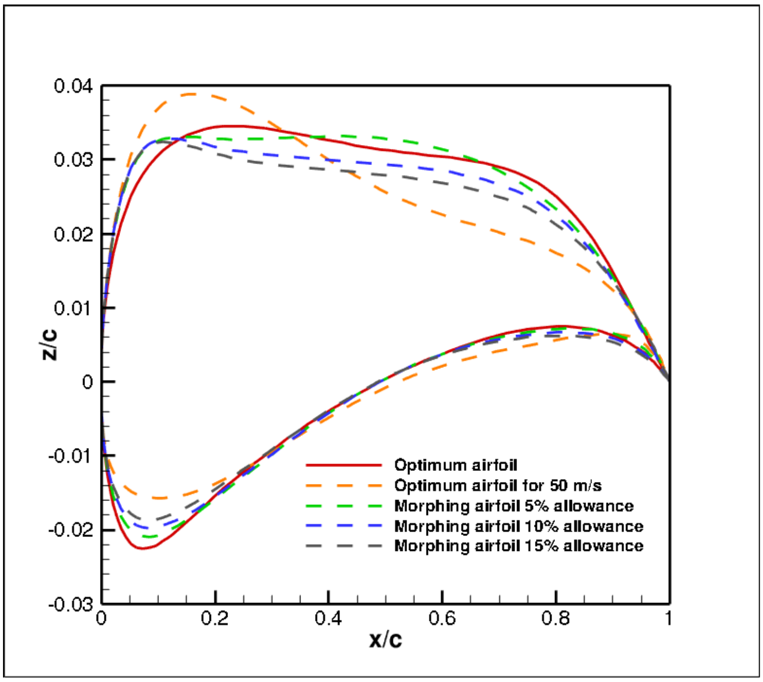

Figure 5.19 Morphing airfoil shapes at different allowances at 50 m/s.

Table 5.8 shows the aerodynamic results with allowance changes for 50 m/s.

Table 5.8 Steady level flight data for morphing wing that is obtained with only airfoil shape change at 50 m/s.

Change Allowance %	Lift (N)	Corrected Lift (N)	Induced Drag + Pressure Drag (N)	Total Drag (N)	α (deg)
0	106.011	106.010	0.399	5.394	-1.365
5	106.011	106.010	0.396	5.120	-1.467
10	106.011	106.010	0.404	3.569	-1.242
15	106.011	106.010	0.422	3.467	-1.220
100	106.013	106.010	0.473	3.372	-1.403

With a similar comment for 40 m/s, drag reduction is significant for 50 m/s when it is compared with 16 m/s and 20 m/s. However significant drag reduction is observed at 10% change allowance at 50 m/s when it is compared with 100% allowance.

According to the results that are discussed in this section, 10% allowance is quite efficient in terms of reduction in drag and required energy for morphing mechanism at velocities greater than 30 m/s. For 16 m/s most significant drag reduction is observed at 15% change allowance whereas significant drag reduction is not obtained at 20 m/s regardless of shape change allowance. As a result of this discussion, it is decided to use 10% change allowance for morphing wing optimization with airfoil shape and planform change considering the number of actuators and the required energy by them. Drag vs. velocity graph for baseline wing, optimum wing in Section 5.4.3 and morphing wing that is obtained with only airfoil shape change with %10 allowance is given Figure 5.20.

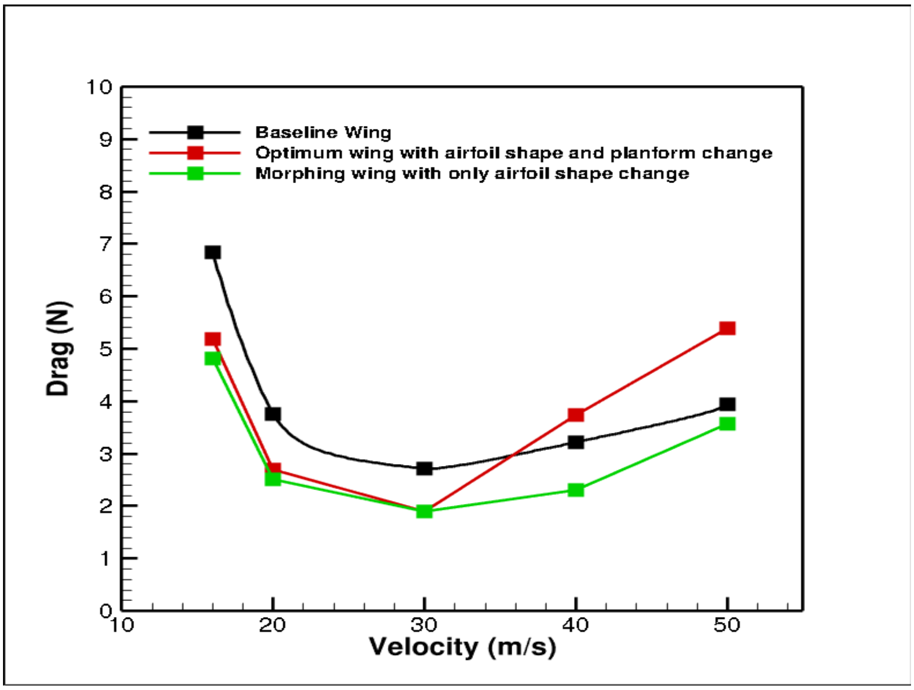

Figure 5.20 Drag vs. velocity for baseline wing, optimum wing that is obtained with airfoil shape and planform change and morphing wing that is obtained with only airfoil shape change with 10 % change allowance.

According to the results, morphing airfoil that is obtained in this optimization problem has less drag at each velocity that is analyzed when it is compared with the baseline wing and the optimum wing. But significant drag reduction is observed at velocities higher than 30 m/s.

5.5.2 Morphing Wing Optimization with Only Planform Change

In this part, optimization design variables are planform design variables and the problem is defined mathematically below.

$$\begin{aligned} &\text{Minimize } D = D_i + D_p + D_f \\ &@\, V_\infty = 16\,\mathrm{m/s}, 20\,\mathrm{m/s}, 40\,\mathrm{m/s} \text{ and } 50\ \mathrm{m/s} \end{aligned} \tag{5.37}$$

subject to

$$L = W = 106.01\ \mathrm{N} \tag{5.38}$$

$$-5^{o} \le \alpha \le 15^{o} \tag{5.39}$$

$$0.1\ \mathrm{m} \le c_r, c_t \le 0.2\ \mathrm{m} \tag{5.40}$$

$$1.2\ \mathrm{m} \le b/2 \le 2\ \mathrm{m} \tag{5.41}$$

According to the optimization problem, there exist 1 equality constraint. Starting wing is the optimum wing that is found in Section 5.4.3 for 30 m/s. Morphing planform change allowances for chords and span are 33% and 25%, respectively. These allowances are chosen so that it contains the planform area of the baseline wing. Figure 5.21 shows the optimum morphing wing planforms for different velocities.

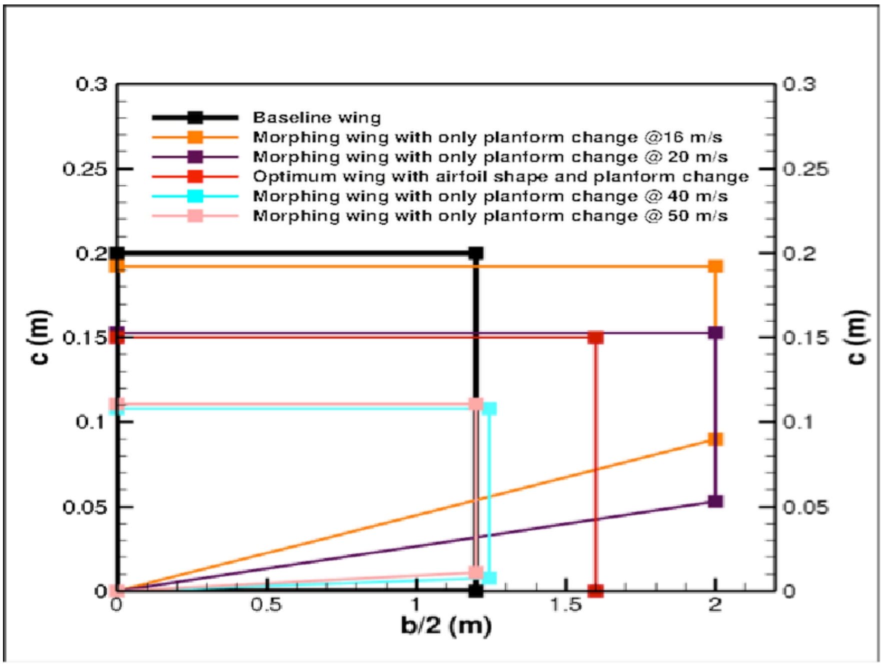

Figure 5.21 Baseline wing and optimum wing that is obtained with airfoil shape and planform change and morphing wings that are obtained with only planform change at different velocities, top view.

According to the results in Figure 5.21, as speed decreases planform area increases in order to provide the required lift. In addition to this, wing taper ratio decreases in order to decrease the induced drag. As speed increases, the main source of lift becomes velocity and the area decreases. Moreover, there is a small taper ratio at 40 m/s and 50 m/s velocities. In order to understand this, drag result of the smallest allowed planform in this optimization for 50 m/s is given with the results of the optimized planforms in Table 5.9.

Table 5.9 Steady level flight data for morphing wing that is obtained with only planform change.

	16 (m/s)	20 (m/s)	30 (m/s)	40 (m/s)	50 (m/s)	50 (m/s) the smallest wing
α (deg)	10.928	5.316	1.169	1.3	-0.109	0.028
c_r (m)	0.192	0.153	0.15	0.108	0.111	0.1
b/2 (m)	2	2	1.6	1.241	1.2	1.2
c_t (m)	0.102	0.1	0.15	0.1	0.1	0.1
Induced Drag + Pressure Drag (N)	1.660	0.757	0.705	0.648	0.516	0.520
Total Drag (N)	3.266	2.02	1.897	1.827	2.259	2.280
S (m^2)	0.588	0.506	0.48	0.258	0.253	0.24
AR	27.194	31.642	21.334	23.905	22.786	24
λ	0.530	0.654	1	0.929	0.904	1

As it is seen Table 5.9, the smallest allowed wing has 2.280 N drag at 0.028 degree angle of attack value at 50 m/s, whereas optimum wing has 2.259 N drag at -0.109 degree angle of attack value at the same velocity. The morphing wing in this section for 50 m/s increases its area in order to maintain steady level flight at less drag by increasing the root chord. This situation also decreases the taper ratio and summation of induced drag and pressure drag alters although there is an increment in wing area, which is directly proportional to pressure drag. Drag vs. velocity graph for this morphing system is shown in Figure 5.22.

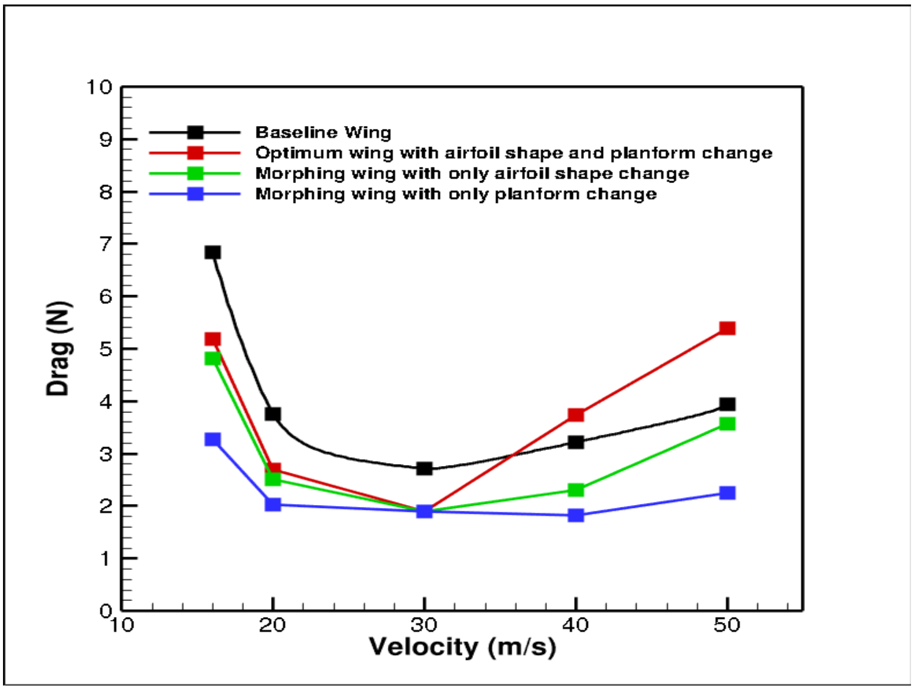

Figure 5.22 Drag vs. velocity for baseline wing, optimum wing that is obtained with airfoil shape and planform change and morphing wings that are obtained with only airfoil shape change and only planform change.

According to the results in Figure 5.22, morphing wing optimization that is obtained with only planform change has a very significant role in drag reduction above and below 30 m/s and its contribution to drag reduction can be seen better if velocity is further away from that velocity. Moreover, it has more drag reduction than the morphing wing that is obtained with only airfoil change, as it is expected from the drag formula. Because, when planform is morphed not only drag coefficient is minimized but also area can be optimized for minimum drag. But, when airfoil is morphed, only drag coefficient is minimized.

5.5.3 Morphing Wing Optimization with Airfoil Shape and Planform Change

The optimization problem in this part is basically a simultaneous application of the optimization problems in sections 5.5.1 and 5.5.2. As it is mentioned above, 10%

change allowance for airfoil shape is used in this part. The starting wing in this part of morphing wing optimization is the wing that is obtained by fixed wing optimization with airfoil shape and planform change in Section 5.4.3.

$$\begin{gathered}\text{Minimize } \mathrm{D} = \mathrm{D_i} + \mathrm{D_p} + \mathrm{D_f} \\ @\ \mathrm{V_\infty} = 16\ \mathrm{m/s}, 20\ \mathrm{m/s}, 40\ \mathrm{m/s} \text{ and } 50\ \mathrm{m/s}\end{gathered} \tag{5.42}$$

subject to

$$\mathrm{L} = \mathrm{W} = 106.01\ \mathrm{N} \tag{5.43}$$

$$-5^{\mathrm{o}} \leq \alpha \leq 15^{\mathrm{o}} \tag{5.44}$$

$$\mathrm{z_1/c} \geq 0.001 \tag{5.45}$$

$$\mathrm{z_6/c} \geq 0.01 \tag{5.46}$$

$$\mathrm{z_i/c} \geq 0\ \mathrm{i} = 2-5, 7-11 \tag{5.47}$$

$$\mathrm{z_i/c} \leq 0.1\ \mathrm{i} = 1-11 \tag{5.48}$$

$$\begin{gathered}0.9 * \left(\frac{\mathrm{z}}{\mathrm{c}}\right)_{\mathrm{upinitial}_{\frac{x}{c}}} \leq \left|\left(\frac{\mathrm{z}}{\mathrm{c}}\right)_{\mathrm{up}_{\frac{x}{c}=i}}\right| \leq 1.1 * \left(\frac{\mathrm{z}}{\mathrm{c}}\right)_{\mathrm{upinitial}_{\frac{x}{c}}} \\ \text{for } \frac{\mathrm{x}}{\mathrm{c}} = 0.9, 0.75, 0.5, 0.25 \text{ and } 0.1\end{gathered} \tag{5.49}$$

$$\begin{gathered}1.1 * \left(\frac{\mathrm{z}}{\mathrm{c}}\right)_{\mathrm{lowinitial}_{\frac{x}{c}}} \leq \left|\left(\frac{\mathrm{z}}{\mathrm{c}}\right)_{\mathrm{low}_{\frac{x}{c}=i}}\right| \leq 0.9 * \left(\frac{\mathrm{z}}{\mathrm{c}}\right)_{\mathrm{lowinitial}_{\frac{x}{c}}} \\ \text{for } \frac{\mathrm{x}}{\mathrm{c}} = 0.9, 0.75, 0.5, 0.25 \text{ and } 0.1\end{gathered} \tag{5.50}$$

$$0.1\ \mathrm{m} \leq \mathrm{c_r}, \mathrm{c_t} \leq 0.2\ \mathrm{m} \tag{5.51}$$

$$1.2\ \mathrm{m} \leq \mathrm{b}/2 \leq 2\ \mathrm{m} \tag{5.52}$$

Figure 5.23 shows the optimum morphing wing planforms and Table 5.10 shows optimum planform and drag results for different velocities.

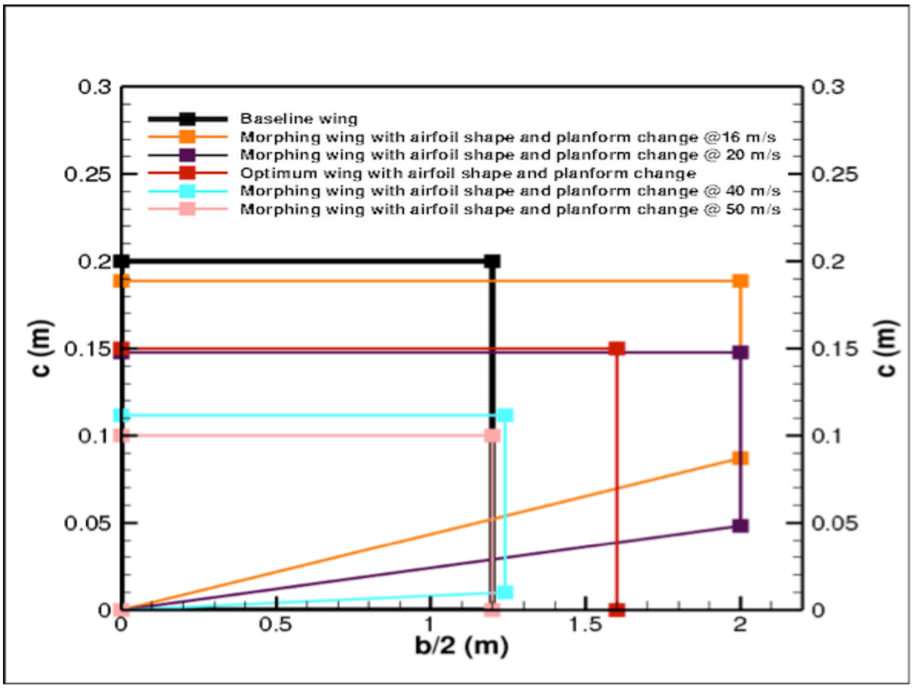

Figure 5.23 Baseline wing, optimum wing that is obtained with airfoil shape and planform change and morphing wings that are obtained with airfoil shape and planform change, top view.

Table 5.10 Steady level flight data for morphing wing that is obtained with airfoil shape and planform change.

	16 (m/s)	20 (m/s)	30 (m/s)	40 (m/s)	50 (m/s)
α (deg)	10.812	5.416	1.169	0.975	-0.281
c_r (m)	0.189	0.148	0.150	0.112	0.100
b/2 (m)	2.000	2.000	1.600	1.200	1.200
c_t (m)	0.102	0.100	0.150	0.102	0.100
Induced Drag+ Pressure Drag (N)	1.676	0.749	0.705	0.713	0.558
Total Drag (N)	3.146	1.928	1.897	1.759	1.961
S (m^2)	0.582	0.495	0.480	0.257	0.240
AR	27.502	32.313	21.334	22.443	24.000
λ	0.539	0.678	1.000	0.909	1.000

When results are compared with the results in Figure 5.21 and Table 5.9, it is seen that planform design variables are very close to each other. The morphing wing areas decrease for all velocities for combined planform and airfoil morphing. Total drag decreases for all velocities but these decrements may be regarded as small considering the effort that will be put into the design and the complexity of the system that will morph both the airfoil and the planform. The obtained morphing airfoils are depicted in Figure 5.24.

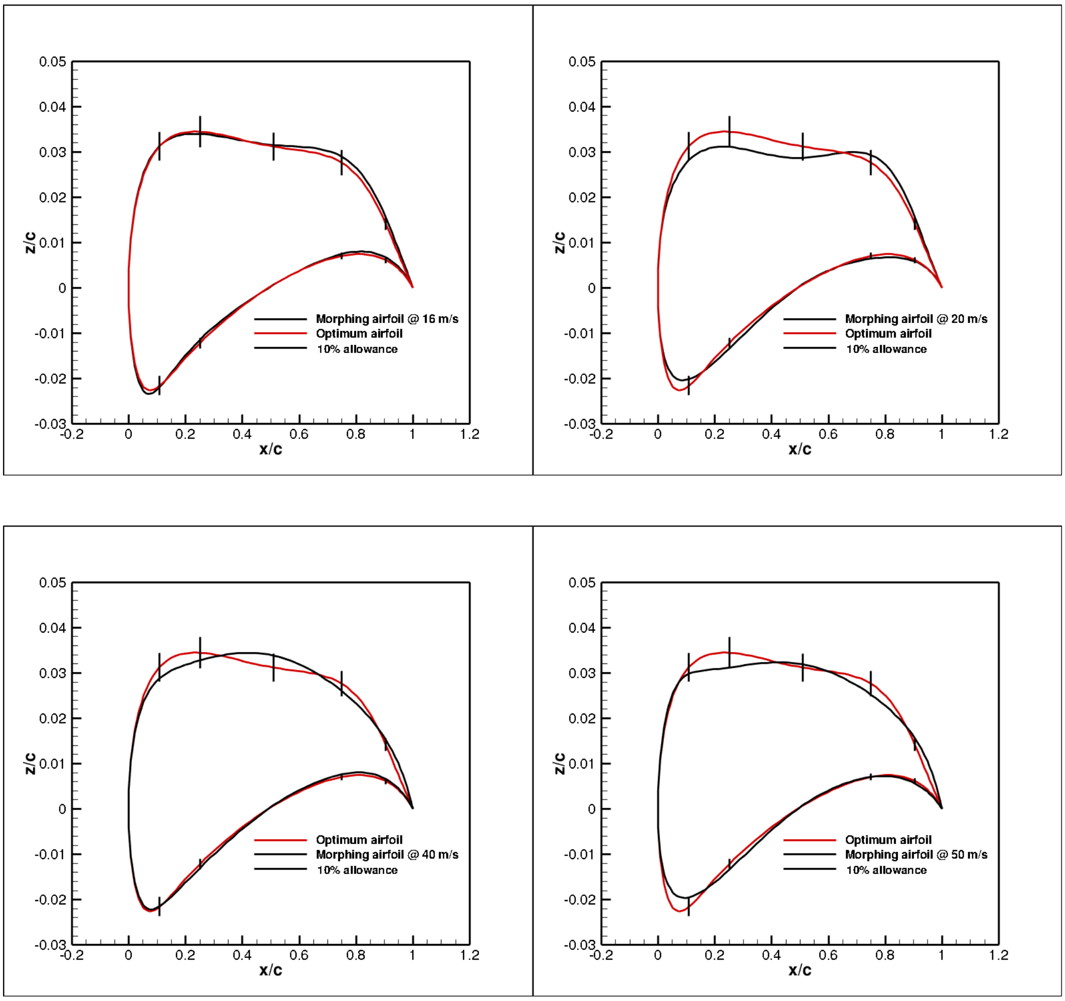

Figure 5.24 Morphing airfoil that is obtained with airfoil shape and planform change at 16 m/s (top left), at 20 m/s (top right), 40 m/s (bottom left), 50 m/s (bottom right).

According to the results, for velocities greater than 30 m/s, airfoils have greater trailing edge angles compared to the optimum airfoil for 30 m/s whereas no significant variation is observed for velocities less than 30 m/s. Apart from the morphing airfoil for 16 m/s, physical thickness at the leading edge of the upper surface decreases, i.e. camber is reduced. Moreover, if the results for 16 m/s are investigated in detail it is seen that the upper surface of the airfoil does not reach the allowed upper and lower bounds. The turbulent separation that exists around 0.05c is the main reason for this. After separation, shape change allowance limits and location of the control points cannot delay separation.

Figure 5.25 shows the comparison of drag results.

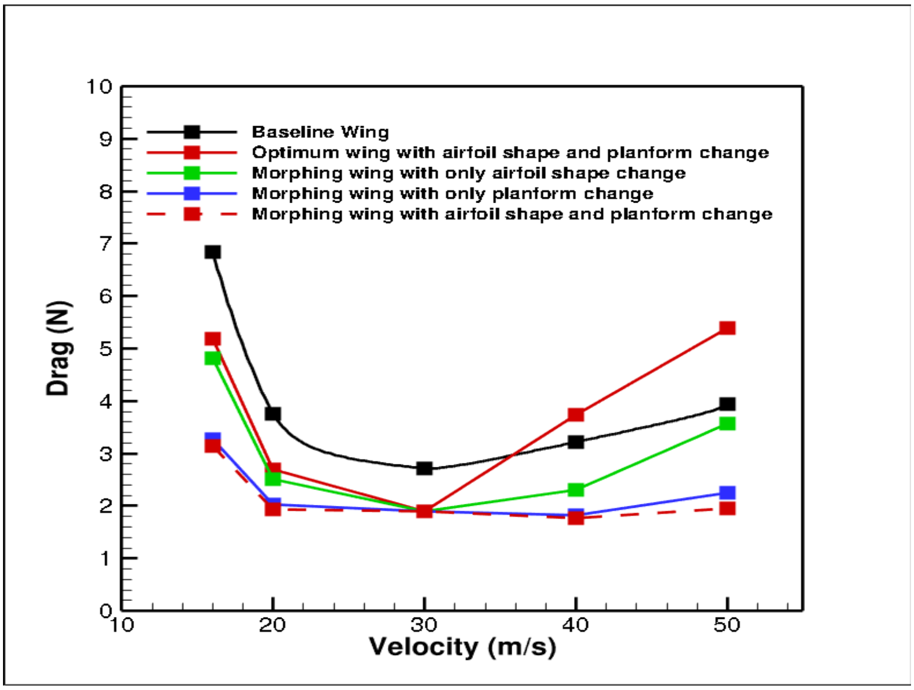

Figure 5.25 Drag vs. velocity for baseline wing, optimum wing that is obtained with airfoil shape and planform change and morphing wings that are obtained with only airfoil shape change, only planform change and airfoil shape and planform change.

Figure 5.25 shows that drag results of the morphing wing that is obtained with combined airfoil shape and planform change are very close to the morphing wing that is obtained with only planform change. This is a somehow expected result because the skin friction drag is mostly dependent on the wetted are of the wing. When morphing wing optimization in this section and the morphing wing optimization in Section 5.5.2 are compared, it is seen that the wetted areas are very similar. The skin friction drag is also dependent on the camber and angle of attack although less than the wetted area.

In summary, planform morphing alone provides the major aerodynamic performance improvement and airfoil morphing yields a marginal improvement over that.

Therefore, when the above considerations are kept in mind, if the morphing technologies are put into practice, the priority may be given to planform morphing.

5.6 Conclusion

In this chapter, fixed wing and morphing wing optimization problems are solved by using aerodynamic and optimization solvers that are described in Chapter 2, Chapter 3 and Chapter 4. Fixed wing optimization is performed for only airfoil change, only planform change and both planform and airfoil change. According to the results, the least drag is obtained when planform and airfoil design variables are defined as design variables for the optimization problem. After that, it is assumed that morphing mechanisms are installed to the optimum wing and effects of airfoil and planform design variables on drag reduction are investigated in the same manner as in fixed wing optimization. According to the results, morphing wing that is obtained with only planform change is the most effective morphing mechanism when complexity of the system, additional weight of the servos or actuators and energy required by them are kept in mind. The results for only airfoil morphing even without any limits for shape change show that the drag reduction is not as significant as the drag reduction when the morphing is performed with only planform change. This is due to the fact that planform change does not only minimize drag but also optimizes wing area for minimum drag.

Airfoil morphing should not be regarded as totally useless, though. Airfoil morphing may be used for maneuvering the airplane, where small deflections produce sufficient moments, like in an aileron for example. Of course, for such applications, the response times of the morphing mechanism to a given command should be very short.

Another aspect that can be relevant to airfoil morphing is when differential morphing is used in order to optimize the lift distribution of a wing, which will further reduce the induced drag. In this case, the response of the mechanism need not be as fast as for control surface applications.

Finally, morphing wing optimization should be performed for other missions of the flight envelope in order to prove the effectiveness of planform change in morphing wing applications.

CHAPTER 6

CONCLUSION

Morphing wing optimization is performed for an UAV for steady level flight in order to minimize drag. In order to perform optimization, function evaluators that are 3-D panel method and 2-D boundary layer solver are developed in order to obtain the lift and the drag values. These solvers are compared with the software that are widely used in the literature and results are in agreement. An optimization solver is developed by using a generalized reduced gradient method and a benchmark structural optimization problem in the literature is solved for validation and the results, which are compatible with the results of the other solvers in literature, are obtained.

After development and comparison process of aerodynamic and optimization solvers, a fixed wing optimization analysis is performed in order to find the optimum wing for 30 m/s, at which the baseline wing has the minimum drag. For this, three different optimization problems are solved according to the design variables of the planform and the airfoil shape.

Then, the optimum fixed wing is defined as the wing that will be morphed during steady level flight at different velocities. The morphing wing optimization process is similar to the fixed wing optimization process. At first, the planform is unaltered and the airfoil shape is changed according to the shape change allowance ratios. It is found out that 10% shape change allowance is adequate in order to obtain a noticeable drag reduction when morphing mechanism’s weight and energy demand is taken into account. After that, morphing wing optimization problem is solved only by using planform design variables. The drag reduction results are much more significant when compared to the results obtained with only airfoil shape change and it is seen that the drag reduction difference increases as the velocity is further away from 30 m/s.

In the final part, a new optimization problem is defined by combining the previous morphing wing optimization problems and no significant drag reduction is observed when the results are compared with the morphing wing that is obtained with only planform change. According to the results that are obtained by the morphing wing optimization problems in this thesis, planform shape change is the most effective way of drag reduction in morphing wings. But further analyses are required in order to claim the final result in this thesis. For example, optimization of the thickness and camber control points along chord for minimum drag is just an example that first comes to mind. Moreover, the morphing wing should be optimized in the same way in this thesis according to the other missions of the flight envelope.

Further research is also in progress for implementation of a two way boundary layer solver as a more accurate flow solver. Moreover, there are some ideas about having a better back to feasible method and a more appropriate starting value method for optimization solvers. For a faster solver, computations must be performed in parallel.

In this thesis, the servo forces that must be present in order to produce the desired shape change are not studied, likewise the impact of morphing mechanisms on the overall weight is not considered. This may be a significant factor reducing or even negating the benefits of morphing. This is definitely an obvious and interesting endeavor for further studies.

On another path, feasibility of morphing to replace control surfaces is also an interesting endeavor. There, the response times should be very short, which is an important challenge to be faced by the designer. Small but very rapid shape changes should be incurred with small and lightweight mechanisms especially for systems that will replace the ailerons and the elevator.

On yet another effort, morphing can be used in order to optimize the lift distribution on a wing, which will further reduce the induced drag. Such morphing will not require short reaction times but differential morphing is a challenge to overcome.

Theoretical and experimental studies related with morphing wing concept should get more attention from scientists for a greener World.

REFERENCES

[1] Weisshaar T. A., “Morphing Aircraft Technology – New Shapes for Aircraft Design”, TO-MP-AVT-141, 2006.

[2] Wright Brothers Aeroplane Company, http://www.wright-brothers.org/Information_Desk/Help_with_Homework/Help_with_Homework_Intro/What%20did%20the%20Wright%20brothers%20invent.pdf, accessed on 31.07.2014.

[3] Technology, Engineering, and Mathematics (STEM) Workforce Needs in the Future & Strategy to Meet Them Committee on Examination of the U.S. Air Force's Science, National Research Council, “Examination of the U.S. Air Force's Science, Technology, Engineering, and Mathematics (STEM) Workforce Needs in the Future and Its Strategy to Meet Those Needs”, National Academies Press, 2010.

[4] Sanders B, Eastep F. E., Forster E., “Aerodynamic and Aeroelastic Characteristics of Wings with Conformal Control Surfaces for Morphing Aircraft”, Journal of Aircraft, Vol. 40, No. 1, pp. 94-99, 2003.

[5] ww2aircraft.net, http://www.ww2aircraft.net/forum/other-mechanical-systems-tech/makhonine-telescoping-wing-8527.html, accessed on 24.07.2014.

[6] Boeing, http://boeing.mediaroom.com/2010-12-02-Boeing-Marks-Retirement-of-Royal-Australian-Air-Force-F-111-Fleet, accessed on 12.06.2014.

[7] Watershed Publishing, http://www.defenseindustrydaily.com/the-2006-saudi-shopping-spree-bae-wins-tornado-fleet-upgrade-contract-02605/, accessed on 03.08.2014.

[8] Matthew Ashworth, http://people.bath.ac.uk/ma346/Morphing%20Structures%20in%20Aircrafts.html, accessed on 18.08.2014.

[9] Wlezien R. W., Horner G. C., McGowan A.R., Padula S. L., Scott M. A., Silcox R. J., Simpson J.O., "The Aircraft Morphing Program", SPIE Proceedings, Vol. 3326, pp. 176-187, 1998.

[10] Texas A&M University, http://dnc.tamu.edu/projects/flowcontrol/Morphing/public_html/darpa.html, accessed on 15.07.2014.

[11] Defense Update, http://defense-update.com/products/t/tomahawk.htm accessed on 21.08.2014.

[12] Blondeau, J., Richeson, J. and Pines, D.J. 2003. ''Design, Development and Testing of a Morphing Aspect Ratio Wing Using an Inflatable Telescopic Spar'' 44th AIAA/ASME/ASCE/AHS/ASC Structures, Structural Dynamics and Materials Conference, Virginia, USA, 2003.

[13] Yin W., Sun Q., Zhang B., Liu J. and Leng J. "Seamless morphing wing with SMP skin", Advanced Materials Research, Vol. 47-50, pp. 97-100, 2003.

[14] Neal D.A., Good M.G., Johnston C.O., Robertshaw H.H., Mason W.H. and Inman, D.J., ''Desing and Wind-Tunnel Analysis of a Fully Adaptive Aircraft Configuration'', 45th AIAA/ASME/ASCE/AHS/ASC Structures, Structural Dynamics, and Materials Conference, California, 2004.

[15] Boria F., Stanford B., Bowman S. and Ifju P., ''Evolutionary Optimization of a Morphing Wing with Wind-Tunnel Hardware in the Loop'', AIAA Journal, Vol. 47, pp. 399-409, 2009.

[16] Bilgen O., Friswell M.I., Kochersberger K.B. and Inman D.J., ''Surface Actuated Variable-Camber and Variable-Twist Morphing Wings Using Piezocomposites'', 52nd AIAA/ASME/ASCE/AHS/ASC Structures, Structural Dynamics, and Materials Conference, Denver, USA, 2011.

[17] Gonzalez L., “Morphing wing using shape memory alloy: a concept proposal”, Final research paper in 2005 Summer Research Experience for Undergraduates (REU) on Nanotechnology and Materials Systems, Texas, USA, 2005.

[18] Vos R., Gurdal Z, and Abdalla M., ‘‘Mechanism for Warp-Controlled Twist of a Morphing Wing,’’ Journal of Aircraft, Vol. 47, pp. 450-457, 2010.

[19] Gamboa P., Vale J., Lau F. J. P. and Suleman A, ‘‘Optimization of a Morphing Wing Based on Coupled Aerodynamic and Structural Constraints’’, AIAA Journal, Vol. 47, pp. 2087-2104, 2009.

[20] Willis D. J., “An Unsteady, Accelerated, High Order Panel Method with Vortex Particle Wakes”, Ph.D. Thesis, Massachusetts Institute of Technology, 2006.

[21] Katz J., Plotkin A., “Low-speed Aerodynamics: from Wing Theory to Panel Methods”, McGraw-Hill, New York, USA, 1991.

[22] Texas A&M University, http://www.xflr5.com/xflr5.htm, accessed on 13.08.2014.

[23] Deperrois A., "Results vs. prediction", Presentation document, July 2008.

[24] Morino L. and Suciu E. O., “Nonlinear Steady Incompressible Lifting Surface Analysis with Wake Roll-Up”, AIAA Journal, Vol. 15, No. 1, pp. 54-58, 1977.

[25] E. O. Suciu, “A Finite Element Analysis of The Exact Nonlinear Formulation of A Lifting Surface in Steady Incompressible Flow, with The Evaluation of The Correct Wake Geometry”, M. S. Thesis, Boston University, 1975.

[26] Suciu E.O. and Morino L., “A Nonlinear Finite Element Analysis of Wings in Steady Incompressible Flows with Wake Rollup”, AIAA Paper, pp. 76-64, 1976.

[27] Gaggero S. and Brizzolara S., "Exact Modeling of Trailing Vorticity in Panel Method for Marine Propeller," 2nd International Conference on Marine Research and Transportation, pp. 9 -19, Naples, Italy, 2007.

[28] Hsin C. Y., "Development and Analysis of Panel Methods for Propellers in Unsteady Flow", Ph. D. Thesis, Massachusetts Institute of Technology, 1987.

[29] Pyo S., "Numerical Modeling of Propeller Tip Flows with Wake Sheet Roll-up in Three Dimensions", Massachusetts Institute of Technology, Report No. 95-6, 1995.

[30] John Burkardt, http://people.sc.fsu.edu/~jburkardt/f77_src/toms423/toms423.f, accessed on 18.09.2013.

[31] Eppler R. and Somers D. M., "Supplement To: A Computer Program for the Design and Analysis of Low-Speed Airfoils", NASA TM-81862, 1980.

[32] Wauquiez C., "Shape Optimization of Low Speed Airfoils Using MATLAB and Automatic Differentiation", Lic. Thesis, Royal Inst. Of Technology, 2000.

[33] Drela M., and Giles M. B., "Viscous-Inviscid Analysis of Transonic and Low Reynolds Number Airfoils", AIAA Journal, Vol. 25, No. 10, pp. 1347 – 1355, 1987.

[34] Wang X. and Shan X., "Shape Optimization of Stratosphere Airship". Journal of Aircraft, Vol. 43, No. 1, pp. 283-287, 2006.

[35] Moran J., "An Introduction to Theoretical and Computational Aerodynamics", John Wiley & Sons Inc., New York, 1984.

[36] JavaFoil - Dr. Martin Hepperle, http://www.mh-aerotools.de/airfoils/java/JavaFoil%20Users%20Guide.pdf, accessed on 29.08.2014.

[37] Mark Drela, http://web.mit.edu/drela/Public/web/xfoil/, accessed on 12.03.2014.

[38] Vanderplaats G. N., “Multidiscipline Design Optimization”, Vanderplaats Research and Development Inc., 2007.

[39] Microsoft, http://support.microsoft.com/kb/82890, accessed on 01.09.2014.

[40] Gill P. E., Murray W. and Saunders M. A., “SNOPT: An SQP Algorithm for Large-Scale Constrained Optimization”, SIAM Rev., Vol. 47, No.1, pp. 99–132, 2005.

[41] Rao S. S., “Engineering Optimization: Theory and Practice”, John Wiley & Sons, Inc., 2009.

[42] Ravindran A., Ragsdell K. M. and Reklaitis G. V., “Engineering Optimization: Methods and Applications”, John Wiley & Sons, Inc., 2006.

[43] ACCP, http://accp1.org/pharmacometrics/theory.htm, accessed on 18.04.2014.

[44] J.W. Chinneck, “The Constraint Consensus Method for Finding Approximately Feasible Points in Nonlinear Programs”, INFORMS Journal on Computing, Vol. 16, No. 3, pp. 255-265, 2004.

[45] Ibrahim W. and Chinneck J. W., “Improving Solver Success in Reaching Feasibility for Sets of Nonlinear Constraints”, Computers and Operations Research, Vol. 35, pp. 1394-1411, 2008.

[46] EXELIS, http://www.exelisvis.com/docs/CONSTRAINED_MIN.html, accessed on 30.08.2014.

VITA

PERSONAL INFORMATION

Surname, Name	: Körpe, Durmuş Sinan
Nationality	: Turkish (T.C.)
Date and Place of Birth	: January 1982, Ankara
Phone	: +90 (543) 4652406
E-mail	: dskorpe@ae.metu.edu.tr, dskorpe@gmail.com

EDUCATION

Degree	**Institution**	**Year of Graduation**
M.S	METU Aerospace Engineering	2008
B.S	METU Aerospace Engineering	2006
High School	İncirli Lisesi	2000

ACADEMIC EXPERIENCE

Year	**Place**	**Enrollment**
2012-Present	UTAA Astronautical Engineering Dept.	Lecturer
2010-2012	TÜBİTAK 1001 Project	Res. Assist.
2008-2012	METU Aerospace op Engineering	Grad. Res. Assist.
2006-2008	TÜBİTAK 1001 Project	Res. Assist.

RESEARCH INTERESTS

Low Speed Aerodynamics, Boundary Layer, Optimization, Aircraft Design

FOREIGN LANGUAGE

Advanced English, Basic German

JOURNAL ARTICLES

1. Sinan KÖRPE, Barış ERDOĞAN, Göknur BAYRAM, Serkan ÖZGEN, Yusuf ULUDAĞ and Niyazi BIÇAK, Crosslinked DADMAC Polymers as Cationic Super Absorbents, Reactive and Functional Polymers, Volume 69, Issue 9, Pages 660-665, September 2009.

INTERNATIONAL CONFERENCE PAPERS

1. Durmuş Sinan KÖRPE and Serkan ÖZGEN, Optimization of A Morphing Wing for Range, AIAC VII. Ankara International Aerospace Conference, Ankara, Turkey, 11-13 September 2013.

NATIONAL CONFERENCE PAPERS

1. D. Sinan KÖRPE, Levent ÜNLÜSOY, Melin ŞAHİN, Serkan ÖZGEN ve Yavuz YAMAN, Büyük Oranda Şekil Değiştirebilen Kanatların Ön Tasarım Sürecinde Aerodinamik ve Yapısal Analizlerinin Eşlenmesi, IV. Ulusal Havacılık ve Uzay Konferansı. İstanbul, Türkiye, 12-14 Eylül 2012.

2. Levent ÜNLÜSOY, Durmuş Sinan KÖRPE, Melin ŞAHİN, Serkan ÖZGEN ve Yavuz YAMAN, Büyük Oranda Şekil Değiştirebilen Kanatların Aerodinamik ve Yapısal Tasarımı. 6. Savunma Teknolojileri Kongresi, Ankara, Türkiye, 20-22 Haziran 2012.

3. D. Sinan KÖRPE, Barış ERDOĞAN, Yusuf ULUDAĞ, Serkan ÖZGEN, Göknur BAYRAM ve Niyazi BIÇAK, Yerdeyken Buzlanma Giderici/Önleyici Olarak Kullanılan Sıvıların Uçak Kanatları Üzerindeki Akış Kararlılığına Etkileri,

Kayseri VII. Havacılık Sempozyumu, Erciyes Üniversitesi, Kayseri, Türkiye, 15-16 Mayıs 2008.

4. Barış ERDOĞAN, D. Sinan KÖRPE, Yusuf ULUDAĞ, Göknur BAYRAM, Serkan ÖZGEN ve Niyazi BıÇAK, Uçakların Yerdeyken Kar ve Buz ile Kaplanmalarını Engelleyen Çözeltilerin Geliştirilmesi ve Üretimi, Kayseri VII. Havacılık Sempozyumu, Erciyes Üniversitesi, Kayseri, Türkiye, 15-16 Mayıs 2008.

POSTER PRESENTATIONS

1. D. Sinan KÖRPE, Barış ERDOĞAN, Göknur BAYRAM, Serkan ÖZGEN, Yusuf ULUDAĞ and Niyazi BIÇAK, Crosslinked DADMAC Polymers as Cationic Super Absorbents, Polyelectrolytes 2008 International Conference, University of Coimbra, Coimbra, Portugal, 16-19 June 2008.
2. Barış ERDOĞAN, D. Sinan KÖRPE, Göknur BAYRAM, Serkan ÖZGEN, Yusuf ULUDAĞ and Niyazi BIÇAK, Highly Alternating Copolymers of DADMAC with N-Vinyl Pyrrolidone in Aqueous Solution, Polyelectrolytes 2008 International Conference, University of Coimbra, Coimbra, Portugal, 16-19 June 2008.